Exploring Photocatalytic and Electrocatalytic Reduction of CO_2 with Re(I) and Zn(II) Complexes and Attempts to Employ a Novel Carbene Ligand to this Endeavor

By

Patrick Berro

A thesis submitted in partial fulfillment of the requirements for the degree of Master of Science in Chemistry

Department of Chemistry and Biomolecular Science

Faculty of Science

University of Ottawa

uOttawa

L'Université canadienne
Canada's university

Acknowledgements

First and foremost, I want to acknowledge the person who made this possible, my supervisor Dr. Darrin Richeson. Thank you for instilling confidence in all of us, for creating one of the greatest environments I have ever been a part of and for giving me four of my most memorable years from the very moment you took me in as an Honour’s student. I have learned so much from you and found a passion in a field I never thought I would.

Next, I want to thank everyone else that’s been a part of my experience here(undergrad and graduate studies), whether from my own lab or the other labs that I got to know. I can’t name you all, since the list would never end. This list also extends to the people that have helped me in learning various techniques and operating numerous equipment, whether part of the NMR facility, X-ray Crystallography, the undergrad lab etc…..

Lastly, thank you to all my friends and family, whether you’re a part of the above or not!
Thank you for all the support!!

Abstract

With the blend of addressing issues of sustainable energy with the environmental worries regarding emission of greenhouse gases, there is a motivation to target the efficient chemical reduction of CO_2. Re(I) integrated photosensitizers and catalysts, synthesized from commercially available ligands, are introduced with the selective CO_2 reduction of formic acid, making for a unique class of Re(I) catalysts typically selective for CO as a reduction product. Furthermore, synthesized Zn(II) phosphino aminopyridine complexes are structurally and computationally characterized as well as observed to function as unprecedented electrocatalysts for the reduction of CO_2 to formic acid and CO. Lastly, with the importance and popularity of N-heterocyclic carbenes (NHCs) as a class of ligands in the field of organometallic catalysis, six-membered perimidine based carbenes are further explored. Synthesis of a chelating pyridyl-perimidine NHC in addition to potential transition metal catalysts are also attempted.

Table of Contents

List of Figures

List of Schemes

List of Tables

List of Abbreviations

Ar	Aromatic Group
BNAH	1-Benzyl-1,4-Dihydronicotinamide
Bn	Benzyl
CAT	Catalyst
CV	Cyclic Voltammetry
DCM	Dichloromethane
DFT	Density Functional Theory
DMSO	Dimethylsulfoxide
E^o	Potential
ED	Electron Donor
GC	Gas Chromatography
HOMO	Highest Occupied Molecular Orbital
Hz	Hertz
iPr	Isopropyl
LUMO	Lowest Unoccupied Molecular Orbital
MS-EI	Mass Spectrometry Electron Impact
MET	Multiple Electron Donor
M	Molar
mM	Millimolar
NMR	Nuclear Magnetic Resonance
Np	Neopentyl
Ph	Phenyl
ppm	Parts Per Million
PS	Photosensitizer
Pyr	Pyridine
SCE	Standard Calomel Electrode

SC-XRD	Single Crystal X-ray Diffraction
SOMO	Singly Occupied Molecular Orbital
TEOA	Triethanolamine
THF	Tetrahydrofuran
UV	Ultraviolet Light
X	Halogen

Chapter I

Introduction

Purpose:

Society is currently facing momentous challenges from the increasing emissions of greenhouse gases and depleting resources for C1 feedstocks. Due to these pressures, there is increasing drive to discover chemical transformations of carbon dioxide (CO_2). This ubiquitous and thermodynamically stable species requires catalysts to activate it for reactions and chemical reduction. Reduction of CO_2 into valuable compounds provides new opportunities for use of this common oxidation product. The world's main energy source is fossil fuels, which are rapidly consumed to supply increasing energy demands. The release of energy from the combustion of fossil fuels results in generation of CO_2, a greenhouse gas, as a by product. However, the area of CO_2 reductions presents a critical challenge due to the high thermodynamic stability value of this gas. This means that this effort requires a large energy contribution to convert CO_2 to other valuable products, and that contributes to a high cost of production. To address this challenge, there is a huge effort to develop innovative new catalytic systems that are able to increase the potential of transforming CO_2.[1]

Two popular approaches in which present research has attempted to tackle CO_2 reduction catalysis have come via photochemical or electrochemical means. The ability to harness an unlimited source of energy in light (photo) or potential one in electricity (electro) is what makes these two avenues foundations of interest.

Thermodynamics of CO_2 Reduction

As mentioned earlier, the reduction of CO_2 has its challenges with the thermodynamic requirements for this reaction. Summarized in **Table 1.1** is the reduction potentials of multiple CO_2 reduction reactions. However, it should be noted that these reactions require the assistance of a proton source. The direct one electron reduction to form the radical $CO_2^{\bullet-}$ is an unfavourable process due to its high energy demand as signified by its large reduction potential of -2.14 V vs SCE. There are other more favourable pathways that employ proton-assisted multiple-electron transfer (MET). These proton coupled electron transfer reactions necessitate much less energy than the one electron reduction reaction.[2]

Table 1.1 The CO_2 reduction potentials for various CO_2 reduction reactions.

Reaction	E°(V) vs SCE[a]
$CO_2 + 2H^+ + 2e^- \rightarrow HCO_2H$	- 0.85
$CO_2 + 2H^+ + 2e^- \rightarrow CO + H_2O$	- 0.77
$CO_2 + 4H^+ + 4e^- \rightarrow C + 2H_2O$	- 0.44
$CO_2 + 4H^+ + 4e^- \rightarrow HCHO + H_2O$	- 0.72
$CO_2 + 6H^+ + 6e^- \rightarrow CH_3OH + H_2O$	- 0.62
$CO_2 + 8H^+ + 8e^- \rightarrow CH_4 + 2H_2O$	- 0.48

[a] E°' potentials are reported at pH 7.

Though these proton coupled electron transfer reductions are thermodynamically more favourable, an anchor for the CO_2 is required to overcome the kinetic barriers. One aspect to tackle these limitations is the utilization of homogenous transition metal complexes assisted by various and novel supporting ligands as a means to activate this linear molecule. These catalysts afford the capability to promote the multiple-electron transfer reactivity of the reduction reaction. Several diverse transition metal complexes have been explored for CO_2 reduction applications, utilizing their two main components that include the metal and the organic-based ligands that coordinate to the metal center.

Mechanism of CO_2 reduction

The reaction of CO_2 with molecular complexes usually occurs either by insertion into a metal-hydride bond or by binding to a vacant coordination site at the metal center (**Scheme 1.1**). The insertion pathway is thought to be promoted by electrostatic attractions between the polarized O−C and M−H bonds, positioning the electrophilic carbon-atom in close proximity to the nucleophilic hydride moiety. In contrast, electron-rich metals possessing free binding sites favor CO_2 activation through monodentate C-coordination, leading to a metallo-carboxylate species with O-atoms sterically exposed and available for protonation. Though both insertion and coordination can proceed through different routes that vary in the mode of CO_2 interaction with the metal center, the former process typically affords HCO_2H as a product as in **A**, whereas the latter has a greater tendency to yield CO as seen in **B**.[3-5]

One of the most common side reactions in the pathways of CO_2 reduction is the generation of hydrogen (H_2). Hydrogen formation can and has been envisioned through two general pathways: homolytic and heterolytic. In both cases, catalytic H_2 production by molecular complexes is generally thought to proceed through metal-hydride intermediates. The formation of these M-H groups is through a combination of reduction and protonation of the metal center. For a homolytic mechanism, the metal hydrides are formed by a combination of metal reduction and protonation. Reductive elimination from reaction of two metal hydride complexes yields H_2. The heterolytic pathway proceeds from one metal center by addition of a second electron and protonation to release H_2.[6]

Scheme 1.1 Two possible pathways for the catalytic two electron reduction reactions of CO_2 for the production of formate (**A**) and CO (**B**)

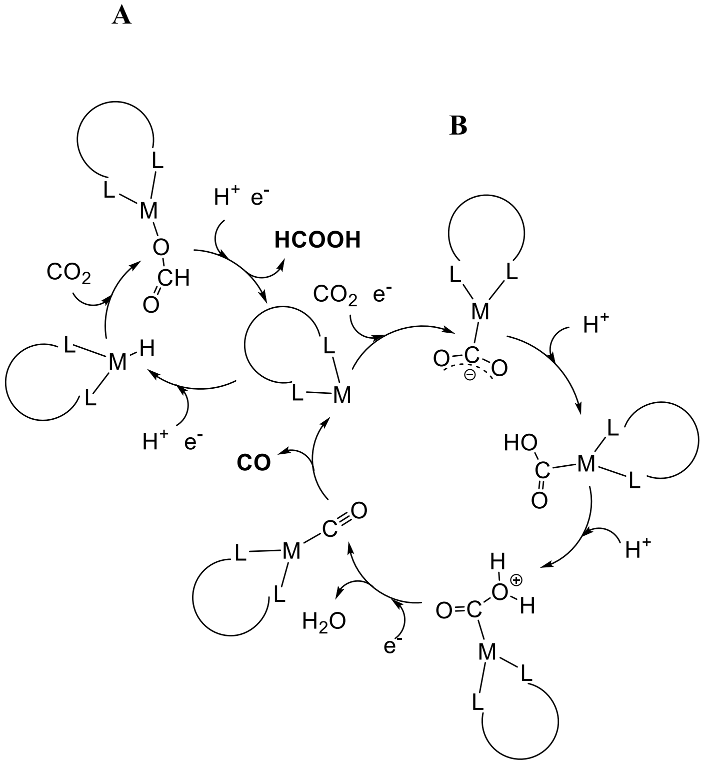

Overview

Typically, a molecular photocatalytic reduction reaction employs three main components; a photosensitizer (PS), an electron donor (ED) a catalyst (CAT). When irradiated with light, the PS is promoted to an excited electronic state (1). The excited state of the photosensitizer is reductively quenched by a sacrificial electron donor (ED), which is commonly an amine, to form the reduced photosensitizer (PS^-) and the oxidized sacrificial donor (ED^+) (2). This reduced photosensitizer (PS^-) will transfer the electron to the catalyst (CAT) to produce the reduced catalyst (CAT^-), which in turn will reduce a specific analyte.

$$PS + h\upsilon \rightarrow PS^* \qquad (1)$$

$$PS^* + ED \rightarrow PS^- + ED^+ \qquad (2)$$

$$PS- + CAT \rightarrow PS + CAT^- \qquad (3)$$

The quenching of the exited state can follow an oxidative or reductive pathway route as seen in **Figure 1.1**. This was first done by Tinneman et al. using transition metal complexes such as cobalt or nickel tetraaza-macrocylic compounds as the catalyst for CO_2 reduction in combination with $[Ru(bpy)_3]^{2+}$ photosensitizer. Decades later and although this photocatalytic system is still a mainstream setup, the field has expanded with newer catalysts and photosensitizers being introduced.

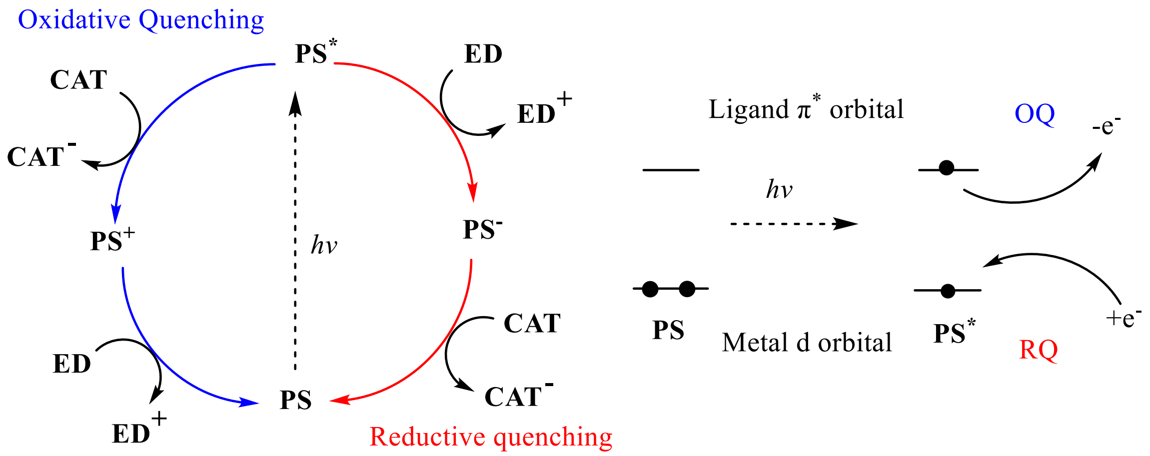

Figure 1.1 Oxidative (blue) and reductive (red) quenching pathways of an excited photosensitizer in the presence of an electron donor and catalyst

However, many of these photosensitizers generally lean towards being too expensive noble metals, which adds to the already metal centered catalyst in solution. Another system that can be introduced is an integrated photosensitizer/catalyst that bypasses the need of a supplementary molecule. In Chapter II, we present functionally integrated Re(I) photosensitizer/catalysts, using commercially available ligands, for the visible light photocatalytic reduction of CO_2. These complexes possess a structure that is unique among Re(I) photoreduction catalysts and unprecedented in the selective formation of formic acid.

As mentioned previously, another route for catalytic CO_2 reduction is the use of an electrochemical source of electrons. Electrochemistry provides an excellent and direct method to investigate and explore the reactions that involve electron transfers. Cyclic voltammetry (CV) is a powerful electrochemical technique usually used to probe the reduction and oxidation processes of the complexes in an electrocatalytic system. Electrocatalytic routes are particularly interesting as well as fundamentally appealing because one can envision using the limitless and sustainable supply of energy to power these transformations. Exploration of electrocatalytic reduction processes provides an ally to the previously discussed photocatalysis. Moreover, one advantage of electrochemical setups is the ‘cleaner’ system it offers as it nullifies the requirement of photosensitizer and electron donor additives in solution. Chapter III introduces successfully synthesized characterized divalent Zn(II) complexes examined for their ability to function in the electrocatalytic reduction of CO_2 with water as a proton source.

A major advantage of homogenous catalysis is the ability to tune the molecular structure of these transition metal complexes, providing a wide array of ligand exploration with the introduction of amines, phosphines and the more recent N-Heterocyclic carbenes (NHCs). As it pertains to NHCs, the synthesis of most of these catalysts have focused on the popular and more established five-membered ring frameworks. In 2003, our group first introduced a six-membered perimidine based carbene presenting a novel framework with an extended aromaticity. Chapter IV will further explore this ligand structure and attempts to synthesize potential first and second row transition metal catalysts will be established.

References:

1) J. Wu, Y. Huang, W. Ye, Y. Li, *Adv. Sci.*, 2017, **4**, 1700194.
2) A. J. Morris, G. J. Meyer, E. Fujita, *Acc. Chem. Res.*, 2009, **42**, 1983.
3) Z. Sun, T. Ma, H. Tao, Q. Fan, B. Han, *Chem*, 2017, **3**, 560.
4) C. Genovese, C. Ampelli, S. Perathoner, G. Centi, *Green Chem*., 2017, **19**, 2406.
5) S. Zhao, S. Li, T. Guo, S. Zhang, J. Wang, Y. Wu, Y. Chen, *Nano-Micro Lett.*, 2019, **11**, 62.
6) Z. Zhang, Y. Li, C. Hou, C. Zhao, Z. Ke, *Catal. Sci. Technol*., 2018, **8**, 656.
7) A. H. A. Tinnemans, T. P. M. Koster, D. Thewissen, A, Mackor, *Recl. Trav. Chim*. 1984, **103**, 288.
8) P. Bazinet, G. P. A. Yap, D. S. Richeson, *J. Am. Chem. Soc.* 2003, **125**, 13314.

Chapter II

Photocatalytic Pyridyl-Re(I) Complexes for CO_2 Reduction

Introduction:

Photocatalysis is a principally interesting approach to overcome the reaction barriers to reduce CO_2, by employing a clean and infinite resource, light, for conversion of this industrial by-product into more beneficial compounds. One product of interest is the two-electron reduction product, formic acid. This is particularly useful due to formic acid's potential as an H_2 (alternate form of fuel) carrier as well as its commercial use as a chemical.[1,2] In this broad field of harnessing energy from light, the search for such catalysts is crucial, with one particular subfield being that of molecular catalysts due to their more feasible ligand tuning and characterization.[3-5]

Generally, a photocatalytic system has three fundamental components: a photosensitizer (PS), for collecting the photon energy; an electron donor (ED), that which is the source of electrons for the reduction; and a catalyst (CAT) capable of binding and activating the CO_2. This typically follows two main pathways. In the case of an integrated catalyst/photosensitizer, electrons for the catalytic cycle can come directly from the ED through electron transfer to a photoexcited CAT, otherwise a photosensitizer is added to the reaction, the electrons for the catalytic cycle are likely produced from a reduced photosensitizer (PS^-) (**Scheme 2.1**).

Scheme 2.1 Two possible pathways of a photocatalyst (**CAT**) (1) as either an integrated photosensitizer or with addition of a photosensitizer (**PS**) (2).

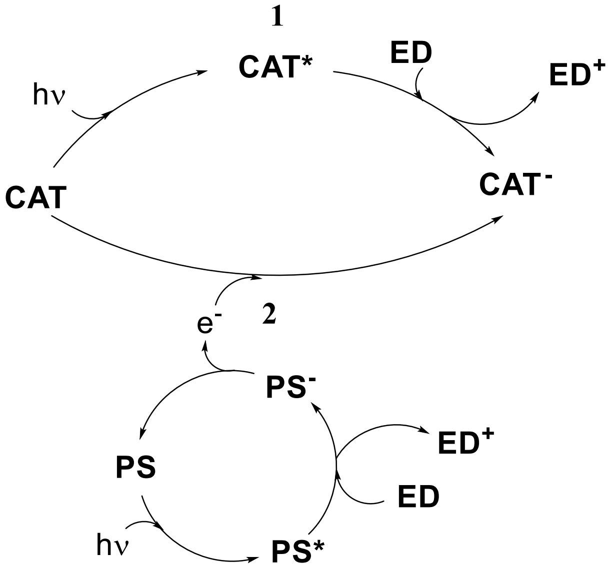

With the discovery of *fac*-Re(bpy)$(CO)_3$X (bipy = 2,2′-bipyridine, X = halide) complexes as photocatalysts for the reduction of CO_2 over 30 years ago, they remain benchmarks in this field today. These catalysts are selective for CO production using triethanolamine (TEOA) as an electron donor and established the ongoing investigation of related *fac*-[Re(α-diimine)$(CO)_3$X] complexes.[6-10] This continued with the introduction of the manganese analogue *fac*-[Mn(bpy)$(CO)_3$Br] maintaining a possible importance of group 7 complexes in this field; however, this complex required an added photosensitizer, $Ru(bpy)_3^{2+}$,[11,12] unlike the *fac*-Re(bpy)$(CO)_3$X catalysts, which are particularly unique in their ability to function as integrated PS and CAT, thus allowing light absorption and catalysis with one species. These features continue to drive the vigorous search for PS integrated catalysts yet realization of this goal remains rather limited.[13-17] The search for novel ligand frameworks led to the development of new complexes such as the N-heterocyclic carbene (NHC) Re(I) complexes, which also display the dual function of CAT and PS species for the reduction of CO_2 to CO (**Figure 2.1**).[18,19]

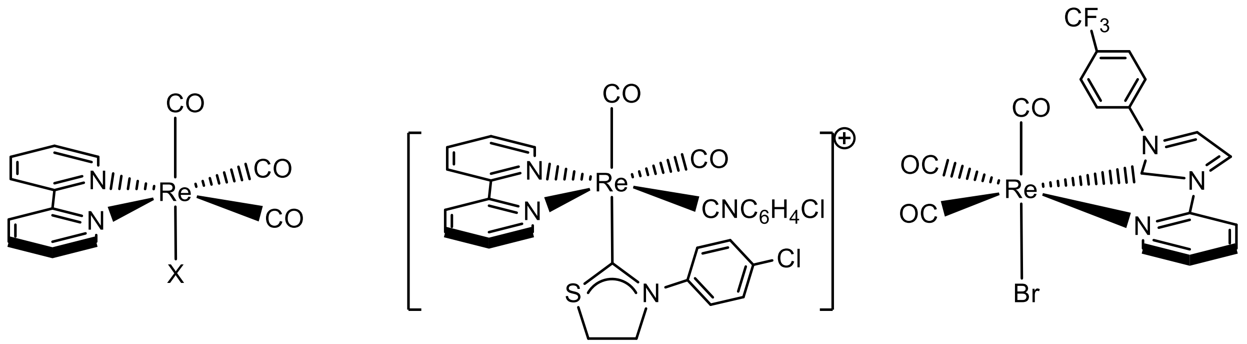

$Re(bpy)(CO)_3X$ "Re(N,S-NHC)" "$Re(Py\text{-}NHC\text{-}PhCF_3)$"

Figure 2.1 Known Re(I) complexes as integrated PS and CAT

Overview

Recently, we have worked on the photocatalytic reduction of CO_2 using Mn, Re and Ru[20,21] complexes that employed variations of phosphino aminopyridine ligands with the requirement of an additional PS in tris(2,2'-bipyridine)ruthenium(II) hexafluorophosphate ($Ru(bpy)_3^{2+}$). However, with the aim of discovering new environments for CO_2 integrated photosensitizer/catalyst reduction species and possibly recognizing new reaction pathways for this transformation as well as hoping to move away from the employment of a photosensitizer, which also contained one of the rare and expensive noble metals, we targeted the preparation of two bis(α-diimine) Re(I) carbonyl complexes, **2.1^+OTf$^-$** and **2.2^+OTf$^-$**. Maintaining this octahedral geometry, we also decided to assess a diamine diphosphino Re(I) carbonyl complex, **$2.3^+PF_6^-$**, using a conjugated diphosphine, cis-1,2-Bis(diphenylphosphino)ethylene (c-dppene). One other beneficial aspect is the use of commercially available ligands (**Figure 2.2**). Based on the knowledge of the catalytic capabilities of the mono(α-diimine) species (e.g. [$Re(bpy)(CO)_3X$]) as well as the related aptitude of the mono- and bis(α-diimine) Ru species, *cis,trans*-$Ru(N\text{^}N)(CO)_2Cl_2$ and cis-$[Ru(N\text{^}N)_2(CO)_2]^{2+}$, in catalysis,[22-25] we were encouraged to pursue these targets.

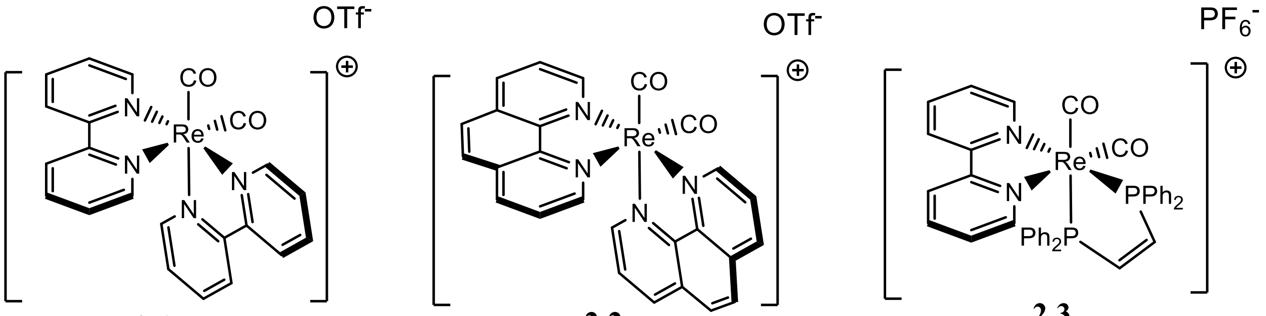

2.1 **2.2** **2.3**

Figure 2.2 Complexes **2.1^{+}OTf^{-}**, **2.2^{+}OTf^{-}** and **2.3^{+}PF$_6^{+}$**

We now provide the first documentation of this coordination environment[26] as possible photocatalysts with integrated photosensitizer ability for CO_2 reduction as well as revealing a notable change in a switch of product selectivity from CO to HCO_2H.

Results and Discussion:

Synthesis

Upon a literature inspection we were able to follow procedures for the synthesis of complexes *cis*-$[Re(CO)_2(bpy)_2](CF_3SO_3)$ (**2.1$^+$OTf$^-$**), *cis*-$[Re(CO)_2(phen)_2](CF_3SO_3)$ (**2.2$^+$OTf$^-$**) and *cis*-$[Re(CO)_2($*c*-dppene$)(bpy)](PF_6)$ (**2.3$^+$PF$_6^+$**) as detailed by *Smithback et al.*.[27] Although some central physical characterization was known, no reactivity was conveyed.

The preparation for **2.1$^+$OTf$^-$** and **2.2$^+$OTf$^-$** involved the uncommon conditions of using a melt of 2,2′-bipyridine (**2.1$^+$OTf$^-$**) or 1,10-phenathroline (**2.2$^+$OTf$^-$**) as the solvent at $T \approx 275$ °C (**a**). This reflects the stability of *fac*-$[Re(N\text{^}N)(CO)_3X]$ and is consistent with the dominance of the mono-ligated compounds in Re(I) chemistry. Characterization was demonstrated through the spectroscopic analysis of both products. In particular, the ^1H and ^{13}C NMR spectra displayed the expected signals for the C_2 symmetric structures. Preparation of **2.3$^+$PF$_6^+$** required a less unusual approach in which 2,2'-bipyrdine is added to the reaction mixture with the synthesized *fac*-$Re(CO)_3($*c*-dppene$)Cl$ as well as potassium hexafluorophosphate (KPF_6) and undergoes a simple reflux (**b**).

Scheme 2.2 The synthetic methods used to prepare complexes **2.1**$^+$**OTf**$^-$, **2.2**$^+$**OTf**$^-$ and **2.3**$^+$**PF**$_6^-$

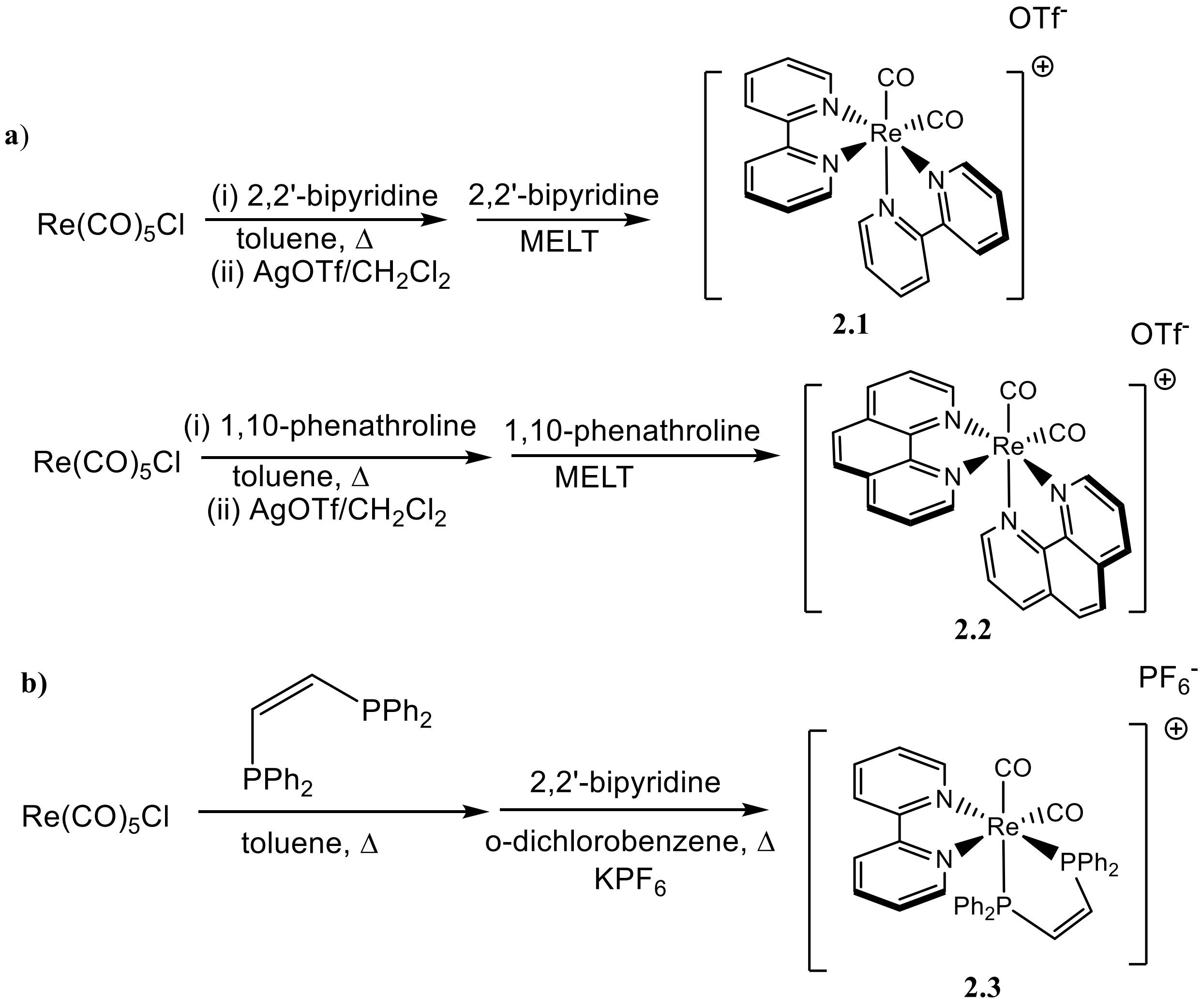

Electrochemistry

Before applying these complexes as photoreduction catalysts, we decided to look at some fundamental physical chemistry characterizations of **2.1**$^+$ using cyclic voltammetry. In acetonitrile, **2.1**$^+$ displayed reversible one electron reductions at $E_{1/2}$ = -1.67 V and -1.90 V *vs.* Fc/Fc$^+$ and an irreversible reduction at more negative potential at -2.63 V as seen in **Figure 2.3**. However, when the solvent was substituted for dimethylacetamide (DMA) and dimethylformamide (DMF) we observed a shift to less negative potentials and more importantly, shifted more positive in the presence of TEOA when recorded in a solution of 4:1 DMF:TEOA. This environment presented the $E_{1/2}$ values of -1.46 V and -1.70 V (**Figure 2.4**). This may be a contributing factor as to why an initial photocatalytic experiment done in CH_3CN produced no reduction products for CO_2 using **2.1**$^+$ (Entry 1 in **Table 2.1**).

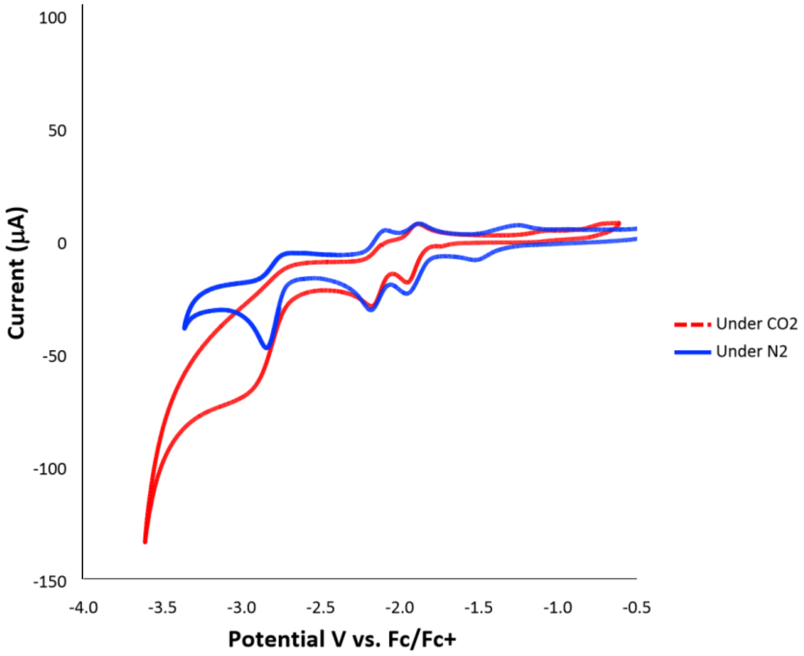

Figure 2.3 The cyclic voltammagram under reducing potentials of *cis*-Re(CO)$_2$(bipy)$_2$$^+OTf^-$ (**2.1$^+$OTf$^-$**) (1.0 mM) under N_2 (blue) or CO_2 (red) in CH_3CN with 0.1M tetrabutylammoniumhexafluorophosphate (TBAHFP) supporting electrolyte at a scan rate of 0.1 V/s *vs*. Fc/Fc$^+$.

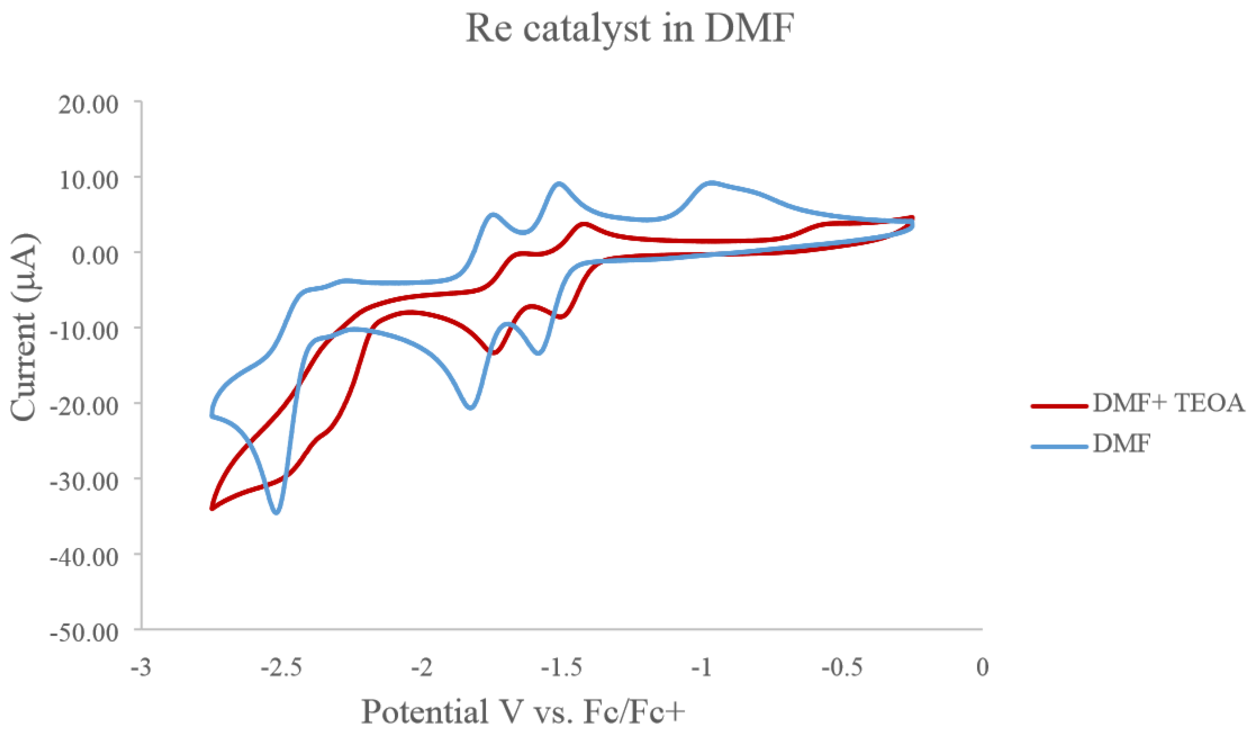

Figure 2.4 The cyclic voltammagram under reducing potentials of *cis*-Re(CO)$_2$(bipy)$_2$$^+OTf^-$ (**2.1$^+$OTf$^-$**) (1.0 mM) under N$_2$ in DMF (blue) or 4:1 DMF:TEOA (red) with 0.1M tetrabutylammoniumhexafluorophosphate (TBAHFP) supporting electrolyte at a scan rate of 0.1 V/s *vs.* Fc/Fc$^+$.

Photocatalytic Results

With the intention of using a blue LED light for the photocatalytic reactions, UV-vis electronic spectral characterizations were performed for **2.1$^+$**, **2.2$^+$** and **2.3$^+$**. A TD-DFT analysis using the integral equation formalism variant of the PCM model with CH_2Cl_2 as solvent confirmed MLCT (dπ–π*) absorptions at visible wavelengths of 388, 416, 434, 496, 498, and 538 nm for **2.1$^+$**; 398, 420, 442, 460, 506, 511 and 549 nm for **2.2$^+$**; 394, 440 and 449 nm for **2.3$^+$**. Consistent with these calculations is the appearance of the visible portion (350–800 nm) of the electronic spectrum of the three cationic species in DMF **Figure 2.12**.

Table 2.1 Summary of results for the photocatalytic CO_2 reduction with 1mM (5 µmol) **2.1**$^+$, **2.2**$^+$ and **2.3**$^+$ in 5mL of either 4:1 DMA/TEOA or 5 mL solution of 0.1 g BNAH in DMA. Solutions included 0.1mM (0.5 µmol) of catalyst if PS (R6G) was added. Irradiation with 405 nm light conducted on solution under a CO_2 atmosphere for 24 h.

Entry	Catalyst	Conc. (mM)	PS (1mM)	ED	HCOOH (µmol)	TON
1	**2.1**$^{+a}$	1	-	TEOA	-	-
2	**2.1**$^+$	1	-	TEOA	26.35	5.2
3	**2.1**$^+$	1	-	BNAH	19.42	3.9
4	**2.2**$^+$	1	-	TEOA	16.36	3.3
5	**2.2**$^+$	1	-	BNAH	31.56	6.3
6	**2.3**$^+$	1	-	TEOA	11.28	2.3
7	**2.3**$^+$	1	-	BNAH	10.53	2.1
8	**2.1**$^+$	0.1	R6G	TEOA	5.27	10.5
9	**2.2**$^+$	0.1	R6G	BNAH	4.38	8.8
10	**2.3**$^+$	0.1	R6G	TEOA	4.78	9.6

[a] *CH_3CN used as solvent*

The cationic complexes **2.1**$^+$, **2.2**$^+$ and **2.3**$^+$ were placed in CO_2 photocatalytic reduction conditions to test for reactivity. A typical setup included a 1mM (5mL) solution of the catalyst in dimethylacetamide (DMA) in a 20 mL sealed vial equipped with a magnetic stir bar and purged with CO_2. The vial was then irradiated with a 405 nm blue LED light for 24 hours. It should be noted that DMA was chosen over DMF (dimethylformamide) because of the documented production of formic acid from the degradation of DMF. Triethanolamine (TEOA) and 1-benzyl-1,4-dihyronicotinamide (BNAH) were both employed as the EDs due to their well-documented use in this field. In addition to the two-electron reduction of CO_2, this mechanism relies on a source of protons that is provided by the decay reactions of oxidized TEOA (**Scheme 2.3**) or BNAH. Results of these reactions are tabulated in **Table 2.1**.

Scheme 2.3 Proposed oxidative decay of TEOA as an electron and proton source of photocatalysis

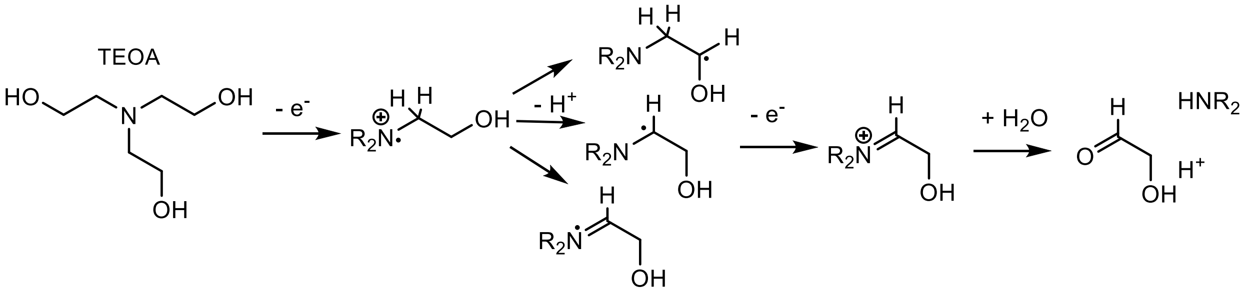

Two notable points can be observed in **Table 2.1**. First, the three cationic species exhibited photocatalytic CO_2 reduction in the absence of an added photosensitizer. Second, although the catalytic turnover (TON), which is the mole of the reduction product produced per mole of catalyst, wasn't as high as the other reported Re(I) CO_2 reduction catalysts, these compounds were unique for their selectivity for formate rather than CO.

When perceiving each catalyst distinctly, some observations can be noted. **2.1**$^+$ appears to favor TEOA over BNAH as an ED with a turnover number for formate of 5.2 to 3.9 (TEOA to BNAH), while **2.2**$^+$ seemed to have the opposite effect (3.3 to 6.3). **2.3**$^+$ was evidently a worse catalyst then both **2.1**$^+$ and **2.2**$^+$, while favoring neither ED. This could possibly be correlated with its low absorbance in blue light region (**Figure 2.12**)

Deciding to avoid the addition of common transition metal complexes photosensitizers, which often employ the more rare and expensive noble metals like Ru and Ir, we surveyed the literature and decided to apply an organic dye PS, rhodamine 6G (R6G), used in organic photocatalytic reduction with blue light.[28] This can be seen in entries 8, 9 and 10 for **2.1**$^+$, **2.2**$^+$ and **2.3**$^+$ respectively. In the presence of the added photosensitizer, formate was produced at almost twice the rate for **2.1**$^+$ and **2.2**$^+$ and over 4 times the turnover with **2.3**$^+$.

Lastly, definitive confirmation that the formic acid originated from photocatalytic CO_2 reduction was done by ^{13}C tracing. We purged the headspace with $^{13}CO_2$ of photoreaction vessel with **2.1**$^+$, Ru(bpy)$_3^{2+}$, and TEOA in DMA. The ^1H NMR data shown in **Figure 2.5** provided conclusive evidence that the formic acid observed in these experiments originated from $^{13}CO_2$, further stressing the noteworthy switch in product selectivity with the reported production of CO from all other Re α-diimine species.

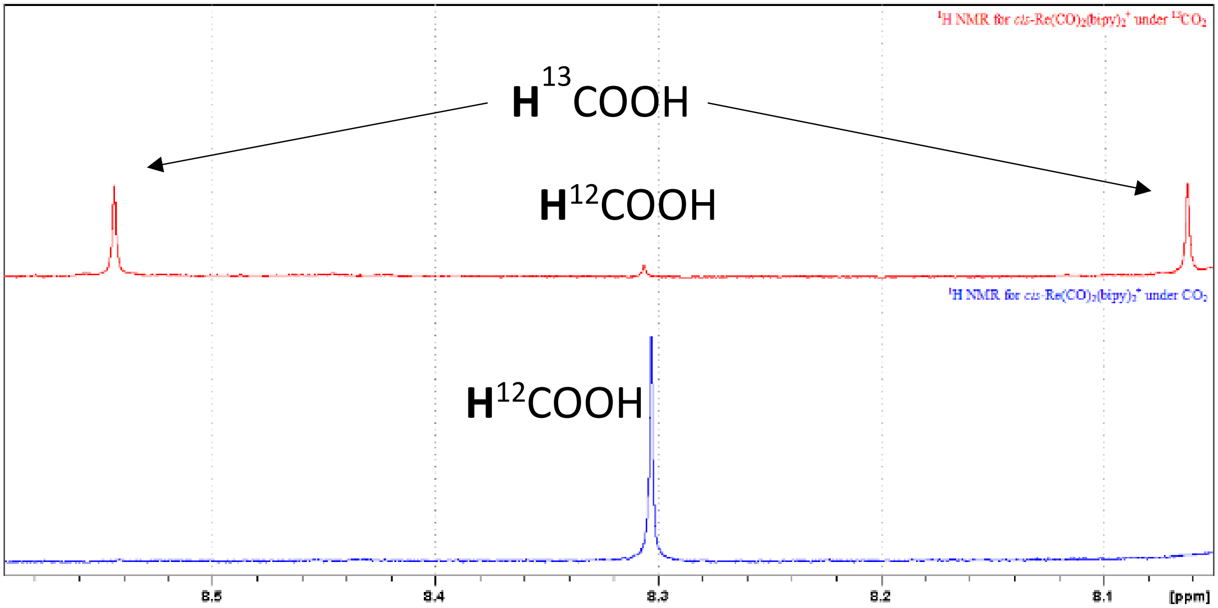

Figure 2.5 ^1H NMR spectra for the formyl HOOC-**H** proton of formic acid obtained from photocatalytic reduction of CO_2 using *cis*-[Re(CO)$_2$(bpy)$_2$](CF$_3$SO$_3$) (**2.1**), as the catalyst. The bottom spectrum was from reaction using unlabeled CO_2 and the top spectrum is from a reaction with labeled $^{13}CO_2$.

Proposed Mechanism

Based on literature precedent, the experimental observations and some DFT calculations, a proposed catalytic mechanism for HCO_2H production from the CO_2 photocatalytic reduction using complex **2.1**$^+$, and believed to be followed by **2.2**$^+$ and **2.3**$^+$ as well, is presented in **Scheme**

2.4. The photocatalytic reduction is believed to follow two pathways. The first is a photosensitizer electron generated catalysis coupled with a CO_2 reduction catalysis cycle. The electron production cycle provides the electrons to the catalyst. In the case of an integrated catalyst/photosensitizer, electrons for the catalytic cycle can come directly from the ED through electron transfer to a photoexcited **2.1**$^+$. When photosensitizer is added to the reaction, the electrons for the catalytic cycle are likely produced from a reduced PS (PS^-) by means of a oxidized ED to an excited state photosensitizer (PS^*). In addition to the two-electron reduction of CO_2, decay reactions of oxidized ED are the source of protons that is provided. The catalytic cycle represents the steps where the Re complex, **2.1**$^+$, catalytically reduces CO_2 using these provided electrons/protons. Generally (as stated in Chapter I), successful conversion of CO_2 to formate is proposed to proceed through a metal hydride intermediate (**2.1(H)**). The most energetically favored hydride intermediate computed is presented in **Figure 2.6.** DFT computationally optimized structure of the Re intermediates with the B3LYP functional and def2TZVP basis are presented in **Figures 2.7-2.11**. In summary the cycle begins with the transformation of **2.1**$^+$ to **2.1** by the two proposed routes, which itself undergoes a reduction and protonation to produce the metal-hydride, **2.1(H). 2.1(H**) can then insert CO_2 leading to a formato complex, **2.1(form)**, that eventually displaces the formate for CO, regenerating **2.1**$^+$and restarts the cycle.

Scheme 2.4 Proposed mechanism for the photocatalytic reduction of CO_2 using **2.1^+**

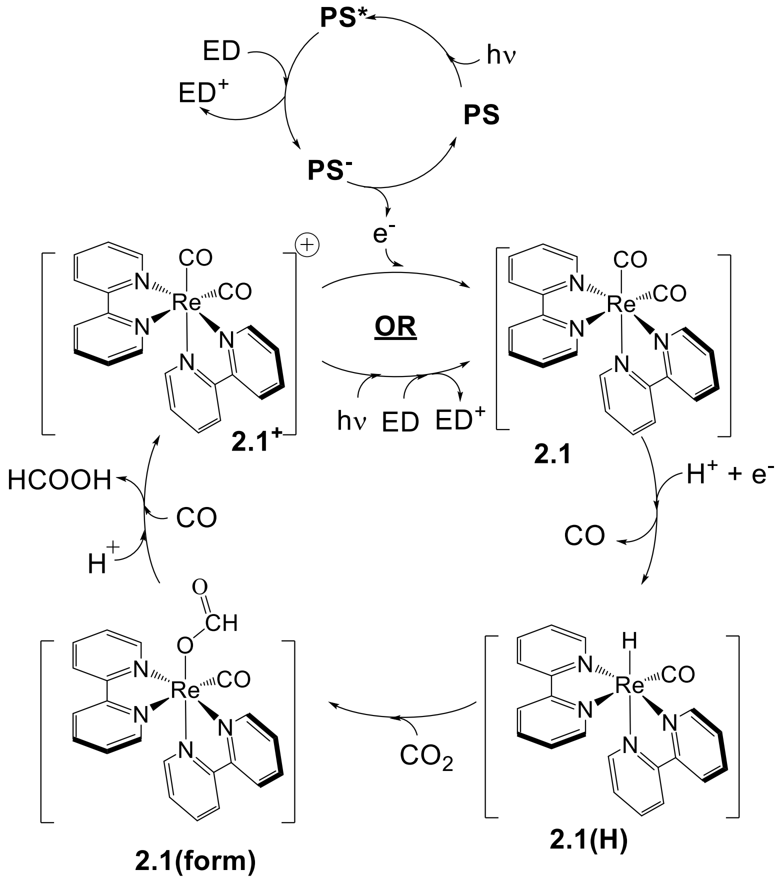

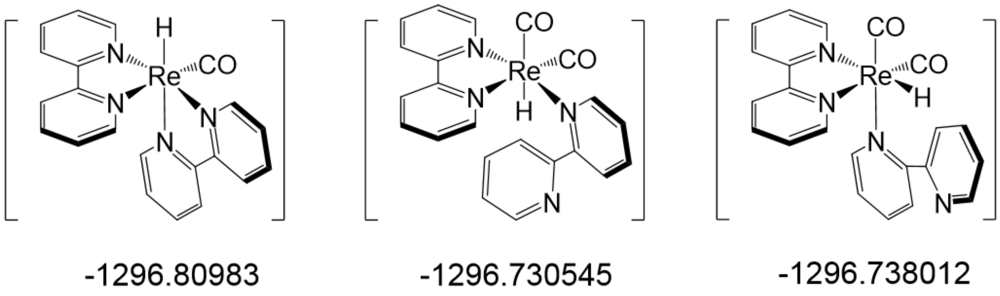

Figure 2.6 Representations of the three possible protonation products to yield Re-H intermediates that may arise in the catalytic cycle shown in **Scheme 2.4**. Each of these species was computationally optimized as a means of determining the most likely structure of proposed **2.1(H)**. DFT calculations used the B3LYP functional and the def2TZVP basis set. The results for the energies associated with each of these possibilities are indicated in Hartrees. This indicated that $[Re(CO)(bpy)_2H]$ was the lowest energy species and was thus used in the proposed cycle.

Conclusion:

This chapter has revealed functionally integrated photosensitizer/catalysts, *cis*-[Re(CO)$_2$(bpy)$_2$](CF$_3$SO$_3$) (**2.1$^+$OTf$^-$**), *cis*-[Re(CO)$_2$(phen)$_2$](CF$_3$SO$_3$) (**2.2$^+$OTf$^-$**) and *cis*-[Re(CO)$_2$(*c*-dppene)(bpy)](PF$_6$) (**2.3$^+$PF$_6$$^+$**), for the visible light photocatalytic reduction of CO$_2$. These complexes possess a structure that is unique among Re(I) photoreduction catalysts and unprecedent in the selective formation of formic acid, which have typically yielded CO as the reduction product. Although the catalytic turnovers were low, we were able to improve the performance with a commercial organic dye, which negates the need for the more commonly used noble metal photosensitizers. We are actively hoping to expand on this class of catalysts, presumably by the introduction of ligands that enhance the complex's ability to absorb more favorably in the visible region and withhold a longer excited state lifetime.

Experimental:

General Methods

Reagents and analytical grade solvents were purchased from Strem Chemicals or Sigma Aldrich and used without further purification. The ^{1}H, ^{13}C{^{1}H} and ^{31}P{^{1}H} NMR spectra were recorded at 400, 100 and 162 MHz respectively with chemical shifts reported in ppm using the residual protons of the NMR solvent as internal standards.

Typical Photocatalytic Experiments: A 20 mL glass vial with a magnetic stir bar was charged, in a nitrogen filled glovebox, with 4 mL of a solvent dimethylacetamide (DMA) or acetonitrile (MeCN) that contained catalyst, photosensitizer (R6G) (if necessary) and approximately 1mL TEOA as an electron donor or 5 mL solvent and 100 mg BNAH as an electron donor. The vial was sealed and removed from the glovebox. The solution was purged with CO_2 for 15-20 minutes and irradiated using a 405 nm LED light (radiant flux at 700 mA of 1050 mW) for 24 hours. After irradiation, carbon monoxide and hydrogen production were measured using an Agilent 7820A gas chromatograph (GC) with an Agilent select permanent gases column and equipped with a thermal conductivity detector (TCD). The liquid products from the photocatalytic reactions were analyzed using ^{1}H NMR. An aliquot (100 µL) was removed from the irradiated samples and was mixed in an NMR tube with D_2O containing a known amount of dimethyl sulfone (DMS) (400 µL) as internal standard. The sample was mixed well and the ^{1}H NMR spectra were collected. Using the ratios of the integrated values for the formic acid ($\delta \approx 8.1$ppm) and integrated values of DMS, the amount of formic acid was determined. A similar experiment was carried out using catalyst employing ^{13}CO2 (99% ^{13}C and <3% ^{18}O from Sigma-Aldrich) at a pressure of 20 PSI. The mixture was stirred and exposed to 405 nm blue LED for 24 h, and the liquid phase products were analyzed as described.

Electrochemistry: Electrochemical experiments were carried out in a single compartment cell wrapped with aluminum foil using a VersaSTAT 3 (Princeton Applied Research) potentiostat. Samples were prepared in a glovebox, sealed, removed from the glovebox and connected to a Schlenk line and maintained under a nitrogen atmosphere. A conventional three electrode system was employed consisting of a glassy carbon working electrode (diameter = 0.3 cm), a Pt wire as the auxiliary electrode, and an Ag wire as a pseudo-reference electrode. Ferrocene was added as a reference compound and potentials were referred to the redox potential of ferrocene (Fc)/ferrocenium ion (Fc^+) as an internal standard. Dried acetonitrile and DMA were purchased from Sigma Aldrich and stored on molecular sieves in glove-box. Tetrabutylammonium hexafluorophosphate (TBAHFP), the supporting electrolyte, was crystallized two times with methanol, dried in vacuum at 90 °C for 24 h before used and stored in a glovebox. The electrolyte solution, 0.1 M TBAHFP in CH_3CN or DMA, was saturated with N_2 by purging with N_2 for 10 min prior to each experiment. The typical concentration of catalyst was 1 mM (10 mL acetonitrile or DMA) in each experiment.

Computational Details: Optimized structures were obtained from density functional theory (DFT) computations using Gaussian 09. The B3LYP functional and def2TZVP basis set was used for all atoms.

Syntheses

Synthesis of *cis*-Re(CO)$_2$(bipy)$_2$$^+OTF^-$ (2.1$^+$OTf$^-$):[27] Complex **2.1$^+$OTf** was synthesized according to the literature from the *fac*-Re(bpy)(CO)$_3$(CF$_3$SO$_3$) (**A**). Complex **A** (1.0 g, 1.738 mmol) was mixed with a large excess of bpy (≈ 1.25g) with a magnetic stir bar in a Schlenk tube, which was capped with a septum and purged with N_2. The reaction mixture was magnetically stirred and heated to reflux for 4 h during which time a red solid appeared. The reaction mixture was cooled and dissolved in CH_2Cl_2 to be transferred to a round bottom flask and the solvent was removed by evaporation under vacuum. Purification was achieved by column chromatography with CH_2Cl_2/CH_3CN mixtures. Yield: 1.03 g (84%). ^{1}H NMR (δ /ppm, CD3CN): 9.42 (d, 2H), 8.46 (d, 2H), 8.41 (d, 2H), 8.13 (dt, 2H), 8.02 (dt, 2H), 7.63 (m, 2H), 7.41 (dd, 2H), 7.33 (m, 2H). Analysis cald for $C_{23}H_{16}F_3N_4O_5ReS$: C, 39.26; H, 2.29; N, 7.96; Found: C 39.34; H 2.13; N 8.06.

Crystals suitable for X-ray analysis were grown by diffusion of saturated CH_2Cl_2 solution in CH_3CN. The structure is shown in **Figure 2.7**.

Synthesis of *cis*-[Re(CO)$_2$(phen)$_2$](CF$_3$SO$_3$) (2.2$^+$OTf $^-$):[27] Complex **2.2$^+$OTf** was synthesized according to the literature from the *fac*-Re(phen)(CO)$_3$(CF$_3$SO$_3$) (**B**) following the same procedure as **2.1$^+$OTf$^-$**, except using complex **B** (1.0 g, 1.67 mmol) was mixed with a large excess of phen (≈ 1.25g) for 5 hrs. Yield: 0.992 g (79%). ^{1}H NMR (δ /ppm, CD3CN): 9.93 (dd, 2H), 8.74 (dd, 2H), 8.50 (dd, 2H), 8.22 (d, 2H), 8.08 (d, 2H), 8.01 (dd, 2H), 7.57 (dd, 2H), 7.47 (dd, 2H). Analysis cald for $C_{23}H_{16}F_3N_4O_5ReS$: C, 39.26; H, 2.29; N, 7.96; Found: C 39.34; H 2.13; N 8.06.

Synthesis of *cis*-[Re(CO)$_2$(c-dppene)(bpy)](PF$_6$) (2.3$^+$PF$_6$$^+$):[27] Complex **2.3$^+PF_6$$^+$** was synthesized according to the literature from the *fac*-Re(c-dppene)(CO)$_3$Cl (**C**). Complex **C** (0.300 g, 0.426 mmol), KPF_6 (0.083 g, 0.45 mmol) and bpy (0.075 g, 0.0.46 mmol) were added to a round bottom flask with 20 ml of ODB. The flask was covered with aluminum foil and the solution was purged with nitrogen, then set to reflux for 7hrs. The solution was cooled and then filtered through a Celite slurry to remove KCl precipitate. The filtrate was transferred to another round bottom flask and the solvent was reduced. Diethyl ether was added to the solution and the flask was stored in the freezer. An orange solid was isolated and dried. Yield: 0.278 g (69%). The ^{1}H NMR, UV-visible of the reported complex. ^{1}H NMR (δ /ppm, CD_3CN): 9.60 (d, 1H), 8.52 (dt, 1H), 8.13 (m, 2.5H), 8.01 (m, 2.5H), 7.79 (d, 1H), 7.64 (m, 7H), 7.51 (m, 4H), 7.38 (m, 5H), 7.09 (m, 1H), 6.86 (m, 3H), 6.18 (m, 2H). $^{31}P\{^{1}H\}$ NMR (δ/ppm, CD_3CN): 52.6 (d), 41.9 (d).

Appendix:

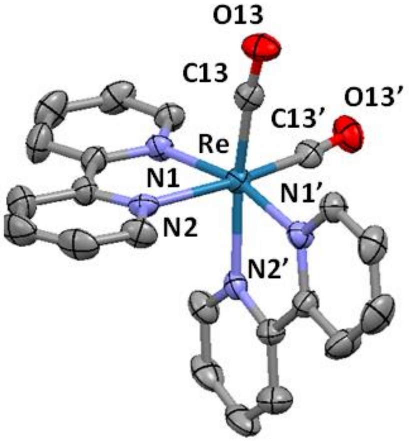

Figure 2.7 Structural representation for compound cis-$Re(CO)_2(bipy)_2^+$ (**2.1**$^+$) obtained from X-ray analysis. Hydrogen atoms and counter anion (OTf^-) are omitted for clarity.

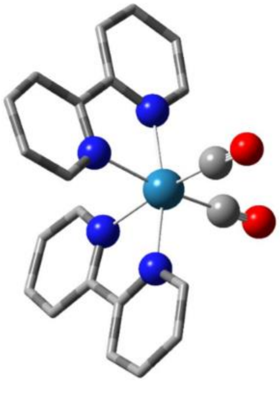

Figure 2.8 A ball and stick structural representation for the computationally optimized cis-$Re(CO)_2(bipy)_2^+$ (**2.1**$^+$). DFT calculations used the B3LYP functional and the def2TZVP basis set. Hydrogen atoms are not shown for clarity.

Table 2.2 A comparison of metal–ligand distances (Å) from the experimental single crystal X-ray analysis and from the computationally optimized structures (**2.1**$^+$) and and the single electron reduction product (**2.1**).

Bond/angle	**1$^+$ (X-ray)**	**1$^+$ (Computed)**	**1 (Computed)**
Re-N trans CO	2.165(3)	2.215	2.2028
Re-N trans N	2.121(3)	2.147	2.1319
Re-CO	1.883(5)	1.921	1.9156
N_{py}-Re-N_{py}	75.15(13)	74.67	75.326

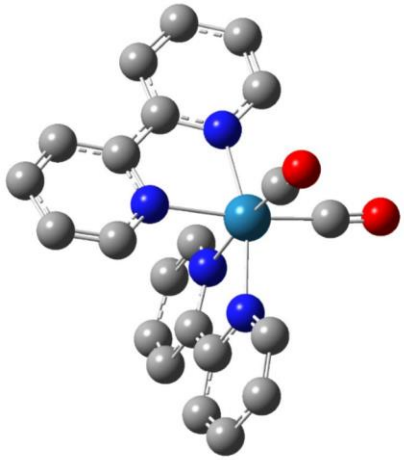

Figure 2.9 A ball and stick structural representation for the computationally optimized reduced compound *cis*-Re(CO)$_2$(bipy)$_2$ (**2.1**). DFT calculations used the B3LYP functional and the def2TZVP basis set. Hydrogen atoms are not shown for clarity.

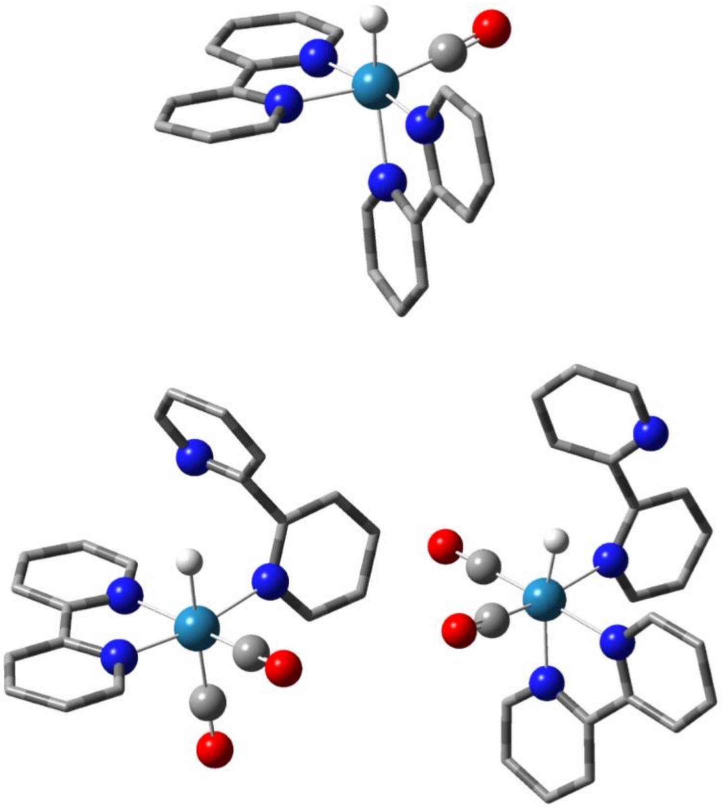

Figure 2.10 Ball and stick structural representations for the two isomers of the computationally optimized $[Re(CO)_2(bipy)_2H]$ and the compound (**2.1(H)**) as the proposed intermediate in the catalytic cycle (see **Scheme 2.4** and **Figure 2.6**). DFT calculations used the B3LYP functional and the def2TZVP basis set. Hydrogen atoms are not shown for clarity.

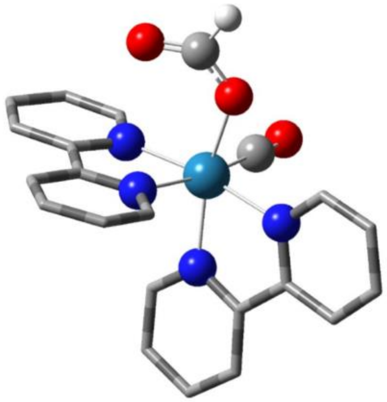

Figure 2.11 A ball and stick structural representation for the computationally optimized $[Re(CO)_2(bipy)_2OCOH]$compound **2.1(form)**. DFT calculations used the B3LYP functional and the def2TZVP basis set. Hydrogen atoms are not shown for clarity.

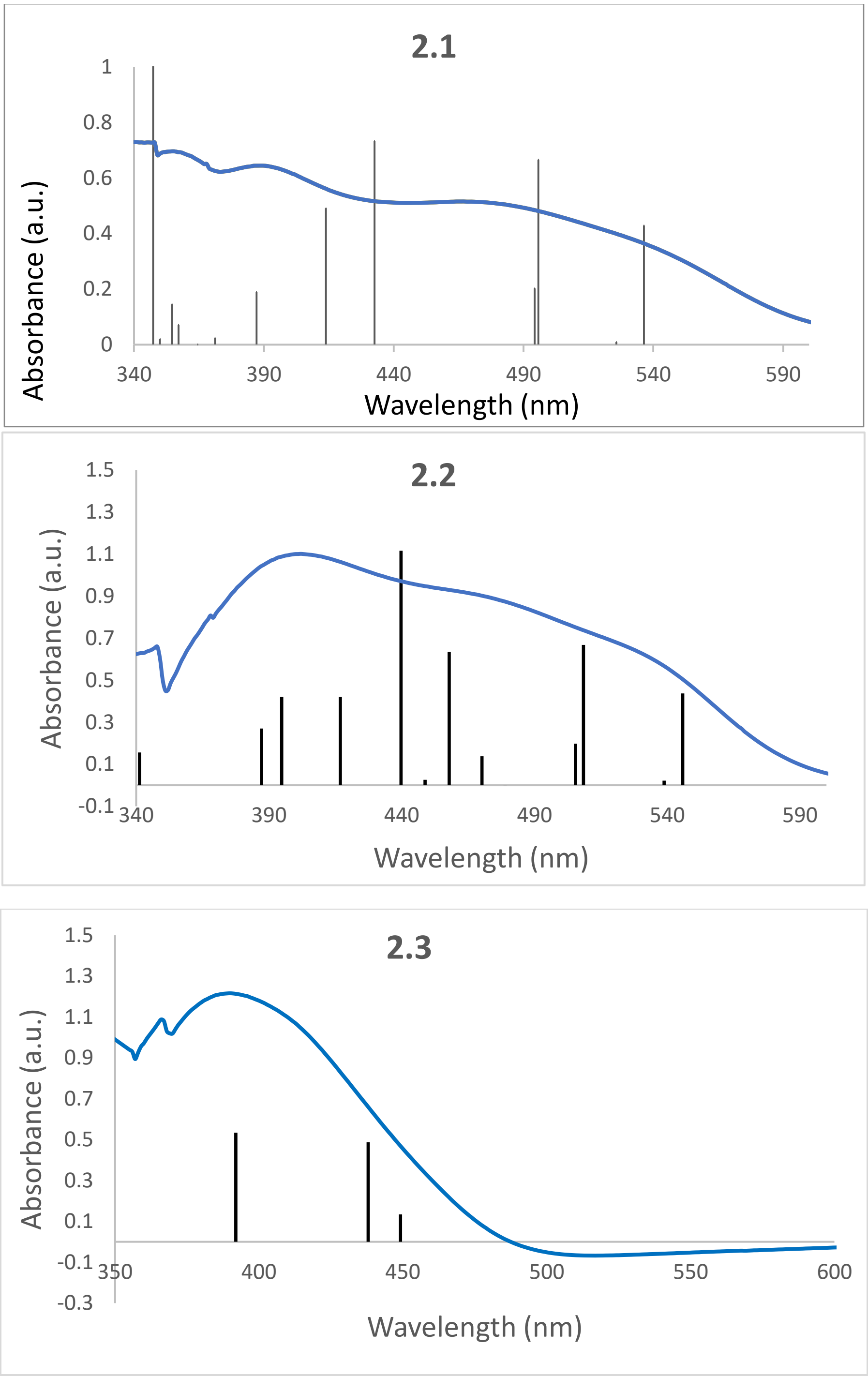

Figure 2.12 UV-vis of complexes **2.1**, **2.2** and **2.3** (blue). Spectra obtained in DMF solvent. TD-DFT computed absorbances in CH_2Cl_2 are branded on the spectra (black).

References:

1) K. Sordakis, C. Tang, L. K. Vogt, H. Junge, P. J. Dyson, M. Beller and G. Laurenczy, Chem. Rev., 2018, **118**, 372.
2) H. Zhong, M. Iguchi, M. Chatterjee, Y. Himeda, Q. Xu and H. Kawanami , Adv. Sustainable Syst., 2018, 1700161.
3) J. L. Inglis, B. J. MacLean, M. T. Pryce and J. G. Vos, *Coord. Chem. Rev.*, 2012, **256**, 2571.
4) C. Costentin, M. Robert, J.-M. Savéant, *Chem. Soc. Rev.*, 2013, **42**, 2423.
5) J. Schneider, H. Jia, J. T. Muckerman and E. Fujita, *Chem. Soc. Rev.*, 2012, **41**, 2036.
6) J. Hawecker, J. Lehn, R. Ziessel, *Helv. Chim. Acta*, 1986, **69**, 1990.
7) J. Hawecker, J.-M. Lehn and R. Ziessel, *J. Chem. Soc., Chem. Commun.*, 1984, **984**, 328
8) P. L. Cheung, C. W. Machan, A. Y. S. Malkhasian , J. Agarwal, C. P. Kubiak , *Inorg. Chem.*, 2016, **55**, 3192.
9) J. X. Zhang, C. Y. Hu, W. Wang, H. Wang, Z. Y. Bian, *Appl. Catal., A*, 2016, **522**, 145.
10) H. Fei, M. D. Sampson, Y. Lee, C. P. Kubiak, S. M. Cohen, *Inorg. Chem.*, 2015, **54** , 6821.
11) M. Bourrez , F. Molton , S. Chardon-Noblat A. Deronzier , *Angew. Chem., Int. Ed.*, 2011, **50** , 9903.
12) M. Bourrez, M. Orio, F. Molton, H. Vezin, C. Duboc, A. Deronzier and S. Chardon-Noblat, *Angew. Chem., Int. Ed.*, 2014, **53**, 240.
13) S. K. Lee , M. Kondo , M. Okamura , T. Enomoto , G. Nakamura and S. Masaoka , *J. Am. Chem. Soc.*, 2018, **140** , 16899.
14) J. Hawecker , J. Lehn, R. Ziessel , *J. Chem. Soc., Chem. Commun.*, 1983, 536.
15) H. Takeda, K. Koike, H. Inoue and O. Ishitani, *J. Am. Chem. Soc.*, 2008, **130**, 2023.

16) P. Kurz , B. Probst, B. Spingler and R. Alberto , *Eur. J. Inorg. Chem.*, 2006, 2966.

17) H. Rao, J. Bonin, M. Robert, *Chem. Commun.*, 2017, **53**, 2830.

18) A. J. Huckaba , E. A. Sharpe, J. H. Delcamp , *Inorg. Chem.*, 2016, **55**, 682.

19) A. Maurin, C. Ng, L. Chen, T. Lau, M. Robert and C. Ko, *Dalton Trans.*, 2016, **45**, 14524.

20) Y. Hameed, B. Gabidullin, D. Richeson, *Inorg. Chem.* 2018, **57** (21), 13092.

21) Y. Hameed, G. K. Gao, J. S. Ovens, B. Gabidullin, D. Richeson, *ChemSusChem*, 2019, **12**, 3453.

22) Y. Kuramochi, J. Itabashi, K. Fukaya, A. Enomoto, M. Yoshida and H. Ishida, *Chem. Sci.*, 2015, **6**, 3063.

23) K. Sekizawa, K. Maeda, K. Domen, K. Koike and O. Ishitani, *J. Am. Chem. Soc.*, 2013, **135**, 4596.

24) H. Ishida, T. Terada, K. Tanaka, T. Tanaka, *Inorg. Chem.*, 1990, **29**, 905.

25) Y. Kuramochi , M. Kamiya, H. Ishida , *Inorg. Chem.*, 2014, **53**, 3326.

26) Y. Hameed, P. Berro, B. Gabidullin, D. Richeson, *Chem. Commun.*, 2019, **55**, 1104.

27) J. L. Smithback, J. B. Helms, E. Schutte, S. M. Woessner, B. P. Sullivan, *Inorg. Chem.*, 2006, **45**, 2163.

28) I. Ghosh, B. Konig, *Angew. Chem. Int. Ed.*, 2016, **55**, 7676.

Chapter III

Electrocatalytic Zn(II) Complexes for CO_2 Reduction

Introduction:

A broad assortment of homogeneous transition-metal complexes (e.g., Mn-, Fe-, Co-, Ni-, Cu-, Ru-, and Re-based complexes), have been explored for catalyzing reduction of CO_2 under both electrochemical and photochemical conditions.[1–6] Both from a sustainability point of view and due to the low toxicity of first row transition metals, useful catalyst for CO_2 reduction built on these metal centers a critical direction that needs to be explored.

Zn Catalysts

Among the 3d metals, perhaps not surprising, Zn is nearly absent from the metals that have been used for CO_2 reduction. This is likely because Zn is normally not viewed as a redox active center. However, Zn does have some important documented roles in catalyzed reactions. For example, Zn has a key role in the catalytic preparation of polycarbonates and cyclic carbonates.[78] These reactions involves the capture of CO_2 and rely on the Lewis acidity of Zn(II). Furthermore, fixation of CO_2 with square planar Zn(II) supported by tetraazacycloalkanes has been reported.

These compounds, in the presence of alcohols ROH and base can reversibly trap CO_2 as zinc alkyl carbonates (ZnO_2COR).[9–11]

Zinc bromide was used as a catalyst in a recently reported conversion of CO_2 to CO with the parallel oxidation of phosphine.[12] Complexes of Zn have been used to catalyze hydrogenation and hydrosilylations. These reduction reactions rely on the formation and reactivity of a Zn-H moiety as a key step of the mechanism.[13]

Related and more pertinent to our goals is the hydrosilylation of CO_2 using [tris(2-pyridylthio)methyl]zinc hydride, [κ^3-Tptm]ZnH, **A** (**Scheme 3.1**).[14] This catalyst is capable of performing hydrosilylation of aldehydes, ketones, and carbon dioxide. Specifically, [κ^3-Tptm]ZnH (**A**) catalyzes the formation of triethoxysilyl formate via hydrosilylation of carbon dioxide with triethoxysilane.[14]

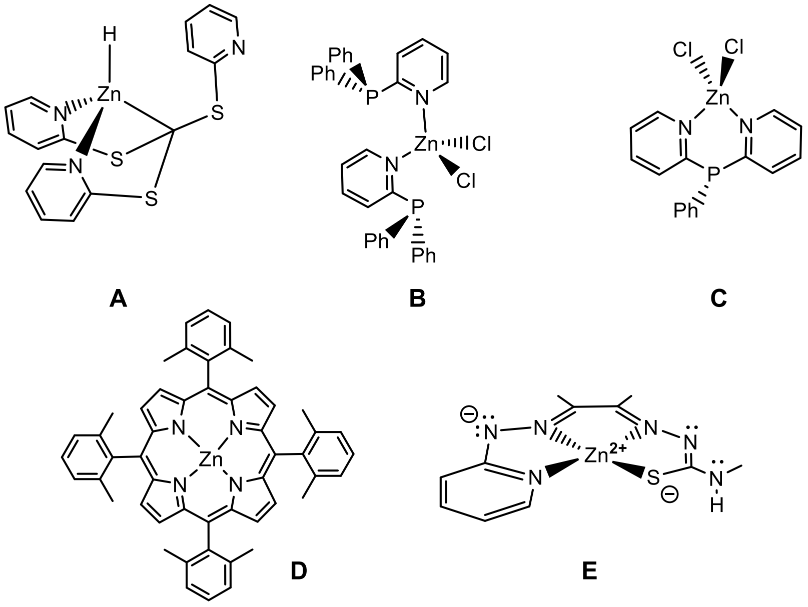

Scheme 3.1 The reported Zn catalysts for the reduction of CO_2.

There are only three reports of electrocatalytic CO_2 reduction using Zn(II) and these employed the complexes **B**, **D**, and **E** in Scheme **3.1**. A heterogenized Zn porphyrin complex **D** was deposited on a carbon fiber and subsequently used for electrocatalytic reduction in a mixed H_2O:DMF solvent.[15] The Zn cation is reported to be crucial for activity, however, it appears that the oxidation state of the metal remains fixed throughout the catalytic cycle. The authors argue that the reactivity of the noninnocent redox-active ligands can reversibly store reducing equivalents and facilitate catalytic conversion of CO_2.

Another electrochemical reduction involved pyridylphosphine ligated Zn(II) centers.[16] The two related complexes **B** and **C** were reported but only compound **B** was active in electrocatalytic reduction of CO_2. Cyclic voltammetry of **B** under Ar showed an irreversible one-electron reduction at −2.03 V vs Fc^+/Fc. Current enhancement of this reduction was observed when the CV was repeated under a CO_2 atmosphere, indicating electrocatalysis. When electrolysis was carried out with **B** under CO_2 and an applied potential of -1.8V (vs Fc^+/Fc), CO formation was observed. However, no quantification of this reduction was reported. The authors proposed a mechanism in which the free phosphorus centers participated in a nucleophilic attack at the carbon of CO_2, forming an adduct while the Zn-center behaved solely as a Lewis acid. The greater rigidity and less flexible chelating ligand for **C** was suggested to hinder CO_2 access to the lone pair of the phosphorus atom and given as the reason that this complex did not react with CO_2.

Compound **E,** Zn(DMTH) (DMTH = diacetyl-2-(4-methyl-3-thiosemicarbazonate)-3-(2-pyridinehydrazonato), presented a square planar Zn (II) complex with a tetracoordinate dianionic ligand that was reported to react with methanol to protonate the noncoordinating nitrogen of the hydrazonepyridine moiety and yield a methoxide complex, Zn(HDMTH)(OCH_3). The Zn-methoxide activated CO_2 by insertion into the Zn-OMe bond to make a methylcarbonate species.

Subsequent reduction of the carbonate by chemical or electrochemical hydride sources was reported to generate formate HCO_2^- and release CH_3OH.[17] The chemical hydride source employed in this reaction was $NaBH_4$. Two electrochemical methods were also reported. One relied on the use of a Pt working anode to generate a Pt-H intermediate that was intercepted by the methylcarbonate intermediate, Zn(HDMTH)(CO_3CH_3). The Pt electrode based approach required a potential of −2.00 V vs Fc^+/Fc and after 24 h an analysis of the reaction mixture by ^1H NMR confirmed the presence of HCO_2^-. An alternate electrochemical approach took advantage of the ability of Zn(DMTH) to function as an electrocatalyst for ligand-centered proton reduction in acetic acid to generate hydrogen.[18] In the presence of acetic acid, complex **E** is protonated at the noncoordinating 2-pyridylhydrazonato N site, the same internal base required for CO_2 fixation, to yield the active catalyst Zn(HL)OAc.[18] In order to observe productive CO_2 reduction, it appears that Zn(HDMTH)(CO_3CH_3) must first be generated by exposing Zn(HDMTH)(OCH_3) to CO_2 followed by addition of acetic acid. Catalytic current was observed at −2.37 V vs. Fc^+/Fc resulting in observation of H_2 in the reaction headspace (GC) along with formate in the solution (^1H NMR).

Overview

In this chapter, we will explore the electrochemical reactivity under reduction potentials of Zn(II) phosphino-pyridyl complexes. Our first targets for investigating the potential of Zn complexes for electrocatalytic CO_2 reduction were species represented by **3.1-3.4**. Although only the methyl substituted amine (N-Me) compounds, **3.1** and **3.2**, were electrochemically analyzed for CO_2 reduction, the hydro-amine (N-H) analogues, **3.3** and **3.4**, were also synthesized for comparison. We considered the N-H species might have complicating reactivity.

Results and Discusssion:

Synthesis and Structural Analysis

As anticipated, the direct room temperature reaction of $ZnBr_2$ with a stoichiometric quantity of the neutral pincer ligand, N,N′-bis(diphenylphosphino)-2,6-di(methylamino)pyridine 2,6-$\{Ph_2PNMe\}_2(NC_5H_3)$ (“PN^3P”) produced a new complex **3.1** as a colorless precipitate that was purified by crystallization from CH_2Cl_2 (**Scheme 3.2**). The ^1H, ^{13}C and ^{31}P NMR spectra of this complex all pointed to a symmetrical coordination of the ligand in complex **3.1**. In particular, the spectra displayed a single proton resonance for the N-Me groups as well as symmetrical signals for the pyridyl group and the PPh_2 moieties. Definitive structural confirmation was provided by single crystal X-ray analysis of this complex.

Scheme 3.2 Synthesis of **3.1**

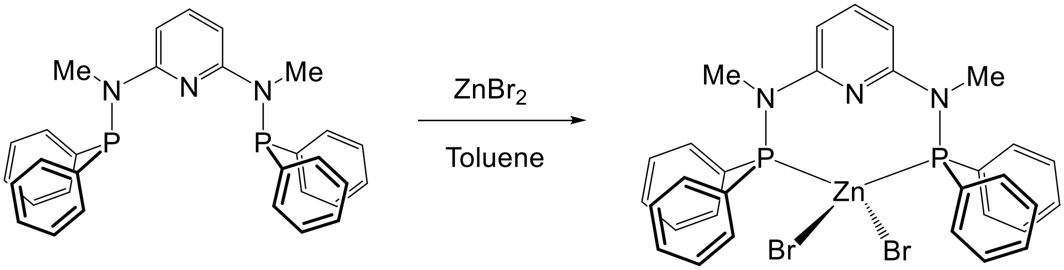

3.1

Figure 3.1 provides a representation of the X-ray crystal structure of [Zn(2,6-$\{Ph_2PNMe\}_2(NC_5H_3)Br_2$] (**3.1**) and established this complex as a four coordinate Zn(II) dibromide complex. In this case the potentially tridentate ligand bonds to the $ZnBr_2$ unit only through the two phosphine groups that flank the central pyridyl group. This results in a bidentate ligand coordination while the pyridyl-N remained uncoordinated. Selected metrical parameters for **3.1** are given in **Table 3.9** and confirm the symmetrical coordination of the PN^3P ligand with two identical Zn-P distances (Zn-P(1) 2.424(3) Å, Zn-P(2) 2.42(3) Å) and only slightly different Zn-Br linkages (Zn-Br(1) 2.4016(13) Å, Zn-Br(2) 2.3868(15) Å). These bond distances are in-line with reported Zn bond distances.[19] For example the complex $[ZnBr_3(PPh_3)]^-$ displayed Zn-P 2.425(9) Å and average Zn-Br of 2.38 Å. [20] The Zn coordination geometry is appropriately categorized as pseudo-tetrahedral. Although the angles range from 101.92(8)° to 115.50(5)°, the average for the six angles around the Zn center are 109.5° and the N(1) and N(3) are planar with Σ angles equaling 360°.

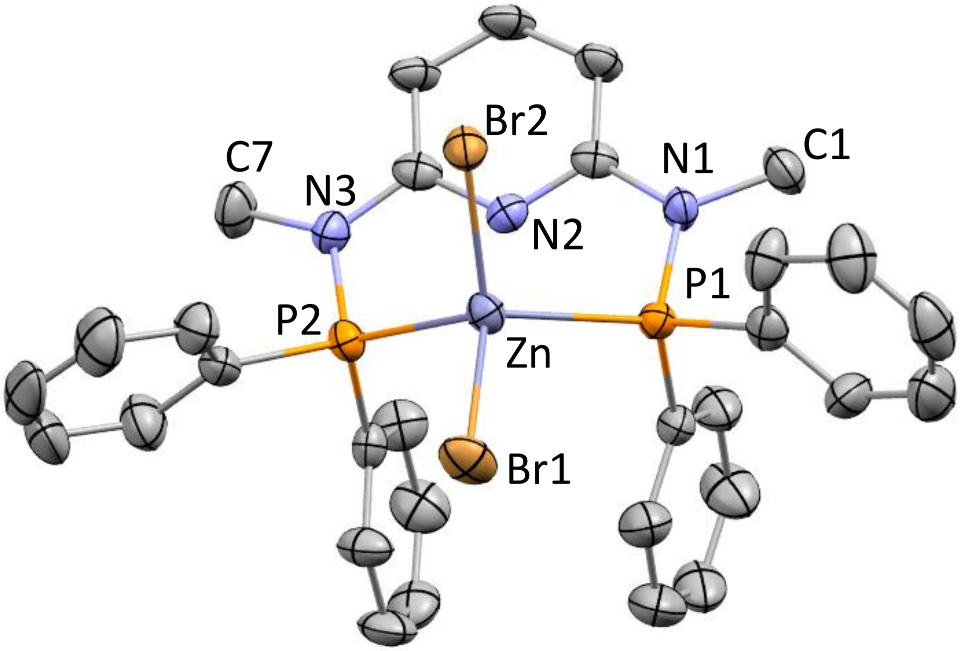

Figure 3.1 Structural representation for the compound **$[Zn(2,6\text{-}\{Ph_2PNMe\}_2(NC_5H_3)Br_2]$** (**3.1**) obtained from single crystal X-ray analysis. Hydrogen atoms are omitted for clarity.

The pyridyl-N(2) center is beyond bonding distance to Zn at 2.680 Å, yet this group is directed toward the Zn(II) center, likely due to electrostatic forces. For comparison the Zn-Npy distances in **A** are 2.076(3) Å and 2.078(2) Å[21] while those for **B** and **C** are 2.061(4) Å, 2.067(4) Å and 2.092(17) Å, respectively.[16]

Similar to the preparation of **3.1**, the room temperature reaction of a toluene suspension of $ZnBr_2$ with the potentially bidentate species N-(diphenylphosphino)-2-methylaminopyridine produced $[Zn(2\text{-}\{Ph_2PNMe\}(NC_5H_3)Br_2]$ (**3.2**) as a colourless precipitate (**Scheme 3.3**). Single crystals were grown by slow diffusion of hexane into a concentrated solution of the complex **3.2** in dichloromethane. The ^1H and ^{13}C NMR spectra gave resonances and intensities consistent with a single environment for the ligand. Evidence for coordination of the PPh_2 group was given by the ^{31}P NMR resonance at δ 27.7ppm, an upfield shift from the free ligand at δ 51.0ppm. The crystals were of sufficient quality to carry out a single crystal X-ray analysis and the collection details are provided in **Table 3.8**.

Scheme 3.3 Synthesis of **3.2**

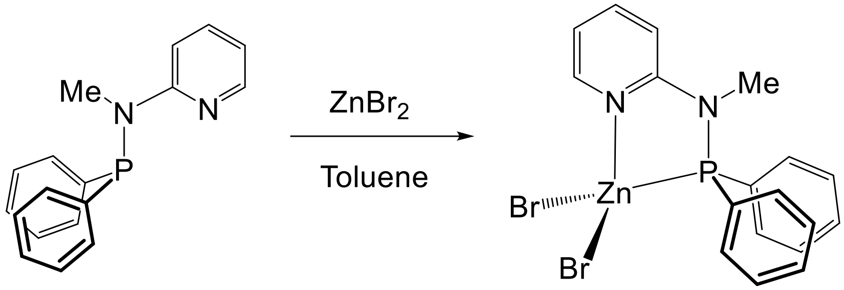

3.2

Complex **3.2** crystallized with two molecules of formula $[Zn(2\text{-}\{Ph_2PNMe\}(NC_5H_3)Br_2]$ in the asymmetric unit and the two displayed very similar bonding parameters with selected metrical values provided in **Table 3.9**. One of these molecules is displayed in **Figure 3.2**, which confirms that complex **3.2** possessed a four coordinate Zn(II) center bonded in a bidentate fashion by the diphenylaminopyridine ("PN") ligand and two bromide anions originating from the starting material. Overall, this yields distorted tetrahedral Zn(II) centers. The PN ligand forms an essentially planar five-membered chelate ring, consisting of the P-N-C-N ligand skeleton bonded to the Zn center with the ligand plane bisecting the Br-Zn-Br plane. The asymmetric unit gave Zn-N distances of 2.067(4) Å and 2.091(4) Å (average = 2.08 Å) and Zn-P distances of 2.4030(13) Å and 2.4045(13) Å) (average = 2.40 Å). These distances are comparable to reported bond distances. The Zn-Br distances are nearly identical and displayed average values of 2.34 Å, again comparable to reported values. While the six angles around each Zn center in **3.2** ranged from 80.53(11)° to 124.86(4)°, the averages of all of these approach an ideal tetrahedral angle with values of 108.3° and 108.4°, respectively. The limitation of the bite angle in the PN ligand led to the smallest angle in the five-membered ring being the P-Zn-N angle.

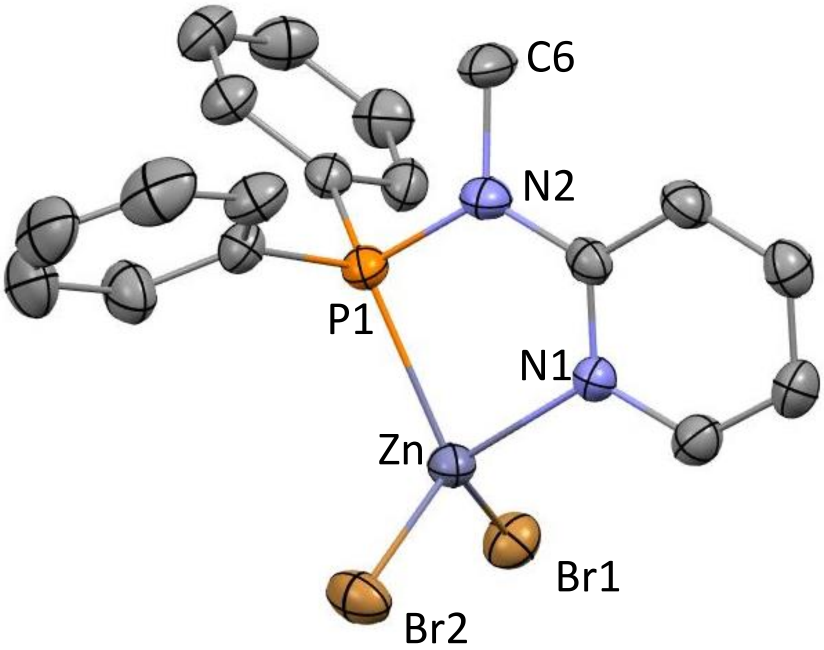

Figure 3.2 Structural representation for the compound **[Zn(2-{Ph_2PNMe}(NC_5H_3)Br_2]** (**3.2**) obtained from single crystal X-ray analysis. Only one of the two molecules in the asymmetric unit is shown. Hydrogen atoms bonded are omitted for clarity.

In order to examine the generality of these complexes and to compare the effects of remote changes to the PN^3P and PN ligands, we prepared the analogous ligands, 2,6-{Ph_2PNH}$_2$(NC_5H_3) and {Ph_2PNH}(NC_5H_3) that differ by replacing the N-Me group with an N-H substituent. These two ligands were employed in an analogous set of reactions with $ZnBr_2$ to produce complexes [Zn(2,6-{Ph_2PNH}$_2$(NC_5H_3)Br_2] **3.3** and [Zn(2-{Ph_2PNH}(NC_5H_3)Br_2] **3.4** related to **3.1** and **3.2** as shown in **Scheme 3.4**.

Scheme 3.4 Synthesis of **3.3** and **3.4**

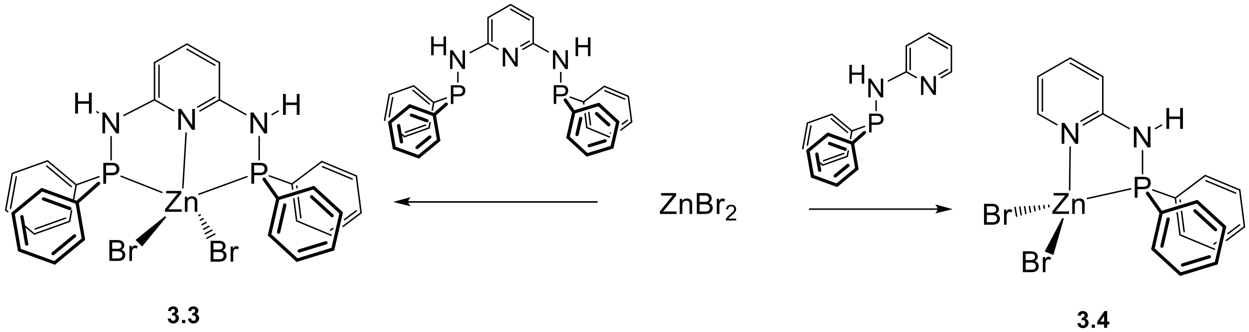

The ^{1}H NMR spectrum of compound **3.3** was similar to that of **3.1** with the expected absence of the N-Me resonance. Furthermore, the ^{31}P NMR spectrum of **3** displayed a single resonance at 22.6 ppm that was of similar shift to **3.1** at 22.5ppm.

We were fortunate to obtain a single crystal of **3.3** and to successfully carry out an X-ray structure analysis. The asymmetric unit was two molecules of formula [Zn(2,6-{Ph_2PNH}$_2$(NC_5H_3)Br_2] each showing a five coordinate Zn(II) constituted from a tridentate PN^{3}P ligand and two bromo ligands as shown in **Figures 3.3** and **3.4**. It appeared that changing the substituent on the amine linking site changed the coordination behavior of the ligand. Selected bonding parameters are given in **Table 3.11**. In the case of **3.3**, the average Zn-P distances 2.4461 Å are similar to those observed in **3.1**, however, for this complex the Zn-N distances of 2.472(4) Å and 2.525(4) Å are shorter than that in **3.1** (2.680 Å). It is important to note that these distances are longer by about 0.5 Å compared to the Zn-Npyridyl distances in **3.2** or **3.4** (see below). The interaction of Npy base site with the Zn does lead to some effects on the coordination geometry, which include an increase in P-Zn-P (132.11(5)° and 126.20(5)°) versus 113.76(9)° in **3.1** and differentiates the two Zn-Br with Br(1) oriented "trans" to the Npy and Br(2) at 90 degrees to Br(1) and the Npy center. This gives a kind of distorted pyramidal coordination geometry; however, it should be noted that taking out the angles involving N gave an average for the bonding angles around Zn in the two molecules of 109.3 and 109.4, which resemble a pseudo-tetrahedral Zn coordination geometry.

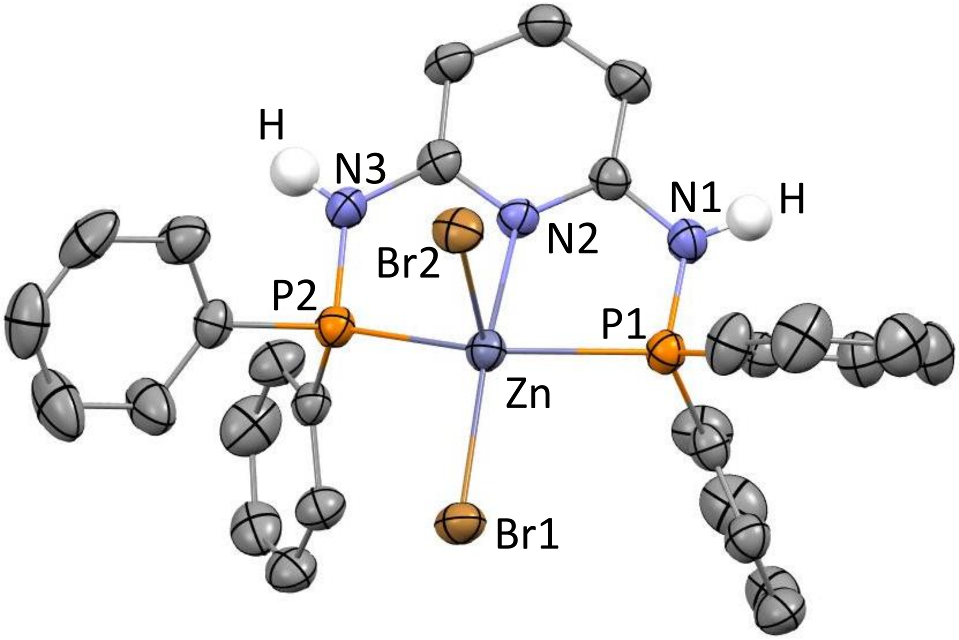

Figure 3.3 Structural representation for one of the two unique molecules of the compound **[Zn(2,6-{Ph_2PNH}$_2$(NC_5H_3)Br_2] (3.3)** in the asymmetric unit. The hydrogen atoms bonded to carbon as well as co-crystallized solvent are omitted for clarity

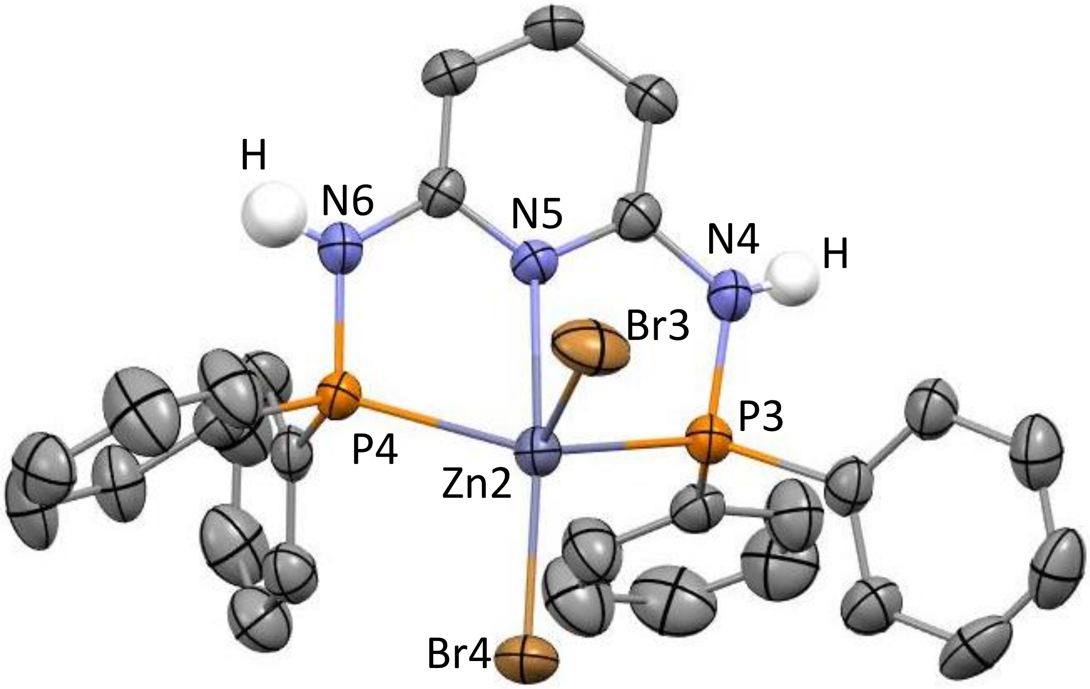

Figure 3.4 Structural representation for one of the two unique molecules of the compound **[Zn(2,6-{Ph_2PNH}$_2$(NC_5H_3)Br_2] (3.3)** in the asymmetric unit. The hydrogen atoms bonded to carbon as well as co-crystallized solvent are omitted for clarity.

Similar to the synthesis of **3.2**, combination of $ZnBr_2$ and 2-{Ph_2PNH}(NC_5H_3) gave complex **3.4** as shown in **Scheme 3.4**. Spectroscopic evidence for **3.4** included the appearance of ligand resonances in the ^{1}H NMR and single resonance in the ^{31}P NMR at 22.65ppm, comparable to that of analogue **3.2**.

Single crystals of **3.4** allowed for the confirmation and determination of structural features of complex **3.4** by single crystal X-ray analysis. The results of this analysis are depicted in **Figure 3.5** with selected crystallographic and structural parameters in **Tables 3.10** and **3.12**.

Even a cursory inspection of **Figures 3.2** and **3.5** indicates the clear relationship between complexes [Zn(2-{Ph_2PNMe}NC_5H_3)Br_2] (**3.2**) and [Zn(2-{Ph_2PNH}(NC_5H_3)Br_2] (**3.4**) and the metrical parameters bear out this observation. Specifically, the Zn-Element bond distances in **3.4** are similar to those in **3.2** and the angles around the Zn center in **3.4** parallel those of **3.2** with the smallest angle being the PN ligand bite angle at 82.30(9)°. The average for the six metal centered angles is 108.43° indicative of a distorted tetrahedral Zn coordination environment.

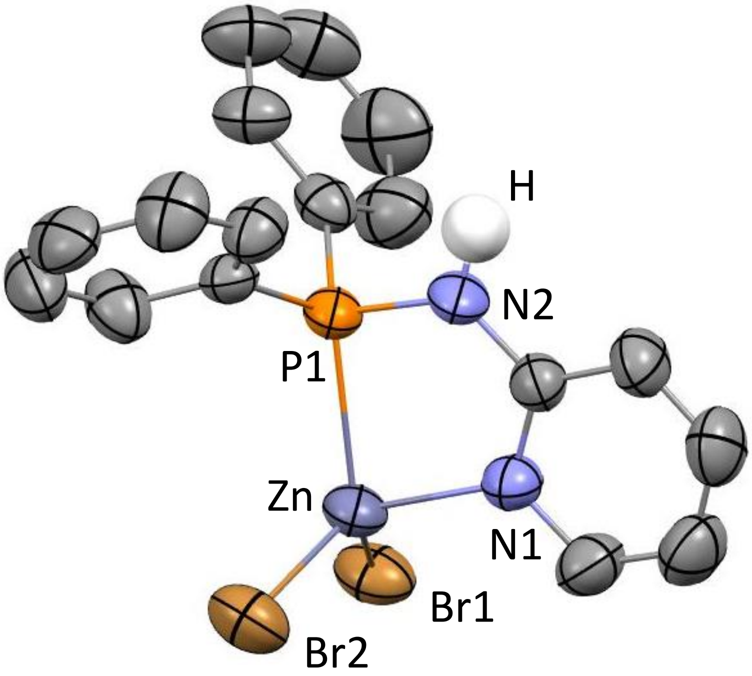

Figure 3.5. Structural representation for the compound **[Zn(2-{Ph_2PNH}(NC_5H_3)Br_2] (3.4)** obtained from X-ray analysis. Hydrogen atoms bonded to carbon are omitted for clarity.

Computations

The differences in the bonding interactions of the PN^{3}P ligand with the Zn(II) center in **3.1** and **3.3** have been noted with the most obvious difference being the interaction of the pyridyl nitrogen with the metal center. The only difference between these two ligands is a change of the substituent, from CH_3 to H, on the amino N center that links the pyridyl and PPh_2 groups. This group is remote from the Zn and is directed away from the coordination sites. It is also noteworthy that the Zn-Npy distances are 0.4-0.6 Å longer in both **3.3** (2.472(4) Å, 2.525(4) Å) and in **3.1** (2.680 Å) compared to the Zn-Npy distances in **3.2** or **3.4** (2.06-2.07 Å). These observations prompted a computational investigation of these complexes through DFT analysis. Starting from the X-ray structure, a DFT optimization using the B3LYP functional and the def2TZVP basis set was performed on complex **3.1** with the results summarized in **Table 3.1** and the optimized structure shown in **Figure 3.6**.

Table 3.1 Comparison of selected internuclear distances (Å) and angles (^{o}) between the experimental (X-ray) and DFT optimized geometries (B3LYP) of compound **3.1**.

Bonds (Å)	X-ray	B3LYP
Zn(1)-Br(2)	2.3868(15)	2.41250
Zn(1)-Br(1)	2.4016(13)	2.41891
Zn(1)-P(1)	2.424(3)	2.52734
Zn(1)-P(2)	2.425(3)	2.52749
Zn-N	2.680	2.88274
Bond angles (^{o})		
Br(2)-Zn(1)-Br(1)	115.50(5)	121.830
P(1)-Zn-P(2)	113.76(9)	113.029

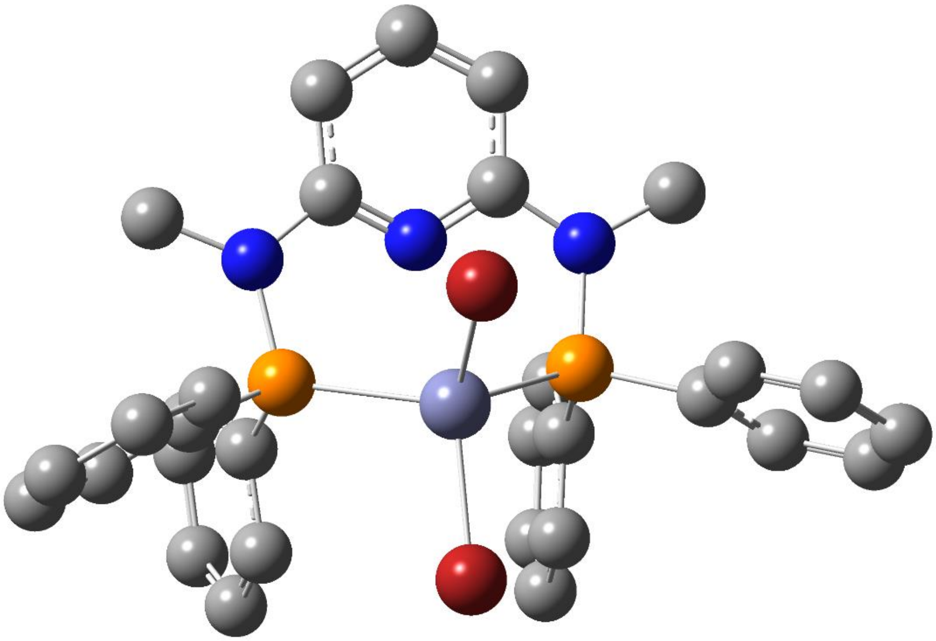

Figure 3.6 Optimized structure of [Zn(2,6-{Ph_2PNMe}$_2$(NC_5H_3)Br_2] **(3.1).** Hydrogen atoms have been omitted for clarity.

Next we targeted the DFT optimization of complex **3.3** using the B3LYP functional and the def2TZVP basis set with the results summarized in **Table 3.2** and the optimized structure shown in **Figure 3.7**. The computationally optimized structure for **3.3** looks, perhaps not surprisingly, quite similar to **3.1**. Specifically, this structure no longer displayed a Zn-N bond and has a new value for this distance of 2.89270 Å. As a result there is a change of P-Zn-P angle from an average value of 129.1° to 116°. These results strongly suggest that the Zn-Npy bonds seen in the X-ray structures may be a result of coulombic interactions and crystal packing features and that both PN^3P analogues favor a tetrahedral geometry with a pendent Npyr.

Table 3.2 Comparison of Selected Internuclear Distances (Å) and angles (°) between the Experimental (X-ray) and DFT Optimized Geometries (B3LYP) of Compound **3.3**.

Bond (Å)	X-ray	B3LYP
Zn-Npy	2.4985	2.89270
Zn-P	2.4461	2.55998
Zn-Br ax	2.4035	2.41117
Zn-Br	2.438	2.41429
Bond angles (°)		
Br-Zn-Br	110.9	121.959
P-Zn-P	129.1	116.134

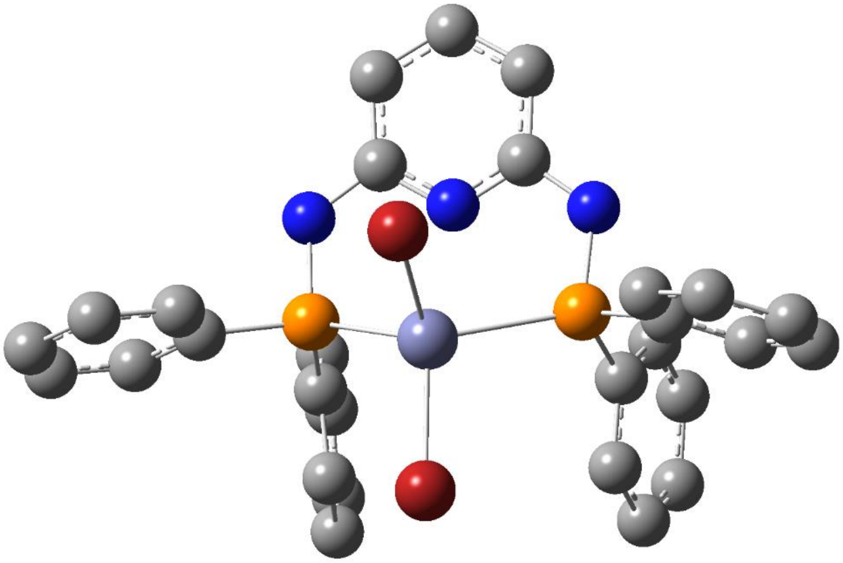

Figure 3.7 Optimized structure of [Zn(2,6-{Ph_2PNH}$_2$(NC_5H_3)Br_2] **(3.3).** Hydrogen atoms have been omitted for clarity.

Electrochemistry and Electrocatalysis

The structural features of complexes **3.1** and **3.2**, bear some resemblance to the catalytic Zn complexes **A**, **B**, **C** and **E** that have demonstrated chemical and electrochemical catalysis for CO_2 reduction and H_2 formation. Having a pendent base site on the Zn complex has been invoked as important in this reactivity and may play a role by functioning with the Zn(II) center as a "frustrated Lewis pair". With this in mind an exploration of the electrochemical and electrocatalytic ability of these Zn complexes was initiated.

We began by performing cyclic voltammetric (CV) measurements on complex **3.1** [Zn(2,6-$\{Ph_2PNMe\}_2(NC_5H_3)Br_2$]. The CV for 1.0 mM acetonitrile solution of **3.1** was performed under N_2 with 100 mM tetrabutylammoniumhexafluorophosphate (TBAHFP) supporting electrolyte using a glassy carbon (GC) working electrode, a Pt counter electrode and a pseudo-reference electrode Ag wire, referenced to the ferrocene/ferrocenium (Fc/Fc^+) couple, with the results shown in **Figure 3.8**. The cathodic scan for complex **3.1** revealed two irreversible reduction peaks at -2.46 and -2.69 V vs. Fc/Fc^+. We also carried out a series of CV measurements on this sample with scan ranges varying from 0.1 – 1.2 V/s and these are shown in **Figure 3.9**. Plotting the current intensity versus square root of scan rate dependence of the reduction peak, these scans show a linear dependence (**Figure 3.10**) on the current associated with the reduction at
-2.42V which is an indication of a freely diffusing species.[22]

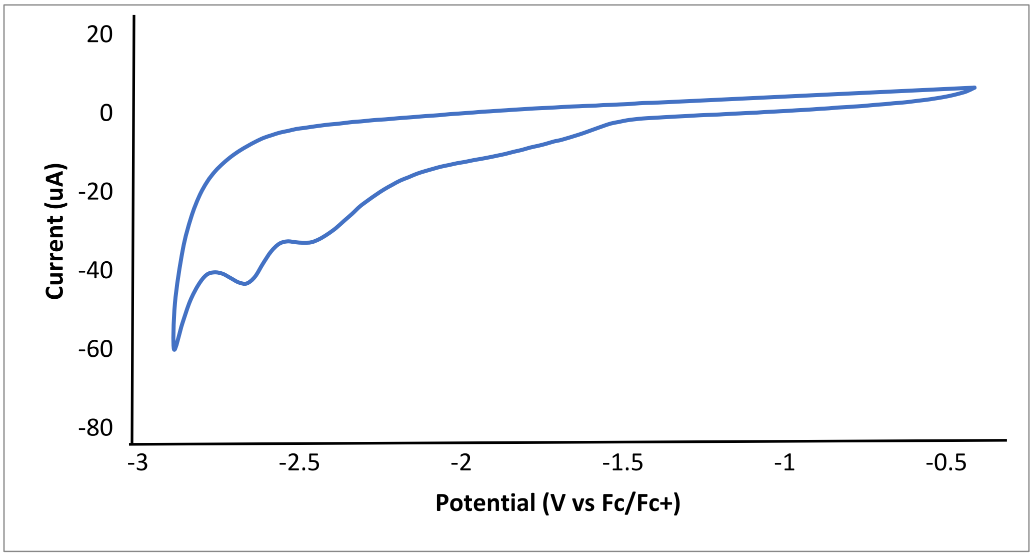

Figure 3.8 Cyclic voltammogram of complex [Zn(2,6-{Ph_2PNMe}$_2$(NC_5H_3)Br_2] **(3.1)** (1mM) in presence of 100mM TBAHFP in CH_3CN using a glassy carbon (GC) working electrode.

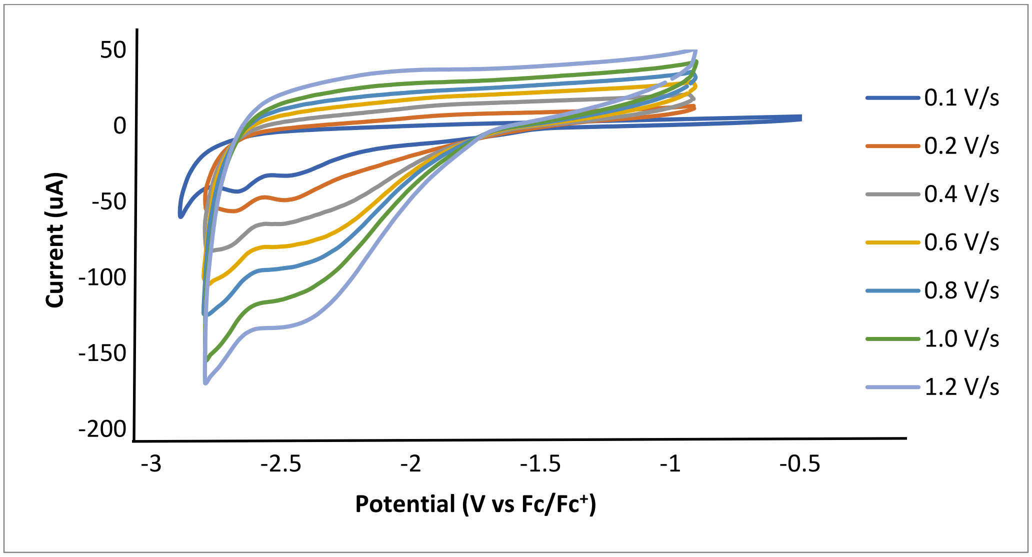

Figure 3.9 Cyclic voltammograms for [Zn(2,6-{Ph_2PNMe}$_2$(NC_5H_3)Br_2] **(3.1)** with different scan rates.

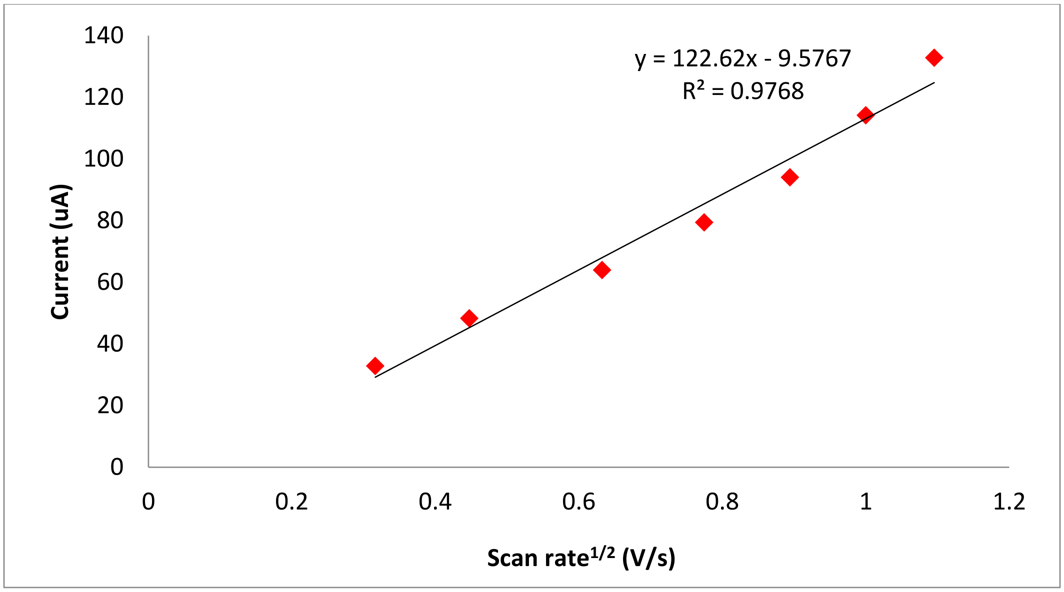

Figure 3.10 Plot of scan rate$^{1/2}$ versus current for the reduction peak at -2.42 *vs.* Fc/Fc$^+$ of [Zn(2,6-{Ph_2PNMe}$_2$(NC_5H_3)Br_2] **(3.1)** in CH_3CN.

We next examined the effect of added water on the electrochemical behavior of **3.1** to inspect the ability of using water as proton (H^+) source as well as for hydrogen (H_2) production. **Figure 3.11** shows the cathodic scans for CH_3CN solutions (10 mL) of **3.1**,using a GC electrode and referenced to Fc$^+$/Fc, for the pure solutions and addition of 100 to 700 microliters of water. With 100 μL of added water there is current enhancement at about -2.5V that continues to increase at more negative potentials. Addition of 200 and 300 μL of water caused further and continued current enhancement. Again, these are signs of catalytic water reduction. Interestingly, when 500 μL of water was added the current enhancement returned to values similar to those observed for 200μL and less than 300μL of added water. At 700μL of added water there was essentially no change from those of 500μL. These observations are shown in **Figure 3.12**, which presents a plot of current *vs.* added water for the cathodic scan of **3.1**. It appears that complex **3.1** is able to catalytically reduce water and that there is a limit to this behavior.

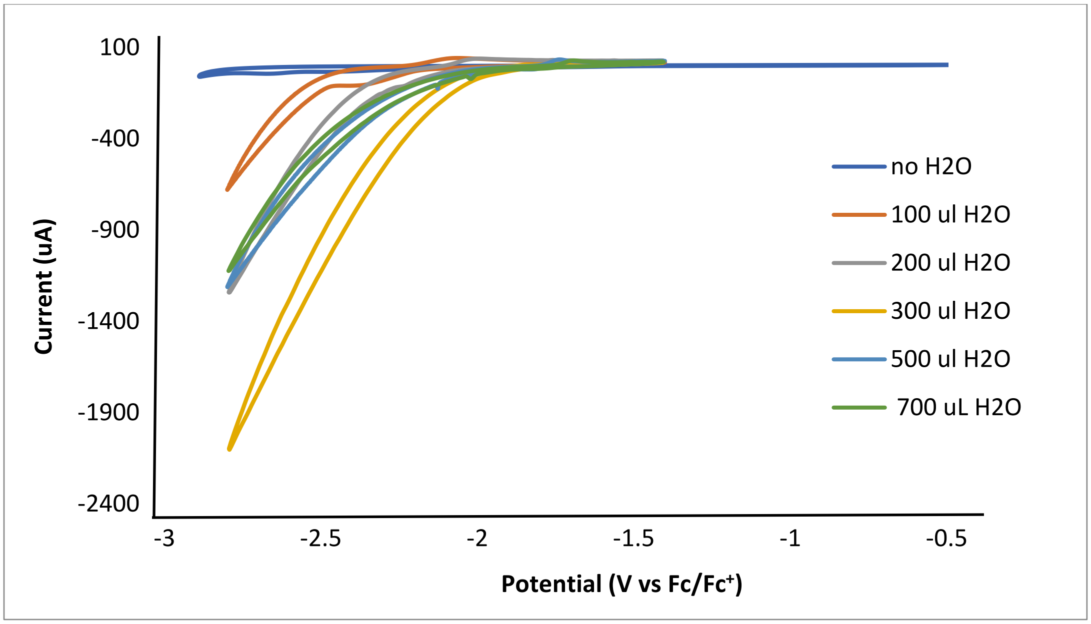

Figure 3.11 The effect of added water on the cathodic/reduction behavior of complex **3.1**. Each scan was carried out under N_2 with 1mM **3.1** in CH_3CN with a GC working electrode, Pt counter electrode and Ag wire pseudo-reference electrode. All scan potentials were adjusted to Fc^+/Fc reference potential. Scans corresponding the various amounts of added water are color coded as shown in the figure legend.

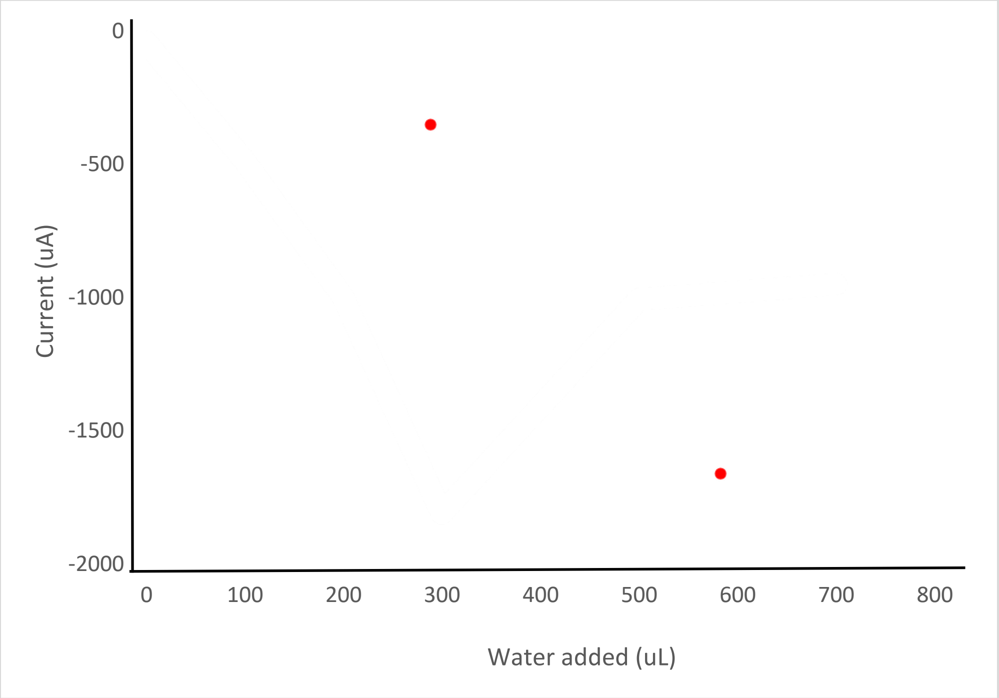

Figure 3.12. A graph of the effect of added water on the current at -2.7 V (vs. Fc^+/Fc) for complex **3.1**. Data was obtained from the experiments shown in **Figure 3.11**.

We next examined the reduction ability of complex **3.1** in the presence of water when the nitrogen atmosphere was exchanged for CO_2. As shown in **Figure 3.13**, there was an additional increase in current when acetonitrile solutions of **3.1** were reduced in the presence of CO_2 and H_2O. These observations are consistent with possible electrocatalytic CO_2 reduction by **3.1**.

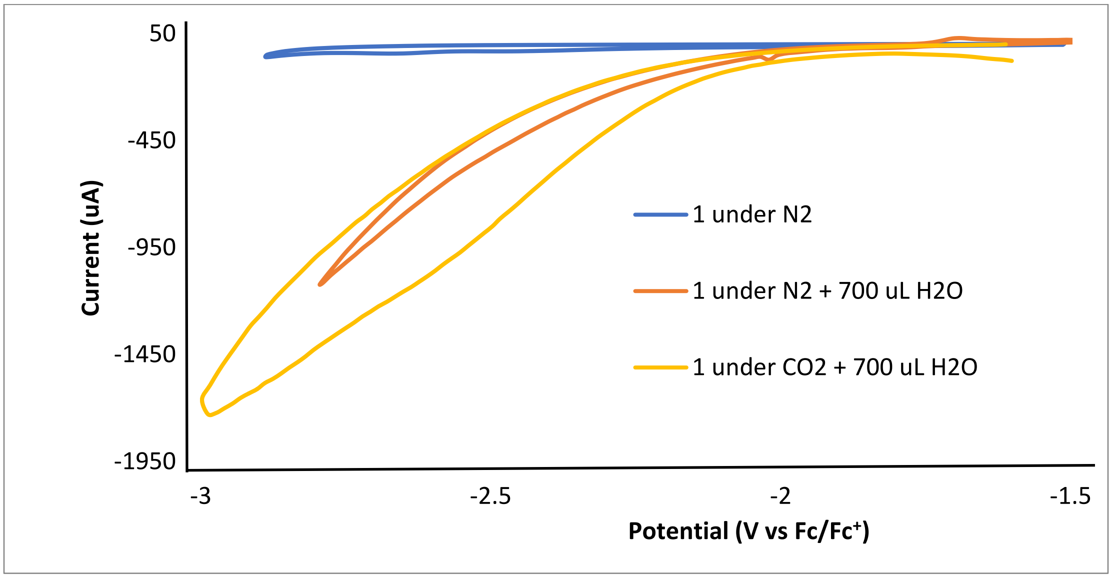

Figure 3.13. Cathodic CV measurements of complex [Zn(2,6-{Ph_2PNMe}$_2$(NC_5H_3)Br_2] **(3.1)** in CH_3CN with a GC electrode under N_2 (blue), under N_2 with 700µL of added water (red), and under a CO_2 atmosphere with 700µL of added water (orange). All potentials are referenced to Fc^+/Fc.

A similar set of cyclic voltammetry measurements were carried out on complex **3.2**, [Zn(2-{Ph_2PNMe}NC_5H_3)Br_2] and are shown in **Figures 3.14-3.20**. Like complex **3.1**, the CV for complex **3.2** in CH_3CN with a glassy carbon working electrode, Pt counter electrode and Ag wire pseudo-reference electrode showed two irreversible reductions at –2.33V and -2.73V versus Fc/Fc^+. An overlay of the CV's emphasizing the relationship of **3.1** and **3.2** is presented in **Figure 3.15**.

We also attempted to measure the scan rate dependence of the reductions of **3.2**. As seen in **Figure 3.16**, as the scan rate was increased, the increase in current and the shift of the first reduction to a more negative values made it difficult to obtain clear current/voltage numbers. Using the second reduction potential -2.73V, a plot was made for the current versus the square root of the scan rate that produce a linear relationship given in **Figure 3.17**.

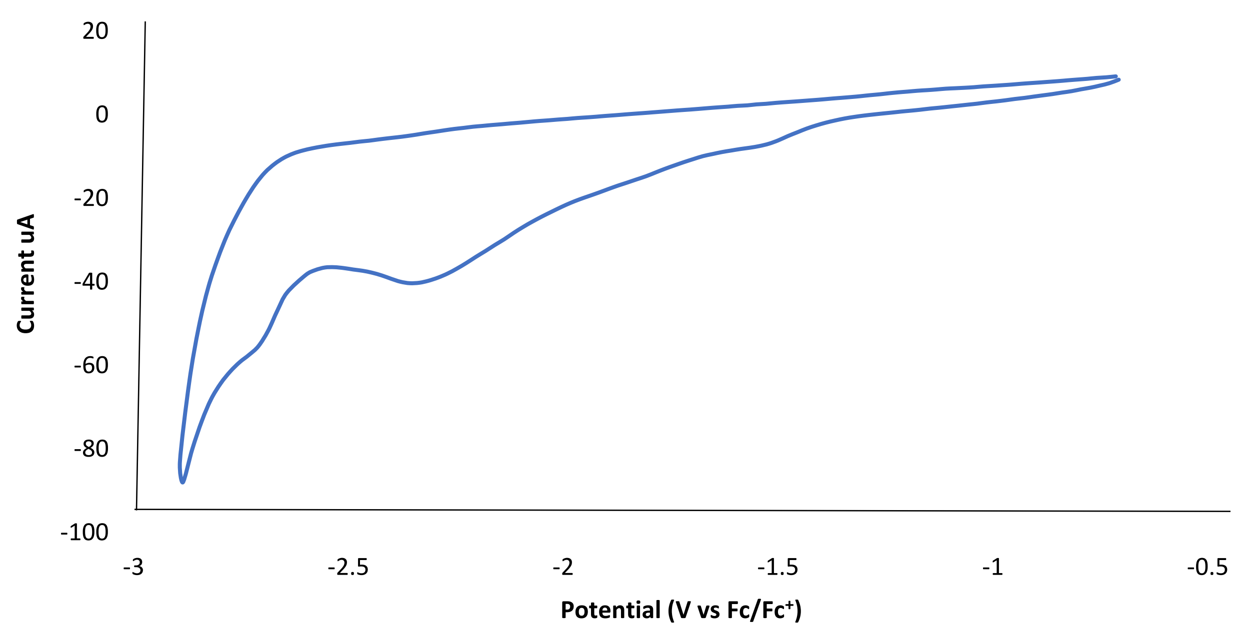

Figure 3.14 Cyclic voltammogram of [Zn(2-{Ph_2PNMe}(NC_5H_3)Br_2], complex **3.2**, 1mM in CH_3CN with 100mM TBAHFP using a glassy carbon (GC) working electrode.

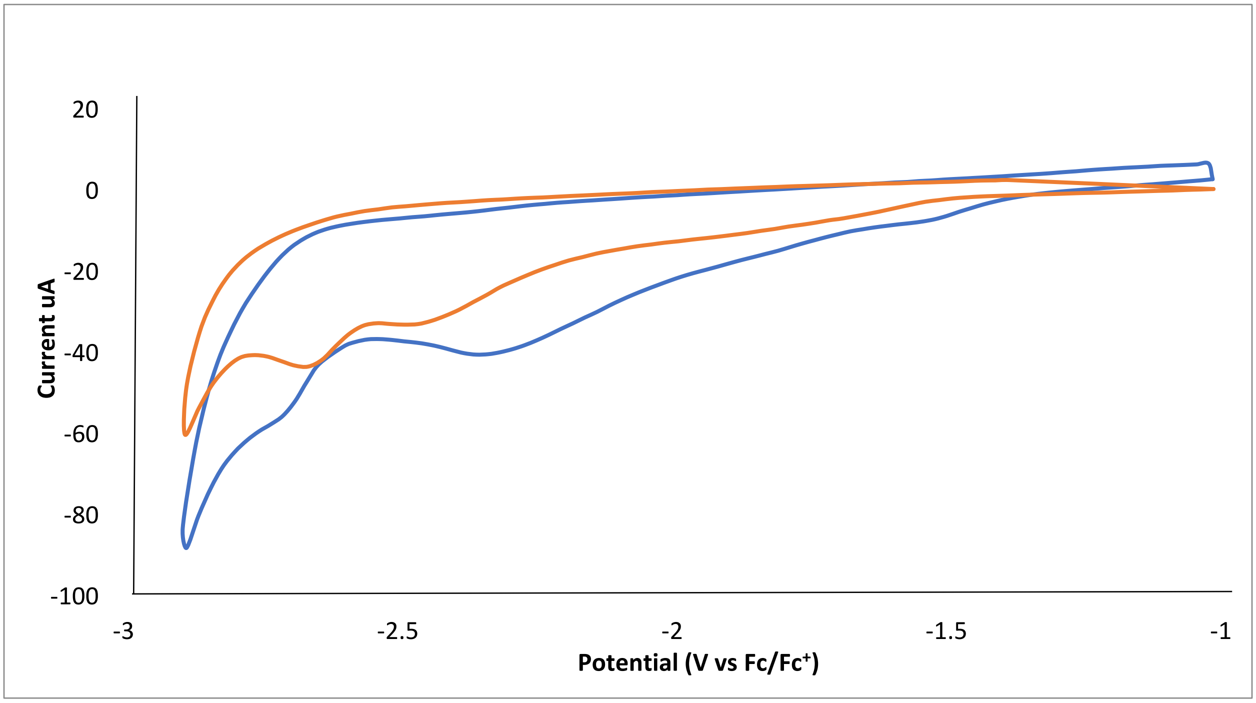

Figure 3.15 Overlay of the CV's of complexes [Zn(2,6-{Ph_2PNMe}$_2$(NC_5H_3)Br_2] **(3.1)** orange and [Zn(2-{Ph_2PNMe}(NC_5H_3)Br_2] **(3.2)** blue.

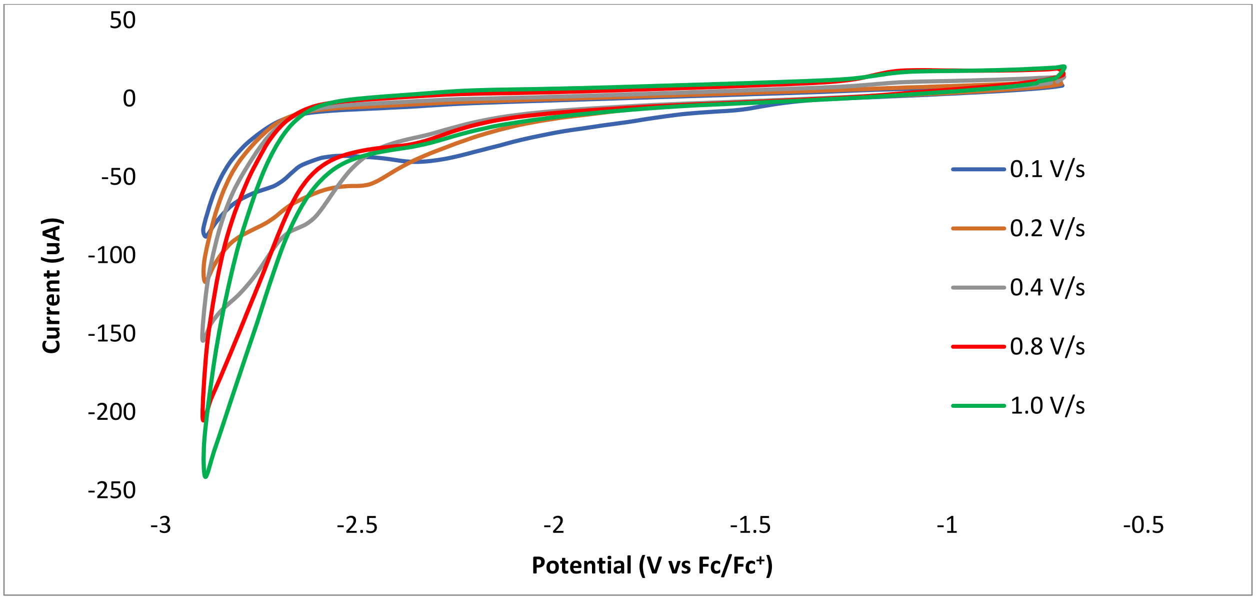

Figure 3.16 Cyclic voltammograms for [Zn(2-{Ph_2PNMe}(NC_5H_3)Br_2] **(3.2)** in presence of 0.1 M TBAHFP in CH_3CN using a glassy carbon (GC) working electrode with different scan rate.

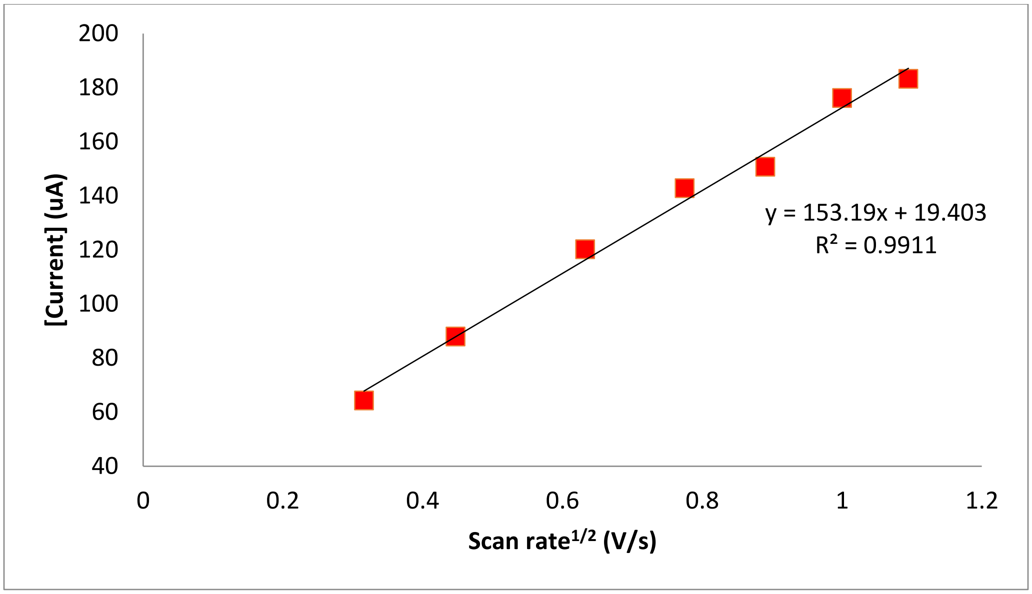

Figure 3.17 Plot of scan rate$^{1/2}$ versus current for the reduction peak of [Zn(2-{Ph_2PNMe}(NC_5H_3)Br_2] **(3.2)** at -2.74 V vs Fc/Fc$^+$ in CH_3CN.

The effect of adding water on the electrochemical behavior of **3.2** was measured by adding aliquots of water to acetonitrile solutions of **3.2** and the results are summarized in **Figure 3.18**. As was observed with **3.1**, substantial current enhancement was observed when water was added to solutions of **3.2** beginning at about -2.4V vs Fc$^+$/Fc. As the potential was scanned to more negative values, this current enhancement increased. This observation is suggestive of electrocatalytic water reduction by **3.2**. However, in contrast to **3.1** there seemed to be little effect of changing the water aliquot from 300µL to 700µL. This is more generally/clearly shown in **Figure 3.19**, where the current intensity showed little variation from 100-700µL of added water.

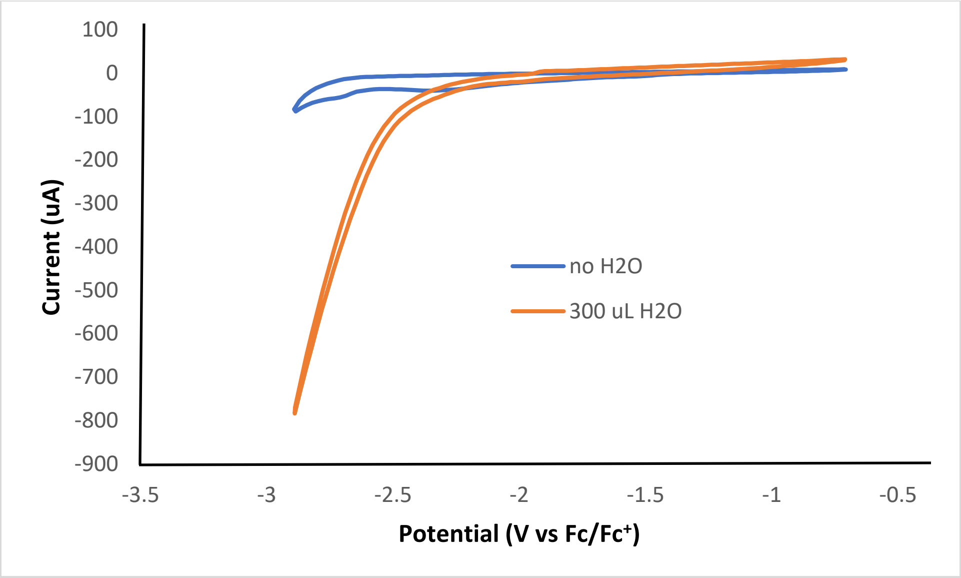

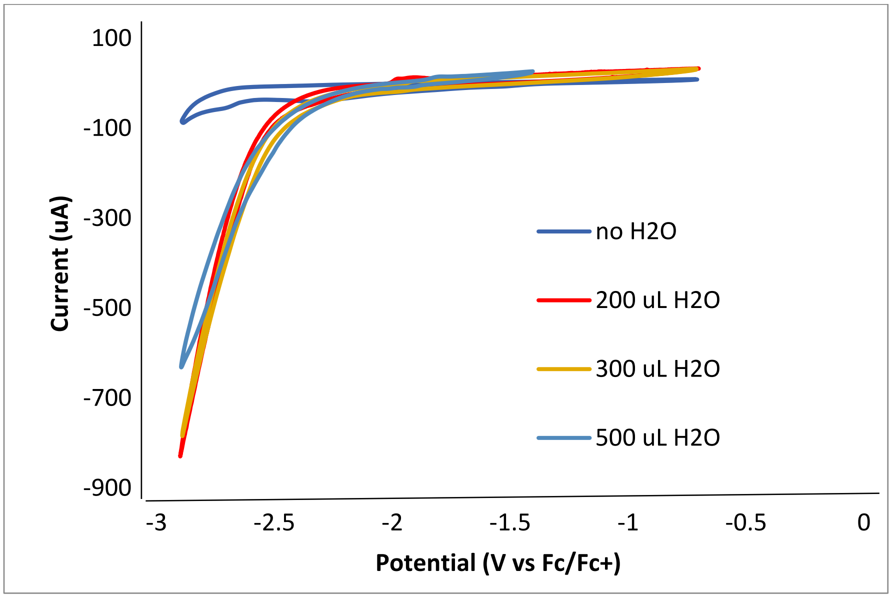

Figure 3.18 The effect of added water on the cathodic/reduction behavior of complex **3.12**. Each scan was carried out under N_2 with 1mM **1** in CH_3CN with a GC working electrode, Pt counter electrode and Ag wire pseudo-reference electrode. All scan potentials were adjusted to Fc^+/Fc reference potential. Scans corresponding the various amounts of added water are color coded as shown in the figure legend.

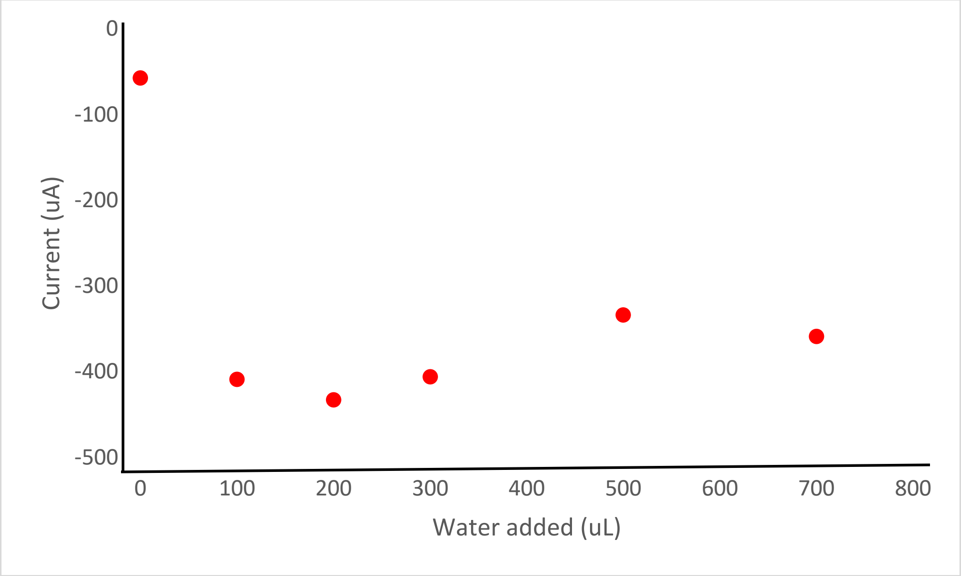

Figure 3.19 A graph of the effect of added water from 100µL to 700µL on the current at -2.73 V (vs. Fc$^+$/Fc) for complex **3.2**.

The effect of changing the atmosphere from nitrogen to carbon dioxide was explored next. **Figure 3.20** shows a CV at negative potentials versus Fc$^+$/Fc of complex **3.2**, under similar conditions as shown in **Figure 3.13**. Included in this Figure are cathodic scans of **3.2** with addition of 700 µL and of **3.2** with 700 µl of added water under a CO_2 atmosphere. The replacement of the reaction atmosphere with CO_2 did not appear to lead to any further current enhancement.

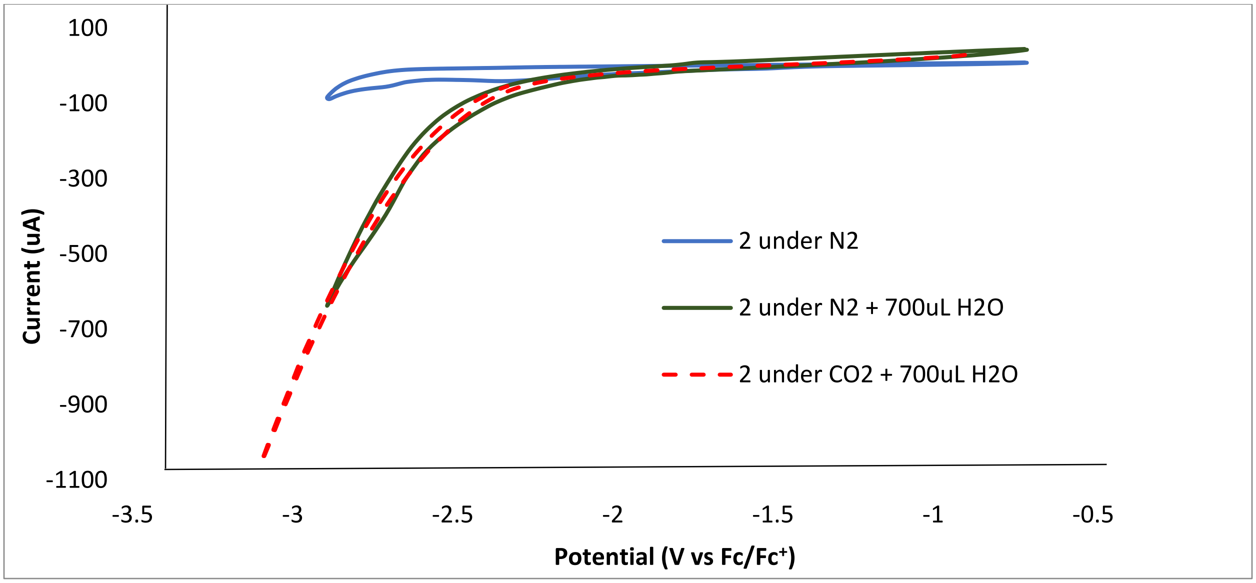

Figure 3.20 Cathodic CV measurements of complex **3.2** in CH_3CN with a GC electrode under N_2 (blue), under N_2 with 700µL of added water (green), and under a CO_2 atmosphere with 700µL of added water (red). All potentials are referenced to Fc^+/Fc.

The preceding experiments demonstrated significant current enhancement of the reduction of complexes **3.1** and **3.2** in the presence of H_2O and CO_2. These are clear indications of electrocatalytic reductions of water and possibly CO_2. In order to more definitively establish the catalytic behavior of complexes **3.1** and **3.2**, the products of these reactions were analyzed after controlled potential coulometry (CPC). The reaction headspace was examined by GC for evidence of CO and H_2 and solution NMR analysis was employed to probe the formation of condensed phase products such as formic acid. The results of these investigations are presented in **Tables 3.3** and **3.4**.

Table 3.3 Controlled potential coulometry of 1mM Catalyst [Zn(2,6-{Ph_2PNMe}$_2$(NC_5H_3)Br_2] (**3.1**) in 15mL of acetonitrile under CO_2 atmosphere.

Exp.	**Potential (V) vs Fc^+/Fc**	**Time (hrs)**	**Added H_2O (μL)**	**H_2 (μmol)**	**CO (μmol)**	**HCOOH (μmol)**	**FE (%)**
1	-2.3	5	200	4.9	14.2	0	-
2	-2.3	18	200	169.43	55.47	52.95	32.6%
3	-2.3	5	500	29.7	49	13.5	64.7%
4	-2.3	11	500	37.87	80.92	21.75	51.1%
5	-2.3	18	500	282	22.26	132.3	24.4%
6	-2.7	5 hrs	200	5.26	24.73	0	-
7	-2.7	5 hrs	500	87.15	143.1	44.8	42.8%
8*	-2.3	5 hrs	200	2.3	0	0	-

** no catalyst was added in this experiment.*

In the case of complex **3.1**, coulometry measurements were carried out at -2.3V and -2.7V vs. Fc^+/Fc under a CO_2 atmosphere with either 200μL or 500μL of added water. These measurements documented the formation of H_2 and CO as the only observed gas phase products and formate/formic acid in solution, Measurements carried out at -2.3V indicated that increasing the amount of added water led to increased formation of H_2 and HCOOH. Generally, there was also an increase in formation of CO when water was increased. However, experiment 5 gave an anomalously low yield of CO while the amounts of produced H_2 and HCOOH remained elevated. The origin of this exception is still under investigation. As a control experiment, the conditions of experiment 1 were duplicated in the absence of catalyst **3.1** giving the results shown as experiment

8 in **Table 3.3** and documenting a small background generation of H_2 and no CO_2 reduction thus detailing the required presence of complex **3.1** for these reduction reactions.

Similar reduction experiments with complex **3.1** were carried out at a more reducing potential of -2.7 V vs Fc^+/Fc and are shown in **Table 3.3** as experiments 6 and 7. These results show a substantial increase in H_2,CO and HCOOH reduction products.

A parallel set of reactions were carried out to explore the products form the reduction reactions with the "PN" ligand supported Zn complex [Zn(2-{Ph_2PNMe}(NC_5H_3)Br_2] **(3.2).** Initial results of controlled potential coulometry of **3.2** in acetonitrile with added water and under a CO_2 atmosphere are shown in **Table 3.4**. At -2.3V *vs* Fc^+/Fc, under experimental conditions similar to experiment 1 in **Table 3.3**, H_2 was the only observed product. This is perhaps not too surprising given the voltametric behavior of **3.2** shown in **Figure 3.20** in which water and water/CO_2 showed similar current enhancements. Using a stronger reduction potential of -2.6 V gave the expected increase in H_2 production as well as a small formation of CO, thus showing that complex **3.2** has some electrocatalytic CO_2 reduction ability. Interestingly, an increase in the amount of added water at -2.6V gave a substantial increase in yield of CO.

Table 3.4 Controlled potential coulometry of 1mM Catalyst [Zn(2-{Ph_2PNMe}(NC_5H_3)Br_2] **3.2** in 15mL of acetonitrile with added water under CO_2 atmosphere.

Potential (V) vs Fc^+/Fc	**Time (hrs)**	**H_2O (μL)**	**H_2 (μmol)**	**CO (μmol)**
-2.3	5	200	3.39	0
-2.6	5	200	22.5	6.6
-2.6	5	500	18.7	27.7

In summary, these CPC experiments provide strong evidence of the ability of the Zn(II) complexes **3.1** and **3.2** to electroreduce both water, to give H_2, and CO_2, to give CO and formic acid, although

3.1 has shown to be the more effective catalysts exhibiting CO_2 reduction at a lower potential, possibly due to its unique pendant basic site (the pyridine N) as seen when comparing **Table 3.3** to **3.4**.

Proposed Mechanism

As outlined in the introduction to this chapter, there remain a rather limited number of reports on homogeneous Zn complexes as either CO_2 or proton reduction catalysts. Although formation of H_2, CO or formate from Zn complexes has been reported, we observe a unique distribution of these products with complex **3.1**, the formation of formate via electrochemical reduction, and the formation of hydrogen from neutral water. In order to provide a clear context for our observed electroreduction products, it is prudent to briefly review the reaction details for the electrocatalysis of complexes **A**-**E**. Two of these species, **D** and **B**, were reported to electrocatalytically yield CO. Complexes **A** and **E** are catalysts for hydrogen generation employing either methanolysis of triphenylsilane or electrocatalytic reduction of acetic acid, respectively. Furthermore, both **A** and **E** have been used for CO_2 to formate transformation.

The Zn porphyrin complex **D** was not used as a homogeneous catalyst but was actually heterogenized by support on a carbon fiber and used for electrocatalytic reduction to produce hydrogen at "less than" -2.04V vs. $Fc^{+/0}$ with CO appearing at more negative potentials and maximizing at -2.34V vs. $Fc^{+/0}$.[15] These researchers argue that the reactivity does not directly involve the Zn(II) center but rather the noninnocent redox-active ligand provides the reducing equivalents for catalysis. Complex **B** is the other reported Zn complex that converted CO_2 to CO.[16] The suggested mechanism followed a more conventional proton coupled electron transfer to yield CO and H_2O although no quantitation of either CO or water was reported. Importantly, the mechanism employed the non-coordinated phosphorus center to activate the CO_2 but there were no further details on subsequent reaction steps.

Using acetic acid as a hydrogen source, Zn complex **E** exhibited catalytic H_2 evolution at -1.7 V vs $Fc^{+/0}$.[23] The mechanism for this reaction was proposed to be a ligand-centered radical coupling. Support for this came from the observation that ligand alone demonstrated enhanced catalytic current (-2.1V) and through DFT computations. The authors suggested that the role of Zn(II) was to provide a structural framework for the H_2 formation.

The reduction of CO_2 to formate species was seen with complexes **A** and **E**. In the case of **A**, this reaction is a catalytic hydrosilylation reaction involving addition of triethoxysilane to CO_2 and generating triethoxysilylfomate and is based on the insertion of CO_2 into the Zn-H function.[14] In the case of complex **E**, formate was produced from the reduction of a methyl carbonate species Zn-OC(O)OMe.[17] The methyl carbonate arose from the insertion of CO_2 into a Zn-OMe group. Successful reduction to formate was by chemical or electrochemical means. The most pertinent method for comparison with our results is the observation that **E,** Zn(DMTH), was capable of electrocatalytic reduction of CO_2 to formate but only when a particular reaction order was followed. First MeOH is added to the complex to yield the protonated ligand/methoxide species $Zn(HDMTH)(OCH_3)$, which was then reacted with CO_2 to yield the methyl carbonate complex $Zn(HDMTH)(CO_3CH_3)$. Only after this formation could addition of acetic acid and electrolysis at −2.37 V produce a mixture of H_2 and formate. In this case it is the electrochemical generation of hydrogen that is responsible for the reduction of the methyl carbonate and the authors suggest that it is the reduction of $Zn(H_2DMTH)(CO_3CH_3)$ with a double protonation of the DMTH ligand, which is the hydride source.

Given this context, the ability of complex **3.1** to undergo electrocatalytic reduction of water and CO_2 is unique as is the appearance of both CO and formate as reduction products. Examining more closely the reduction of water to make H_2, **Table 3.5** compares the electrocatalytic reduction of water in an acetonitrile solution of complex **3.1** under nitrogen atmosphere compared to this reaction under a CO_2 atmosphere. The first notable feature is that complex **3.1** reduces neutral water to produce H_2 at -2.2 V making it superior to **E**, which required acetic acid a much more active hydrogen source. It is also interesting that H_2 formation is faster under a N_2 atmosphere compared to the same process under CO_2. It appears that there is a competition between CO_2 and water reduction.

Table 3.5 Controlled potential coulometry of 1mM Catalyst **3.1** in 15mL of acetonitrile with added water under a CO_2 or a N_2 atmosphere.

Potential (V) vs Fc^+/Fc	**Time (hrs)**	**Reaction atmosphere**	**H_2O (µL)**	**H_2 µmol**	**CO µmol**
-2.2	4	CO_2	200	9.2	9.3
-2.2	4	N_2	200	26.1	0

In order to more clearly understand the electronic distribution in the reduction of **3.1** a DFT optimization of the anion $[Zn(2,6\text{-}\{Ph_2PNMe\}_2(NC_5H_3)Br_2]^-$ **(3.1^-)** was performed. Beginning with the optimized structure of complex **3.1** an electron was added and a new DFT optimization was performed with the B3LYP functional and def2TZVP basis set. The goal was to interrogate where the electron would reside on compound **3.1** after reduction.

Table 3.6 Comparison of Selected Internuclear Distances (Å) between the Experimental (X-ray) and DFT Optimized Geometries of Compounds **3.1**.

	X-ray	B3LYP	Anion B3LYP
Zn(1)-Br(2)	2.3868(15)	2.41250	2.44922
Zn(1)-Br(1)	2.4016(13)	2.41891	2.47159
Zn(1)-P(1)	2.424(3)	2.52734	2.51825
Zn(1)-P(2)	2.425(3)	2.52749	2.51825
Zn-N	2.680	2.88274	2.77531
Br(2)-Zn(1)-Br(1)	115.50(5)	121.830	116.996
P(1)-Zn-P(2)	113.76(9)	113.029	118.887

When computing the anion of complex **3.1** with B3LYP, the SOMO is shown in **Figure 3.21**. Essentially a lone electron on Zn that resides in a s type orbital (99.35%).

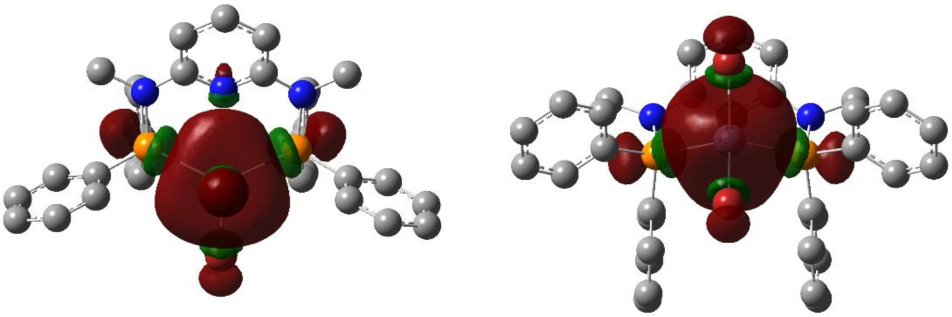

Figure 3.21 Two views of the SOMO of the anion [Zn(2,6-{Ph_2PNMe}$_2$(NC_5H_3)Br_2]$^-$ **(3.1$^-$)**.

In **Scheme 3.5** a proposed mechanism for the catalytic reduction of CO_2 can be seen for **3.1**, noting that it may enter two different pathways depending on the product, CO or fomate. This is based on the computations, such as the reduction to yield the anion, bulk electrolysis results as well as literature hypotheses. Initially, **3.1** undergoes a reaction with water and further reduction to produce a Zn-H and eliminate a bromide anion. The Zn-H has two paths with the first being release of hydrogen by reaction with water. The second is the insertion of CO_2 to generate a formate complex that could release formate by substitution with, for example, bromide.

The path to CO formation employs a proton coupled electron transfer to release H_2O and CO. The reaction of Lewis acid CO_2 with pendant base pyridine to activate the CO_2. Protonation and electrochemical reduction would produce a metallaformic acid susceptible to loss of water and release of CO.

Scheme 3.5 Proposed mechanism for **3.1** CO_2 reduction pathways to yield CO and formate.

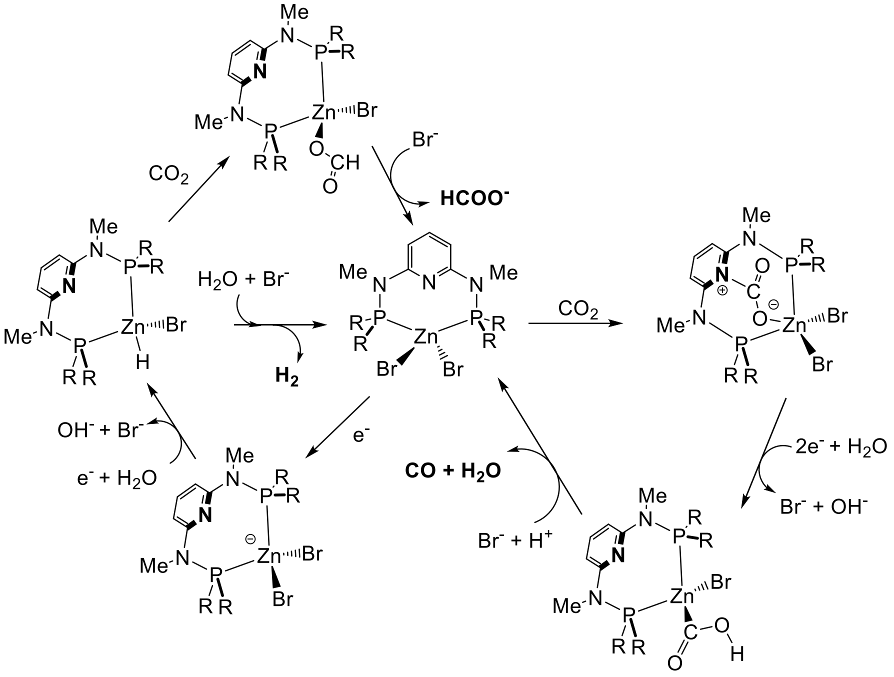

Conclusion:

In summary, we were able to prepare four new Zn(II) phosphino-pyridyl complexes, **3.1**. **3.2**, **3.3** and **3.4**. When comparing **3.1** and **3.3**, their PN^3P ligands differ with how closely the pyridyl N binds the metal center. **3.1** showed interesting bonding leaving a weakly coordinated or uncoordinated pyridyl group, which may play a role in its chemistry. **3.1** and **3.2** were studied for their electrocatalytic potential for H_2O and CO_2 reduction, where the performance parameters of these species are similar, but **3.1** was studied more thoroughly using bulk measurements due to its pendent basic site as well as its lower potential for CO_2. Further computations seen in **Table 3.6** and **Figure 3.21** combined with the results from the bulk electrolysis of **3.1** lead to a possible mechanism seen in **Scheme 3.4**, in which two pathways can be followed to produce the reduction products CO and formate. For future work, more experiments for the electrocatalytic ability should be more carefully investigated, as well as more substantial evidence for the mechanism should be explored, such as a possible intermediate synthesis by chemical reduction which would then be exposed to analogous bulk electrolysis experiments to compare to results seen in **Table 3.3**.

Experimental:

General Methods

Reactions were performed in a glovebox under a nitrogen atmosphere, with the exception of ligand synthesis, which was performed using standard Schlenk techniques under a flow of N_2. All solvents were sparged with nitrogen and then dried by passage through a column of activated alumina using an apparatus purchased from Anhydrous Engineering. Deuterated solvents were dried using activated molecular sieves. All other chemicals were purchased from Sigma-Aldrich and used without further purification. Ligands were synthesized based on literature.[24,25] Dried acetonitrile was purchased from Sigma-Aldrich and stored on molecular sieves in a glovebox. ^{1}H, $^{13}C\{^{1}H\}$ and $^{31}P\{^{1}H\}$ NMR spectra were recorded at 300.0, 75.0 and 121.5 MHz respectively with chemical shifts reported in ppm using the residual protons of the NMR solvent as internal standards. Elemental analysis was performed by Midwest Microlab, LLC, Indianapolis, IN.

Electrochemistry: All cyclic voltammetry experiments have been carried out in a three neck round bottom flask. Samples were prepared in a glove box and sealed before removing for measurement. Cyclic voltammetry was performed using a VersaSTAT 3 (Princeton Applied Research) potentiostat. A conventional three electrode system was employed. A glassy carbon electrode (diameter = 0.4 cm) was used as the working electrode, a Pt wire as the auxiliary electrode, and an Ag wire was used as a pseudo-reference electrode. For bulk electrocatalytic reduction experiments, a glassy carbon rod (diameter = 0.4 cm; length 2 cm) was used as the working electrode, a coiled Pt wire as the auxiliary electrode, and an Ag wire was used as a pseudo-reference electrode. The Pt electrode was separated from rest of electrolyte solution by a porous frit. Ferrocene was added as an internal reference after purging with N_2 and measured before and after water addition. Tetrabutylammoniumhexafluorophosphate ($(n\text{-}Bu)_4NPF_6$, TBAHFP), the supporting electrolyte, was crystallized two times with dried methanol and dried in vacuum at 90 °C for 24 h before use and stored in the glove box. The electrolyte solution, 0.1 M $(n\text{-}Bu)_4NPF_6$ in CH_3CN, was saturated with N_2 by purging (purity ⩾ 99.8%, BOC gases) for 15 minutes prior to each experiment. The concentration of catalyst was 1 mM (15 mL acetonitrile) in each experiment. Hydrogen production was measured using an Agilent 7820A gas chromatograph (GC) equipped with a thermal conductivity detector (TCD) analyzer using an Agilent select permanent gases column. The amount of H2 was determined using a calibration curve.

Syntheses

Synthesis of N-(diphenylphosphino)-2-methylaminopyridine (PN-Me): A solution of 1.08 g (10.0 mmol) of 2- (methylamino)pyridine in 25 mL of diethyl ether was cooled to −78 °C. n-BuLi (10 mmol, 1.6 M in hexane, 6.25 mL) was added drop wise and the solution was stirred for 2 h. A solution of PPh_2Cl (10 mmol, 2.2 g) taken in 10 mL diethylether was added dropwise and the solution was allowed to warm at room temperature. This reaction mixture was stirred overnight. The reaction mixture was filtered twice and the solvent was removed to give a colorless liquid which was further kept under vacuum for 24 h at room temperature to give colorless solid. Yield; 2.28 g (78%).^{1}H NMR (400 MHz, $CDCl_3$): δ = 2.96 (3H, d, J = 1.56 Hz), 6.75−6.79 (m, 1H), 7.39−7.55 (m, 12 H), 8.28−8.30 (m, 1H). ^{13}C{^{1}H} NMR (100 MHz, $CDCl_3$): δ = 34.1 (d, J = 8.6 Hz), 110.5 (d, J = 41.4 Hz), 114.6 (d, J = 1.0 Hz), 128.4 (d, J = 5.8 Hz), 129.0, 131.9 (d, J = 20.4 Hz), 136.6 (d, J = 14.8 Hz), 137.0 (d, J = 3.0 Hz), 147.6 (d, J = 1.7 Hz), 161.3 (d, J = 26.9 Hz). ^{31}P{1H} NMR (162 MHz, $CDCl_3$): δ = 51.0.

Synthesis of N,N′-bis(diphenylphosphino)-2,6-di(methylamino)pyridine (PN^{3}P-Me): n-Butyllithium (1.6 M in hexane, 8.0 mmol, 5.0 mL) was drop wise added to a toluene (100 mL) solution of N,N'-dimethyl-2,6-diaminopyridine (1.0 g, 7.3 mmol) cooled in an ice-salt bath. The mixture was stirred at room temperature for 2 h and was then cooled to –78 °C using dry ice acetone bath. To this mixture 1.3 mL (7.3 mmol) of chlorodiphenylphosphine was added. The resulting reaction mixture was stirred for 2 h at room temperature and refluxed for 18 h. The solution was cooled to room temperature and filtered twice with a frit. The above procedure was then repeated with the resulting yellow solution. After filtering, the solvent of resulting reaction mixture was removed under vacuum yielding a yellow oil. This oil dissolved in acetonitrile and the mixture was heated to reflux for 10 minutes. Upon cooling at room temperature, a white precipitate formed. The acetonitrile was decanted off and the compound was dried under vacuum. Yield: 1.70 g (46%). ^{1}HNMR (400 MHz, $CDCl_3$): δ = 2.92 (6H, d, J = 1.72 Hz), 6.90 (dd, 2H, J = 2.44, 8.04), 7.38−7.49 (m, 21 H). ^{13}C{1H} NMR (100 MHz, $CDCl_3$): δ = 33.9 (d, J = 8.6 Hz), 99.7 (d, J = 21.1 Hz), 128.3 (d, J = 5.8 Hz), 128.7, 132.0 (d, J = 20.7 Hz), 137.4 (d, J = 15.8 Hz), 138.2 (t, J = 3.2 Hz), 159.5 (dd, J = 2.08, 27.2 Hz). ^{31}P{^{1}H} NMR (162 MHz, $CDCl_3$): δ = 49.5.

N,N′-bis(diphenylphosphino)-2,6-diaminopyridine (PN^{3}P-H): 20 mmol (2.18 g) of 2,6-diaminopyridine was dried overnight in a Schlenk flask, transfered to the glove box and 40 mL of THF was added. The flask was taken from the glove box and connected to Schlenk line to purge with N_2 and cooled to -70 °C. 44 mmol of triethylamine (Et_3N) was dissolved in 10 mL THF and was added drop wise to the solution. 44 mmol (2.1 equivalent) of chlorodiphenylphosphine (PPh_2Cl) in 10 mL THF was added drop wise over 10 minutes with stirring. The solution was allowed to warm to room temperature and set to reflux overnight. Then, the solution was transferred to glove box and filtered, washed with anhydrous hexane for three times. The solvent was removed under vacuum to afford the ligand. The ligand was stored in the glovebox. Yield: 87%. ^{1}H NMR (400 MHz, $CDCl_3$): δ(ppm) = 7.82-7.62 (m, 9H), 7.61-7.54 (m, 3H), 7.53-7.40 (m, 8H), 7.40-7.27 (m, 3H), 3.78-3.49 (br s, 2H, NH). 31P{1H} NMR (161.8 MHz, DMSO): δ(ppm) = 25.46 (s, PN). MS-ESI: (m/z): 478.4. Elemental analysis calculated for $C_{29}H_{25}N_3P_2$ (Mr . 477.1): C, 72.95; H, 5.28; N, 8.80. Found: C, 72.65; H, 5.03; N, 8.56%.

Synthesis of the N-(diphenylphosphinoamino) pyridine (PN-H): A solution of 2-aminopyridine (1.00 g, 10.6 mmol) in 50 mL toluene was cooled to −78 °C, and then triethylamine (1.50 mL, 10.6 mmol) and Ph_2PCl (2.0 mL, 10.6 mmol) were slowly added drop wise to the solution. The reaction mixture was allowed to reach room temperature and further stirred for 4 h at room temperature. After this time, the mixture was filtered off to remove the precipitated triethylamine hydrochloride. The precipitate was washed with toluene. The washings and the filtrate were combined and taken to dryness under reduced pressure (rotovap) leaving a pale yellow oil which on cooling spontaneously crystallized. The material was removed from the flask and washed with MeOH and then diethyl ether and dried under vacuum. Yield 70%. ^{1}H NMR (200 MHz, $CDCl_3$) δ (ppm): 6.40 (1H, s, br, N–H), 6.76 (1H, t, J = 6.4 Hz, Py), 7.2 (1H, d, J = 8.4 Hz, Py), 7.37–7.40 (6H, m, Ph), 7.47–7.52 (4H, m, Ph), 7.59 (1H, t, J = 7.2 Hz, Py), 8.03 (1H, d, J = 5.2 Hz, Py). ^{31}P{H}-NMR (161.9 MHz, $CDCl_3$) δ (ppm): 26.0.

Synthesis of $[Zn(2,6\text{-}\{Ph_2PNMe\}_2(NC_5H_3)Br_2]$ (3.1): A solution of ligand N,N′-bis(diphenylphosphino)-2,6-di(methylamino)pyridine (0.202 g, 0.4 mmol) in 5 mL of toluene was added to a toluene solution of $ZnBr_2$ (0.089 g, 0.4 mmol) in a glove box. The reaction mixture was stirred for 16 h at room temperature under N_2. The resulting mixture was then kept in the refrigerator and colourless precipitate was removed by filtration to give complex **3.1**. Single crystals were grown by slow diffusion of hexane into a concentrated solution of the complex in dichloromethane. Yield 0.236 g (81%). ^{1}H NMR (300 MHz, $CDCl_3$, 25 °C): δ = 2.85 (s, 6H, CH_3), 6.46 (d, 2H, J = 8.10 Hz), 7.26−7.41 (m, 13H), 7.52−7.58 (m, 7H), 7.70 (t, 1H, J = 8.1 Hz). ^{13}C{^{1}H} NMR (75 MHz, $CDCl_3$): δ = 33.1 (t, CH3, J = 2.9 Hz), 99.6, 128.2 (t, J = 15.5 Hz), 128.8 (t, J = 4.7 Hz), 131.1, 133 (t, J = 7.3 Hz), 141.6 (t, J = 2.2 Hz), 156 (t, J = 6.8 Hz). ^{31}P{^{1}H} NMR (121.5 MHz, $CDCl_3$): δ = 22.5. Elemental Analysis calculated for $C_{31}H_{29}Br_2N_3P_2Zn$: C, 50.95; H, 4.00; N, 5.75. Found: C, 51.28; H, 4.33; N, 5.49.

Synthesis of [Zn(2-{Ph_2PNMe}(NC_5H_3)Br_2] (3.2): A solution of ligand N,N-bis(diphenylphosphino)-2- (methylamino)pyridine (0.392 g, 1.0 mmol) in 10 mL of toluene was added to a toluene solution of $ZnBr_2$ (0.225 g, 1.0 mmol) in a glove box. The reaction mixture was stirred for 16 h at room temperature under N_2. 50 mL of hexane was added to the resulting mixture and colourless precipitate was removed by filtration to give complex **3.2**. Single crystals were grown by slow diffusion of hexane into a concentrated solution of the complex in dichloromethane. Yield 0.561 g (91%). ^{1}H NMR (400 MHz, $CDCl_3$, 25 °C): δ = 3.65 (d, 3H, CH_3, J = 3.6 Hz), 7.00 (d, 1H, J = 8.68 Hz), 7.10 (t, 1H, J = 6.38 Hz), 7.51−7.62 (m, 6H), 7.72−7.78 (m, 4H), 7.89 (t, 1H, J = 8.08 Hz), 8.42 (d, 1H, J = 2.66 Hz). ^{13}C{^{1}H} NMR (100.7 MHz, $CDCl_3$, 25 °C): δ = 34.3 (d, CH3, J = 6.26 Hz), 110.2 (d, J = 2.08 Hz), 117.4 (d, J = 2.86 Hz), 125.8 (d, J = 36.36 Hz), 129.6 (d, J = 10.32 Hz), 132.5 (d, J = 1.68 Hz), 133.3 (d, J = 15.32 Hz), 142.4, 147.2 (d, J = 4.16 Hz), 156.9 (d, J = 11.88 Hz),. ^{31}P{^{1}H} NMR (162 MHz, CDCl3, 25 °C): δ = 27.7. Elemental Analysis calculated for $C_{18}H_{17}Br_2N_2PZn$: C, 41.78; H, 3.31; N, 5.41 Found: C, 41.87; H, 3.04; N, 5.63

Synthesis of $[Zn(2,6\text{-}\{Ph_2PNH\}_2(NC_5H_3)Br_2]$ (3.3): 0.24 g (0.5 mmol) of N,N′-bis(diphenylphosphino)-2,6-diaminopyridine in 5 mL in dichloromethane was added to 0.12 g (0.5 mmol) of $ZnBr_2$ in THF under N_2 and the solution was stirred overnight. Hexanes was then added, and a white precipitate formed and was collected. The precipitate was further washed with hexanes and then dried on a rotary evaporator. Yield was 70% (0.245 g, 0.35 mmol). Solid was then crystallized by dissolving in 1:1 CH_3CN:EtOH and diffusion of ether. ^{1}HNMR (400 MHz, d-DMSO): δ(ppm): 7.4(m, 8H), 7.3 (m, 13H), 7.2 (2H, t), 6.25 (2H, d) $^{31}P\{^1H\}$ NMR (162 MHz, d-DMSO): δ(ppm): 22.6

Synthesis of $[Zn(2\text{-}\{Ph_2PNH\}(NC_5H_3)Br_2]$ (**3.4**): same as for **3.3** but N-(diphenylphosphinoamino) pyridine (0.14 g, 0.5 mmol) added instead of PN^3P-H and yield was 64% (0.16 g, 0.32 mmol). ^{1}HNMR (400 MHz, d-DMSO): δ(ppm): 7.9 (1H, d) 7.54 (2H, d) 7.43 (5H, m) 7.33 (5H, m), 6.89 (1H, d), 6.63 (1H, t) $^{31}P\{^1H\}$ NMR (162 MHz, d-DMSO): δ(ppm): 22.65

Appendix:

Table 3.7 Crystal data and structure refinement for **3.1** and **3.2**

	3.1	**3.2**
Empirical formula	$C_{31}H_{29}Br_2N_3P_2Zn$	$C_{18}H_{17}Br_2N_2PZn$
Formula weight	730.70	517.49
Temperature (K)	200(2)	200(2)
Wavelength (Å)	0.71073	0.71073
Crystal system	Hexagonal	Monoclinic
Space group	P 61	$P\ 2_1$
a (Å)	10.6902(2)	9.2997(12)
b (Å)	10.6902(2)	17.268(2)
c (Å)	46.4469(9)	12.0322(15
α (deg)	90	90
β (deg)	90	92.223(2)
γ (deg)	120	90
Volume (Å 3)	4596.83(19)	1930.8(4)
Z	6	4
Density (calculated) (Mg/m3)	1.584	1.780
Absorption coefficient (mm-1)	3.539	5.495
Reflections collected	19945	19945
Independent reflections	9485 [R(int) = 0.0266]	9485 [R(int) = 0.0266]
Final R indices [I>2sigma(I)]	R1 = 0.0421, wR2 = 0.1026	R1 = 0.0302, wR2 = 0.0583
R indices (all data)	R1 = 0.0467, wR2 = 0.1047	R1 = 0.0478, wR2 = 0.0633

Table 3.8 Selected Bond lengths [Å] and angles [°] for **[Zn(2,6-{Ph_2PNMe}$_2$(NC_5H_3)Br_2] (3.1)**

Bond	[Å]
Zn(1)-Br(2)	2.3868(15)
Zn(1)-Br(1)	2.4016(13)
Zn(1)-P(1)	2.424(3)
Zn(1)-P(2)	2.425(3)
P(1)-N(1)	1.709(8)
P(2)-N(3)	1.713(9)
Angle	[°]
Br(2)-Zn(1)-Br(1)	115.50(5)
Br(2)-Zn(1)-P(1)	108.50(8)
Br(1)-Zn(1)-P(1)	107.52(8)
Br(2)-Zn(1)-P(2)	109.68(8)
Br(1)-Zn(1)-P(2)	101.92(8)
P(1)-Zn(1)-P(2)	113.76(9)
C(2)-N(1)-P(1)	116.3(6)
C(1)-N(1)-P(1)	123.2(7)
C(2)-N(1)-C(1)	120.2(8)
C(6)-N(3)-C(7)	119.7(9)
C(6)-N(3)-P(2)	116.9(7)
C(7)-N(3)-P(2)	123.0(7)

Table 3.9 Selected Bond lengths [Å] and angles [°] for the two molecules of **[Zn(2-{Ph$_2$PNMe}(NC$_5$H$_3$)Br$_2$] (3.2)** in the asymmetric unit.

Bond	[Å]	Bond	[Å]
N(1)-Zn(1)	2.067(4)	N(3)-Zn(2)	2.091(4)
P(1)-Zn(1)	2.4030(13)	P(2)-Zn(2)	2.4045(13)
Br(1)-Zn(1)	2.3400(8)	Br(3)-Zn(2)	2.3302(8)
Br(2)-Zn(1)	2.3368(8)	Br(4)-Zn(2)	2.3485(8)
Angle	[°]	Angle	[°]
N(1)-Zn(1)-Br(2)	110.18(11)	N(3)-Zn(2)-Br(3)	107.25(12)
N(1)-Zn(1)-Br(1)	109.79(12)	N(3)-Zn(2)-Br(4)	111.23(11)
Br(2)-Zn(1)-Br(1)	118.26(3)	Br(3)-Zn(2)-Br(4)	117.82(3)
N(1)-Zn(1)-P(1)	81.58(11)	N(3)-Zn(2)-P(2)	80.53(11)
Br(2)-Zn(1)-P(1)	110.57(4)	Br(3)-Zn(2)-P(2)	124.86(4)
Br(1)-Zn(1)-P(1)	120.21(4)	Br(4)-Zn(2)-P(2)	108.36(4)

Table 3.10 Crystal data and structure refinement for **3.3** and **3.4**

	3.3	**3.4**
Empirical formula	$C_{64}H_{63}Br_4N_7OP_4Zn_2$ $(C_2H_5)_2O$ and CH_3CN	$C_{17}H_{15}Br_2N_2PZn$
Formula weight	1520.47	503.47
Temperature (K)	200(2)	296(2)
Wavelength (Å)	0.71073	0.71073
Crystal system	Monoclinic	Monoclinic
Space group	P 21/c	P 2_1/n
a (Å)	18.323(2)	11.5085(5)
b (Å)	19.036(2)	8.0518(3)
c (Å)	19.746(2)	26.8422(13)
α (deg)	90	90
β (deg)	93.162(2)	101.549(3)
γ (deg)	90	90
Volume (Å^3)	6876.9(14)	2436.95(18)
Z	4	4
Density (calculated) (Mg/m^3)	1.469	1.372
Absorption coefficient (mm^{-1})	3.159	4.352
Reflections collected	74867	34318
Independent reflections	14168 [R(int) = 0.0683]	5070 [Rint = 0.0716, Rsigma = 0.0485]
Final R indices [I>2sigma(I)]	R1 = 0.0452, wR2 = 0.0452	R1 = 0.0384, wR2 = 0.0804
R indices (all data)	R1 = 0.1091, wR2 = 0.1010	R1 = 0.0888, wR2 = 0.0960

Table 3.11 Selected Bond lengths [Å] and angles [°] for for the two molecules of **[Zn(2,6-$\{Ph_2PNH\}_2(NC_5H_3)Br_2$] (3.3)** in the symmetric unit

Bond	[Å]	Bond	[Å]
Br(1)-Zn(1)	2.4637(8)	Br(3)-Zn(2)	2.3979(9)
Br(2)-Zn(1)	2.4087(8)	Br(4)-Zn(2)	2.4120(9)
N(2)-Zn(1)	2.472(4)	N(5)-Zn(2)	2.525(4)
P(1)-Zn(1)	2.4510(14)	P(3)-Zn(2)	2.4443(15)
P(2)-Zn(1)	2.4527(14)	P(4)-Zn(2)	2.4364(15)
Angle	[°]	Angle	[°]
Br(2)-Zn(1)-P(1)	108.89(4)	Br(3)-Zn(2)-Br(4)	111.25(3)
Br(2)-Zn(1)-P(2)	101.40(4)	Br(3)-Zn(2)-P(4)	107.65(5)
P(1)-Zn(1)-P(2)	132.11(5)	Br(4)-Zn(2)-P(4)	104.37(4)
Br(2)-Zn(1)-Br(1)	110.55(3)	Br(3)-Zn(2)-P(3)	105.53(4)
P(1)-Zn(1)-Br(1)	101.81(4)	Br(4)-Zn(2)-P(3)	101.43(4)
P(2)-Zn(1)-Br(1)	101.10(4)	P(4)-Zn(2)-P(3)	126.20(5)
Br(2)-Zn(1)-N(2)	93.13(10)	Br(3)-Zn(2)-N(5)	90.58(10)
P(1)-Zn(1)-N(2)	71.47(10)	Br(4)-Zn(2)-N(5)	158.11(10)
P(2)-Zn(1)-N(2)	70.66(10)	P(4)-Zn(2)-N(5)	68.73(10)
Br(1)-Zn(1)-N(2)	156.18(10)	P(3)-Zn(2)-N(5)	69.83(10)

Table 3.12 Selected Bond Lengths Å Bond Angles [°] for **[Zn(2-{Ph_2PNH}(NC_5H_3)Br_2] (3.4**)

Bond	[Å]
Br1-Zn1	2.3355(6)
Br2-Zn1	2.3430(6)
Zn1-N1	2.062(3)
Zn1-P1	2.4114(10)
Angle	[°]
N1-Zn1-Br1	109.63(9)
N1-Zn1-Br2	109.11(9)
Br1-Zn1-Br2	118.21(2)
N1-Zn1-P1	82.30(9)
Br1-Zn1-P1	110.90(3)
Br2-Zn1-P1	120.41(3)

References:

1) N. Elgrishi, M. B. Chambers, X. Wang and M. Fontecave, *Chem. Soc. Rev.*, 2017, **46**, 761.

2) J. Bonin, A. Maurin and M. Robert, *Coord. Chem. Rev.*, 2017, **334**, 184.

3) H. Takeda, C. Cometto, O. Ishitani and M. Robert, *ACS Catal.*, 2017, **7**, 70–88.

4) Y. Yamazaki, H. Takeda and O. Ishitani, *J. Photochem. Photobiol. C Photochem. Rev.*, 2015, **25**, 106.

5) K. E. Dalle, J. Warnan, J. J. Leung, B. Reuillard, S. Karmel, Isabell, E. Reisner, *Chem. Rev.*, 2019, **119**, 2752.

6) R. Reithmeier, C. Bruckmeier, B. Rieger, *Catalysts*, 2012, **2**, 544.

7) S. Kissling, P. T. Altenbuchner, T. Niemi, T. Repo and B. Rieger, in *Zn in Catalysis. Applications in Organic Synthesis*, eds. S. Enthaller and X.-F. Wu, Wiley-VCH Verlag GmbH & Co., Weinheim, Germany, 2015, pp. 179.

8) S. Klaus, M. W. Lehenmeier, C. E. Anderson, B. Rieger, *Coord. Chem. Rev.*, 2011, **255**, 1460.

9) M. Kato, T. Ito, *Inorg. Chem.*, 1985, **24**, 504.

10) M. Kato, T. Ito, *Inorg. Chem.*, 1985, **24**, 509.

11) M. N. Collomb-Dunand-Sauthier, A. Deronzier, R. Ziessel, *J. Phys. Chem.*, 1993, **97**, 5973.

12) R. Dobrovetsky, D. W. Stephan, *Angew. Chemie - Int. Ed.*, 2013, **52**, 2516.

13) Y. Li, K. Junge, M. Beller, in *Zn in Catalysis. Applications in Organic Synthesis*, eds. S. Enthaller and X.-F. Wu, Wiley-VCH Verlag GmbH & Co., Weinheim, Germany, 2015, 5

14) W. Sattler, G. Parkin, *J. Am. Chem. Soc.*, 2012, **134**, 17462.

15) Y. Wu, J. Jiang, Z. Weng, M. Wang, D. L. J. Broere, Y. Zhong, G. W. Brudvig, Z. Feng,

H. Wang, *ACS Cent. Sci.*, 2017, **3**, 847.

16) E. S. Donovan, B. M. Barry, C. A. Larsen, M. N. Wirtz, W. E. Geiger,R. A. Kemp, *Chem. Commun.*, 2016, **52**, 1685.

17) S. P. Cronin, J. M. Strain, M. S. Mashuta, J. M. Spurgeon, R. M. Buchanan, C. A. Grapperhaus, *Inorg. Chem.*, 2020, **59**, 4835–4841.

18) S. P. Cronin, A. Al Mamun, M. J. Toda, M. S. Mashuta, Y. Losovyj, P. M. Kozlowski, R. M. Buchanan, C. A. Grapperhaus, *Inorg. Chem.*, 2019, **58**, 12986.

19) J. Burt, W. Levason, G. Reid, *Coord. Chem. Rev.*, 2014, **260**, 65.

20) R. E. Desimone, G. D. Stucky, *Inorg. Chem.*, 1971, **10**, 1808.

21) W. Sattler, G. Parkin, *J. Am. Chem. Soc.*, 2011, **133**, 9708.

22) N. Elgrishi, K. J. Rountree, B. D. McCarthy, E. S. Rountree, T. T. Eisenhart, J. L. Dempsey, *J. Chem. Educ.*, 2018, **95**, 197.

23) A. Z. Haddad, B. D. Garabato, P. M. Kozlowski, R. M. Buchanan and C. A. Grapperhaus, *J. Am. Chem. Soc.*, 2016, **138**, 7844.

24) G. K. Rao, W. Pell, B. Gabidullin, D. Richeson, *Chem. Eur. J.*, 2017, **23**, 16763.

25) Y. Hameed, B. Gabidullin, D. Richeson, *Inorg Chem.*, 2018, **57**, 13092.

Chapter IV

Perimidine Based NHCs

Introduction:

A carbene displays a neutral carbon center having two electrons involved in bonding with substituents with the remaining two electrons being unshared and remaining on the C center. The general geometries of disubstituted carbenes are linear or bent (**Figure 4.1**). For a linear arrangement, the carbene center would have an approximate sp-hybridization with the two remaining p orbitals remaining perpendicular to each other as well as to the axis of the molecule. In this case, the carbene would show a triplet ground state with one unpaired electron in each of the non-bonding p orbitals as expected by Hund's rule. When the carbene center has a bent geometry, perhaps as an effect of the substituents, the carbon would now be assigned a valence bond description of sp^2 hybridization. This results in the non-bonding orbitals being inequivalent and possessing different orbital energies. Obviously, the difference in energies between these two structures will determine whether a carbene prefers the singlet or triplet state in terms of energy. Regarding this, the size of the energy gap between the sp^2 and p orbitals is the key to clarify the most stable state. When the energy gap between the sp^2 and p orbitals is larger than the pairing energy for the doubly occupied orbital, the singlet state is preferred. Usually, a singlet-triplet gap of 7.6 x 10^{-23} kcal or more results in a singlet ground state and a gap less than 5.7 x 10^{-23} kcal yields a triplet ground state.[1] Bond angles are 125-140° for triplet methylene and 102° for singlet methylene (as determined by EPR).[2]

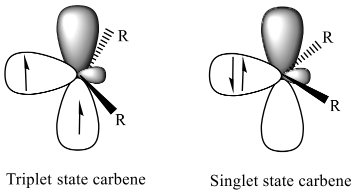

Figure 4.1 Simple orbital pictures for linear and bent carbenes.

Background of NHCs

The first room-temperature stable carbene, reported in the early 1990's, was the five membered heterocyclic species 1,3-di-1-adamantylimidazol-2-ylidene (**Figure 4.2**).[3] This species is a singlet carbene. From this discovery, several examples of related N-heterocycle carbenes (NHCs) were introduced. Since the development of the first examples, there have been significant success in NHC chemistry, leading to isolable and commercial compounds.[4,5] Even though a carbene has only 6 electrons, making it an electron deficient compound, the carbene center of an NHC is typically used as a nucleophile since it possesses a pair of nonbonding electrons that could interact with an electrophilic center. As a result, carbenes behave as ligands, donating their lone electron pairs to a metal and can stabilize transition metal compounds. The applications of NHCs as ligands rapidly expanded and today NHCs have become rather ubiquitous donor ligands putting them in the same class of ligands as phosphines in transition metal catalyzed reactions.[6,7]

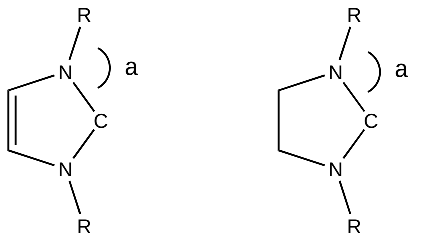

A B

Figure 4.2 Five membered carbenes

In terms of the stability of five-membered ring structures, carbenes having an unsaturated structure like **A** are more stable, a feature that has been attributed to the 6π electron aromatic nature of these compounds. However, both types of carbenes are considered as stable ligands since the empty p_z orbital on the carbene center can be stabilized by π overlap with the non-bonding electrons of the flanking nitrogen centers. On top of that, the five-membered heterocycle forces the carbene to have a bent structure with an ideal angle of approximately 108°. Therefore, the fact that singlet state is the preferred electron arrangement can be explained by these factors.

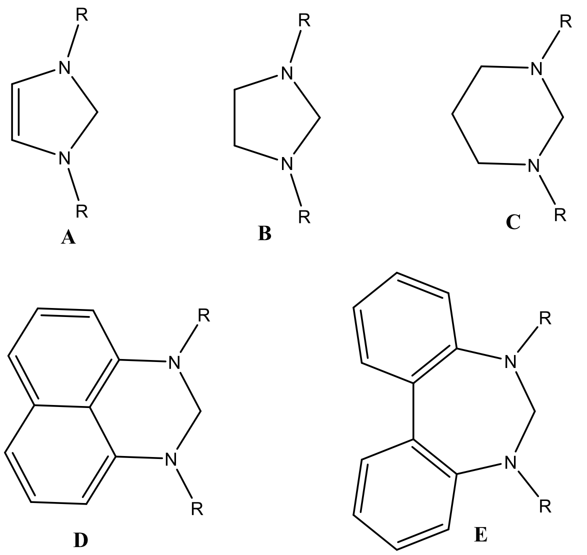

A B C

D E

Figure 4.3 Common NHC frameworks

The past few decades have demonstrated that changes to the size of the heterocyclic ring can affect the donor strength and steric impact of the ligand. Expanding on the variety of structures and electronics of these ligands will reveal novel applications of these compounds, and reports of scaffolds for stable free carbenes (**Figure 4.3**) such as **C**[8,9] , **D** and **E**[10] have also emerged. Understanding the central properties of innovative carbenes is critical for the utilization of these species and for the design of new carbenes.

Overview

Our group has worked on the unique framework provided by the perimidine core of **D**, where the divalent carbon is a component of an electron-rich, extended aromatic six-membered heterocyclic ring.[11,12] This feature modulates the donor properties of the carbene center and imposes geometric constraints on the N-substituents, influencing their steric impact. This scaffold directs the N-bound groups closer to the carbene atom, decreasing the α angle and increasing the steric pressure on both the carbene and a coordinated metal.

So far only noble metal complexes, such as Rh, Ir and Pd,[13,14] have been synthesized with the perimidine NHC framework. Here we attempted to synthesize complexes with these ligands using the more earth abundant first row metals as potential electrocatalysts for CO_2 reduction.

Results and Discussion:

(^{i}Pr)(^{n}Pn)- PERI^{+}

To obtain the desired carbenes, the perimidinium cations were targeted as precursor compounds. Deprotonation of these species allows for the generation of the anticipated final stable carbene products. Regarding this, we have typically tried two different approaches. All syntheses start from 1,8-diaminonaphthalene (**DAN**) as the initial building block. The first method, shown in **Scheme 4.1**, was to use N, N'-disubstituted DAN and cyclize it in an acid reaction with excess of triethylorthoformate to form the perimidinium salt. Another approach is to use the cyclized monosubstituted perimidine and then quaternize the unsubstituted N center using an alkyl halide. The method used depended on the substituents chosen. Initially, to regrasp the procedure of this synthesis, we decided to synthesize the isopropyl-neopentyl variation, which follows the former procedure, due to its unique non-aromatic ^{1}HNMR handles and unpublished synthesis as a ligand in an organometallic complex.

Given the variety of substituents that could be applied to N,N'-disubstituted-perimidinium salt family of ligands, a shorthand notation for identifying these species is useful. With this in mind, the notation R,R'-PERI^{+}X^{-} (X=anion) is used. For example, N-isopropyl-N'-neopentyl-perimidinium salt be called (^{i}Pr)(^{n}Pn)- PERI^{+}Br^{-}. In the case of monosubstituted perimidinium I will use the notation R-PERI. In order to follow this same pattern I will follow a similar short-hand notation for the N,N'-disubstituted free carbene which will be called "R,R'-carbene".

Scheme 4.1 Synthetic route of (^{i}Pr)(^{n}Pn)- PERI^{+}Br^{-} (**4.5a**) through the intermediates **4.1**, **4.2**, **4.3** and **4.4** from starting material **DAN**.

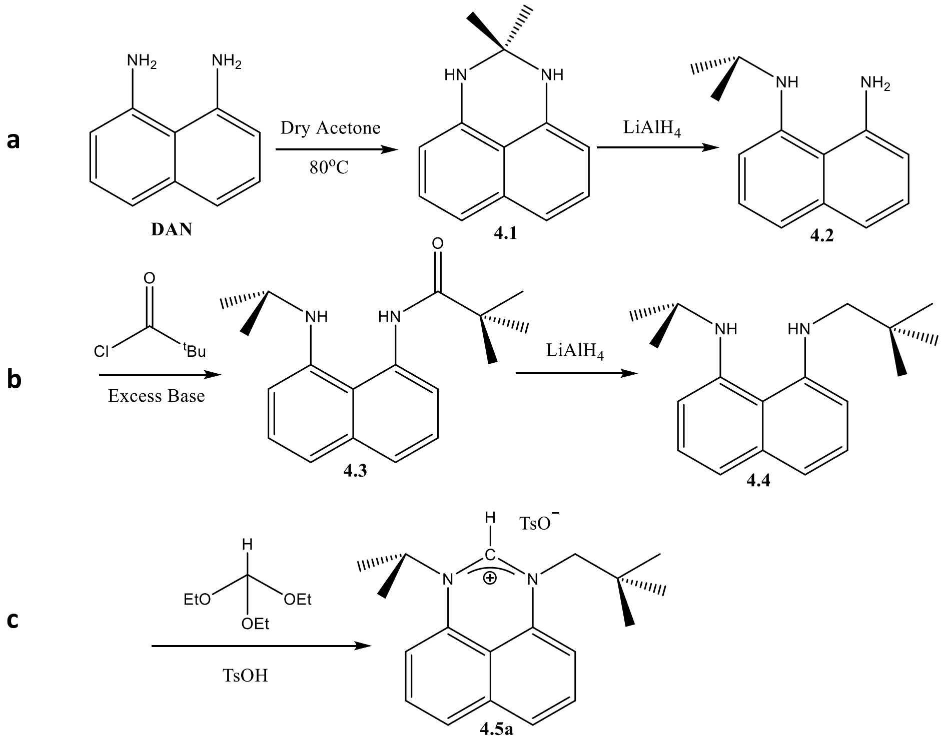

As can be seen in **c** of **Scheme 4.1**, the first method resulted in compounds that possessed counter anions that were determined by the acid used in the reaction. This can lead to issues with the targeted deprotonation step. For example, with the tosylate salt, **4.5a** (^{i}Pr)(^{n}Pn)-PERI^{+}TsO^{-}, prepared using p-toluenesulfonic acid, we found that exchanging the toslyate anion to a bromide ion was required for effective deprotonation reactions. This anion exchange step was done by substituting the acid for ammonium bromide generating the bromide salt **4.5b** (^{i}Pr)(^{n}Pn)-PERI^{+}Br^{-} . The unique feature that differentiates **4.5** from **4.4** in their respective ^{1}H NMR spectrums is the appearance of the upfield singlet appearing at δ 9.15 ppm for the cationic N-C(H)-N unit of **4.5**.

Furthermore, the one-bond CH J-coupling value ($^{1}J_{CH}$) has been shown by Meng et al., to be a useful means of measuring the NHC's sigma donation strength.[15] This relates to its hybridization as it correlates the increasing J-coupling with poorer σ-donation due to increasing s-orbital character of the C-H bond. Compound **4.5b** (^{i}Pr)(^{n}Pn)-PERI$^+$Br$^-$ was found to have a $^1J_{CH}$ coupling of 204.1 Hz. This puts the perimidine scaffold as one of the stronger σ-donors relative to the common cyclic NHCs, such as the imidazole **A** (~225 Hz) and benzimidazole (~217 Hz) scaffolds and similar to the unconjugated imidazoline **B** (~206 Hz), while slightly weaker than the unconjugated 6-membered analogue (~200 Hz).

(^{n}Pn)(^{i}Pr)-carbene

Initially, attempts to synthesize the free carbene by deprotonation of the precursor, such as **4.5** and other analogues, utilized a tert-butoxide base; however, this approach was found to lead to nucleophilic attack of the base on the perimidinium salt and to yield a σ-diamino ether. To avoid this issue, a bulkier non-nucleophilic base, potassium bis(trimethylsilyl) amide (KHMDS) was used (**Scheme 4.2**).[11]

Synthesis of (^{n}Pn)(^{i}Pr)-carbene **4.6** presented challenges, as precision was required in order to obtain the desired product. It was originally believed that deprotonation of any of the isopropyl substituted perimidiniums, due to its steric properties, would yield a monomer free carbene. In fact, a previous deprotonation of **4.5** did produce the fully characterized carbene **4.6**. However, this hypothesis would prove to be incorrect as the conditions recently used produced the enetetraamine **4.7**. Both characterization by ^{1}HNMR as well as analysis of single crystals by X-ray diffraction definitively confirmed the “dimerized” form of the free carbene of the (^{n}Pn)(^{i}Pr)-scaffold our lab had initially reported.

Scheme 4.2 Potential products **4.6** and **4.7** after treating **4.5** with KHMDS

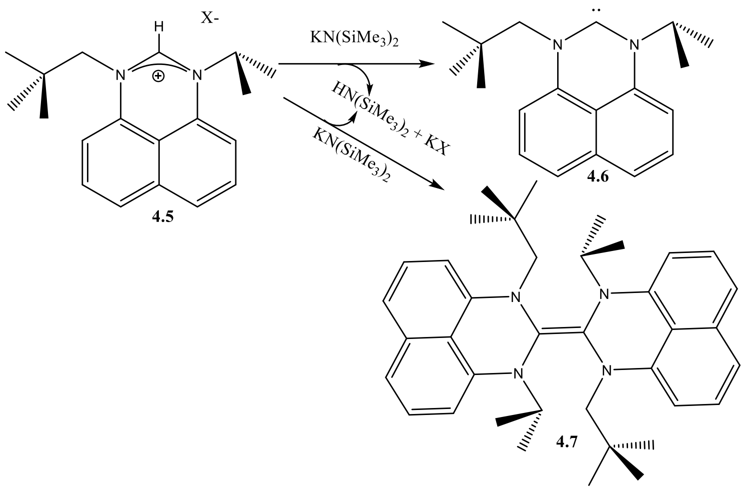

Identification of carbene or enetetraamine formation is easily confirmed with the disappearance of the downfield proton in the salt precursor. For the deprotonation (^{n}Pn)(^{i}Pr)-PERI$^+$Br$^-$ **4.5b**, the loss of the peak at δ 9.15 ppm was evidence of this. The original experimental used **4.5a** as the precursor and also crystallized in a different solvent producing the free carbene **4.6**; however, it is unclear if this is the reason for a selective product formation. In fact, even in experiments that led to **4.7,** ^{1}HNMR spectra of the reaction mixture displayed resonances of carbene **4.6**. A second ^{1}HNMR began to show evidence of dimerization where, somewhat surprisingly, splitting of certain peaks began to appear, such as the appearance of two doublets replacing the singlet representing the two protons on the methylene unit of the neopentyl substituent. These protons are equivalent and yield a singlet for **4.6** but are diastereotopic in dimer **4.7**. Importantly, dimerization of perimidine carbenes has been shown to have little effect on the ability to make transition metal complexes as seen in our previous work (**Scheme 4.3**).

Scheme 4.3 Previously synthesized Pd(II) and Rh(I) complexes by means of the dimerized perimidine NHC.

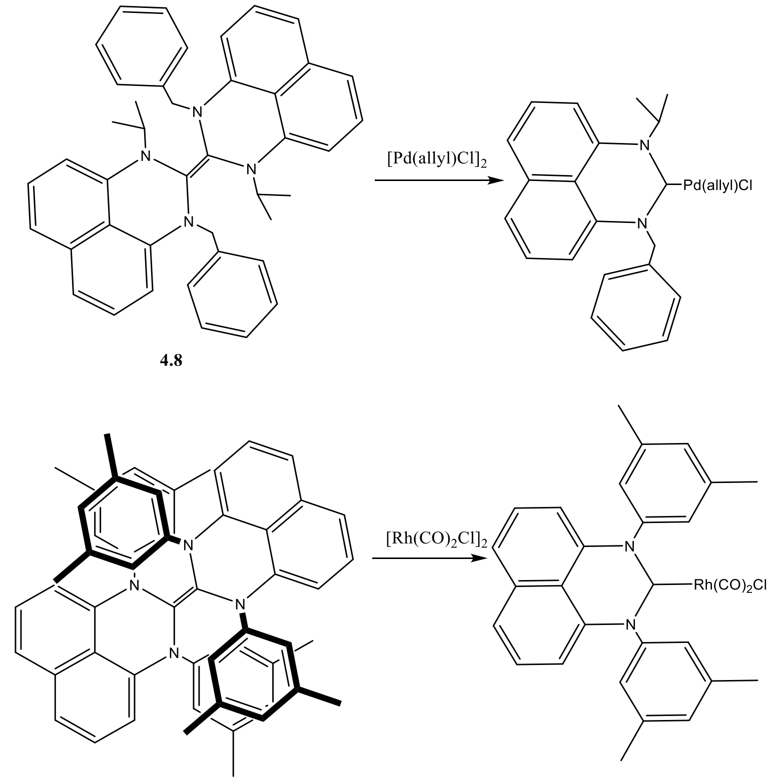

In an attempt to better understand the carbene dimerization we looked at the computed data of thermodynamic factors applied as the driving force for (^{i}Pr)(Bn)-enetetraamine **4.8**. Formation of the C=C double bond led to an energy gain of approximately 172 kcal/mol. Dimerization is favoured if the sum of the singlet/triplet energy gap of two monomers is less than that of the energy gained from the double bond formation. In the case of (^{i}Pr)(Bn)-enetetraamine **4.8**, singlet/triplet gap energy could be computed through a DFT optimization of **4.8** using the B3LYP functional and the TZVP basis set. From this computation, the difference in the free energies of the singlet and triplet forms of **4.8** (the singlet/triplet gap) was determined to be 57.7 kcal/mol. Approximately 56.6 kcal/mol energy can be gained by dimerization of both free carbenes in the triplet states. Henceforth, we can presume the perimidine carbenes have a thermodynamic preference for forming their enetetraamine counterparts.

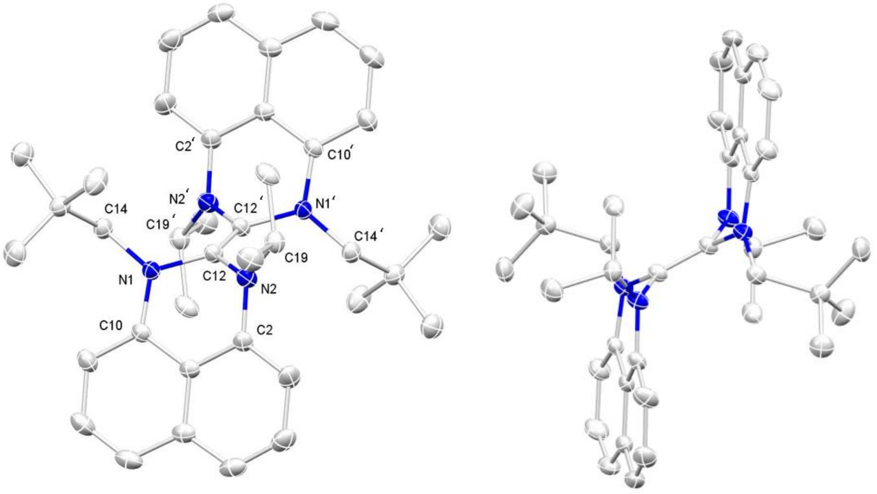

Figure 4.4 X-ray structure of **4.7**. Thermal ellipsoids are drawn at 20% probability. Hydrogen atoms have been omitted for clarity.

In some instances, the reaction resulted in a crude product ^{1}HNMR, where the appearance of several peaks can be seen, resembling a somewhat doubling of the peaks, but most interestingly was the appearance of two singlets downfield (δ 8.54 ppm and δ 8.65 ppm) that did not line up with the salt starting material as they were not as deshielded. This is believed to be due to the ineffective deprotonation of all the starting material leading to the formation of a dimer intermediate,[16] which is probably the two isomers (trans **4.9** and cis **4.10**) (**Scheme 4.4**). This highlights the importance of adding the salt gradually into the solution of KHMDS and introduces a proposed mechanism for the "dimerization".

Scheme 4.4 Proposed route of dimer intermediates, isomers **4.9** and **4.10** when half the stoichiometric amount of base is added to carbene precursor **4.5**.

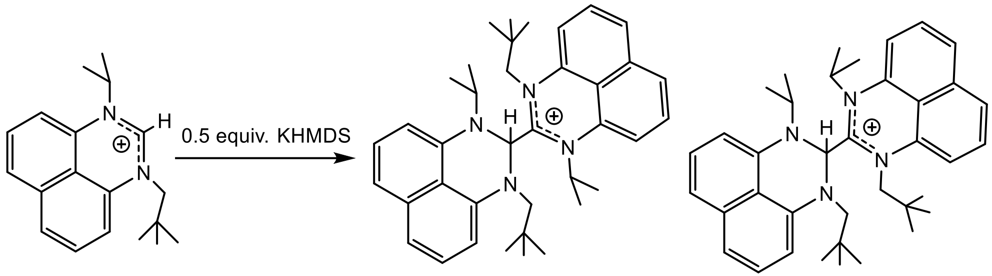

4.5 4.9 4.10

With the (^{n}Pn)(^{i}Pr)-enetetraamine in hand several attempts were made to synthesize first row transition metal organometallic complexes with (^{n}Pn)(^{i}Pr)-enetetraamine as starting material. Unfortunately, these were not successful. Major issues came from purity, in which it was difficult to utilize the small amount of crystals that formed from crystallization as well as due to the impurity of the crude product of the carbene/enetetraamine when used directly after synthesis.

Chelating Perimidine Carbene

Although we were experiencing some difficulties with employing the carbenes outlined above in coordination chemistry we remained inspired by the results of the electro and photochemistry using the PN and PN^{3}P bound transition metal complexes. As a result, we targeted to the synthesis of a bidentate pyridyl-perimidine NHC as a ligand for potential catalysts. Although the concept of polydentate pyridyl-NHC transition metal complexes as catalysts in this field is not unique,[17] this would be one of the few or possibly the first non-monodentate perimidine based NHCs produced.

Targeting this model would require a third route that would be different from those outlined above. This new route would entail the cyclization of **DAN** with formic acid generating perimidine

4.11, before the addition of the substituents (**Scheme 4.5**). The first substituent would be the pyridyl group, where **4.11** and 1-bromopyridine would undergo an Ullmann coupling reaction producing **4.12**,[18] which itself undergoes a nucleophilic reaction with methyl iodide to give the final salt product and NHC precursor (Pyr)(Me)-PERI$^+$I$^-$ **4.13**. Here the iodide salt was chosen due to the facility of using MeI (liquid) to (MeBr).

Scheme 4.5 Synthetic route of (Pyr)(Me)-PERI$^+$I$^-$ (**4.13)** through the intermediates **4.11** and **4.12** from starting material **DAN**.

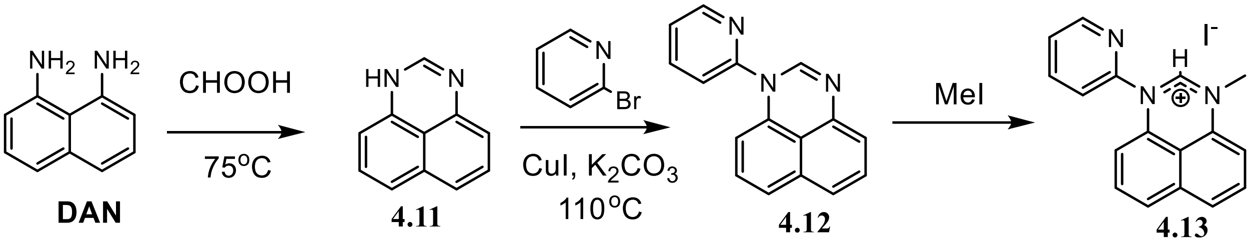

We were particularly attracted to the potential of a pyridyl-NHC bidentate species given the prevalence of bidentate pyridyl-L ligand systems for example with (pyridyl-L)Mn(CO)$_3$Br complexes. This procedure was also beneficial in the sense that the NHC did not need to be synthesized separately but would be generated in a one-pot reaction with an appropriate starting material. The procedure would include potassium tert-butoxide (tBuOK) to deprotonate the carbene precursor **4.13** and have it coordinate the bromopentacarbonylmanganese (I) at 60°C under nitrogen.

Following the procedure outlined in Scheme 4.5 and upon purification, the ^{1}HNMR produced a spectrum with broad peaks concluding an unknown product; however, fortuitously vapor diffusion of hexanes into a dichloromethane solution of the crude product resulted in isolation of crystals that were appropriate for a crystal structure. X-ray analysis (**Figure 4.2**). The results of this analysis revealed that the isolated product was a urea analogue of the (Pyr)(Me)-scaffold, represented by **4.15** with the X-ray analysis results shown in **Figure 4.3**. We believe the oxygen source to be the result of the purification being handled under air or from the extraction using water. Although the complex was unsuccessful, the formation of **4.15** did give evidence to the possible formation of the carbene due to the indication of deprotonation of **4.13** and subsequent oxidation of the N-C-N unit carbon.

Scheme 4.6 Synthesis of urea analogue, **4.15**, as a byproduct of attempt to generate **4.13** coordinated Mn(I) complex, **4.14**.

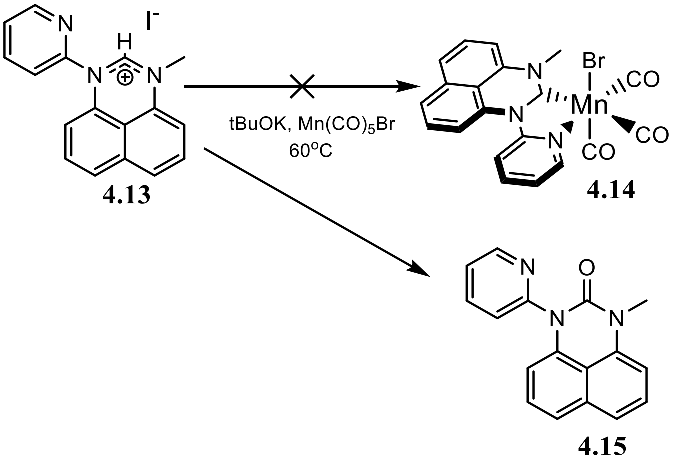

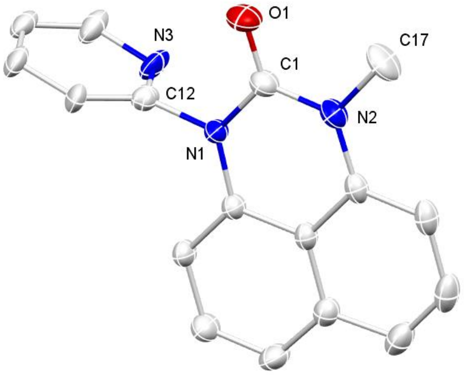

Figure 4.5 X-ray structure of **4.15**. Thermal ellipsoids are drawn at 20% probability. Hydrogen atoms are emitted for clarity.

These hints to success also prompted an attempt to prepare a Zn(II) pyridyl-carbene species. We have previously prepared pyridyl-phosphine ("PN" ligand) complexes of $ZnBr_2$ and wanted to explore the potential of a pyridyl-NHC system (Chapter III). We followed a similar procedure as above by attempting to synthesize the free carbene (**4.16**) first by deprotonation with KHMDS, followed by subsequent addition of $ZnBr_2$ in toluene to target the complex **4.17** (**Scheme 4.7**).

Complications with crystallizing the free carbene and hence purifying it required us to have to continue with the crude compound in synthesizing the complex. Unfortunately, our only source of evidence for the generation of both **4.16** and **4.17** was through ^{1}HNMR analysis, although both spectra contained a certain degree of impurities.

Scheme 4.7 Proposed synthetic route to generate **4.17**.

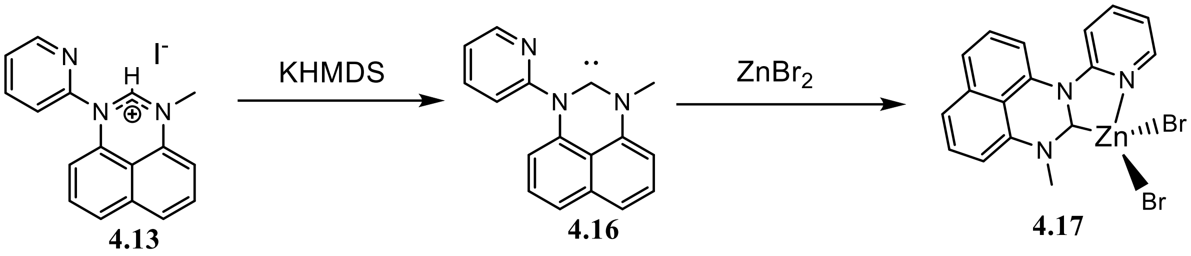

Figure 4.6 depicts the changes in the solutions as characterized by ^{1}HNMR. The red spectrum is that of the solution after the addition of the KOtBu base to (Pyr)(Me)-PERI$^+$I$^-$ (green). The main indication of a possible carbene product, **4.16**, is once again the disappearance of the down field singlet peak representing the N-CH-N unit proton at δ 9.63 ppm, while other protons can be accounted for having shifted upfield as was seen with the (^{n}Pn)(^{i}Pr) analogue. Due to struggles with crystallizing the product, the crude product was added to a solution with $ZnBr_2$, which is stirred overnight. The blue spectrum represents the ^{1}HNMR of the solution after drying. Interestingly the aromatic peaks from the pyridine and perimidine rings seem to have shifted downfield, representing deshielding, possibly due to coordination to a Lewis acidic Zn(II).

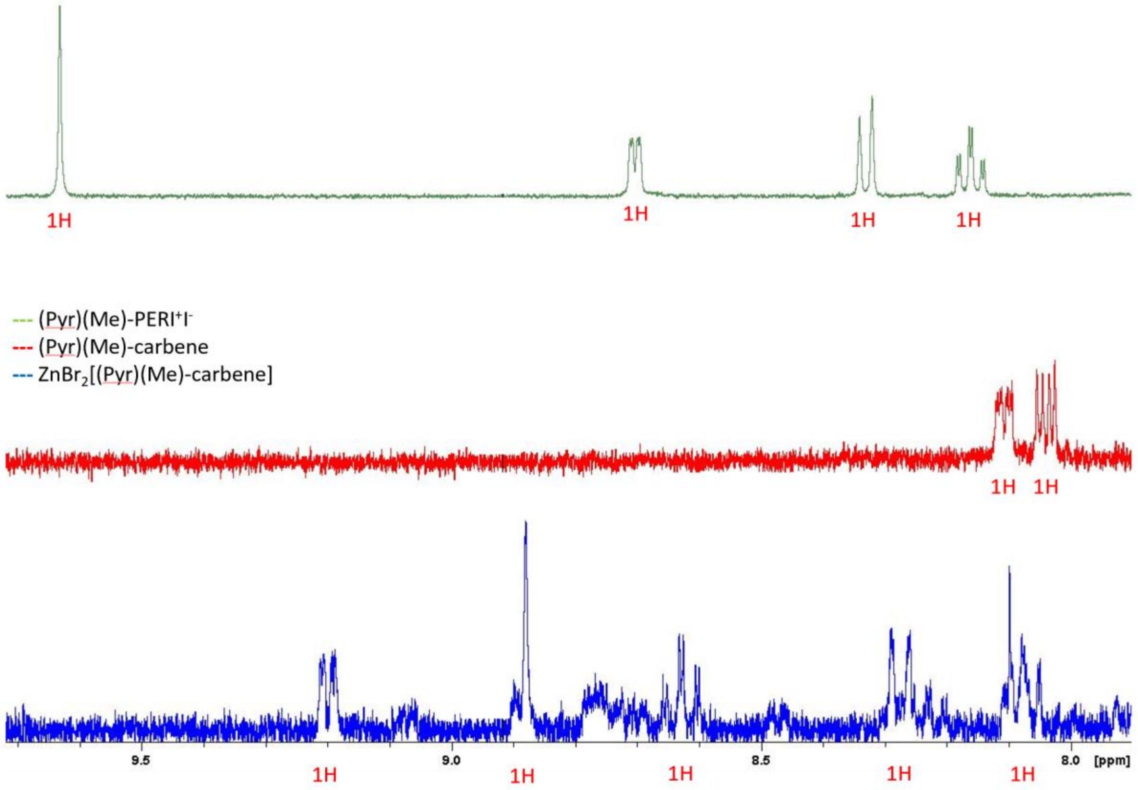

Figure 4.6 ^{1}HNMR spectra in $CDCl_3$. Green spectrum representing (Pyr)(Me)-PERI$^+$I$^-$ **4.13**. Red spectrum representing addition of KHMDS to **4.13** and possible formation of **4.16**. Blue spectrum representing addition of $ZnBr_2$ to previous product and possible formation of **4.17**.

Conclusion:

Overall, using the R,R'-DAN framework, a known permidinium scaffold, **4.5b**, was synthesized along with a novel pyridyl-perimidinium analogue **4.13**. The one-bond CH J-coupling value ($^1J_{CH}$) of **4.5b** presented the strength of the σ-donor property of these perimidine NHCs as among the stronger donors relative to alternate cyclic NHCs. The enetetramine product was also observed when attempting to deprotonate **4.5b**, which was initially believed to only exist as the free carbene due to its isopropyl substituent. This was also seen to be the computed thermodynamically favored product. Due to the constraints of time and with the desire to pursue the synthesis of a polydentate scaffold as a more feasible ligand for the field of electro/photocatalysis, synthesis of bidentate perimidine NHC coordinated complexes were attempted, using the precursor **4.13**. A urea species of **4.13** showed potential generation of a free carbene due to the deprotonation of the N-CH-C unit as well as preliminary results of a Zn(II) complex perceived by ^{1}HNMR. Future attempts to synthesize these metal complexes shouldn't be impossible with improved purification as these complexes would provide a broader avenue in understanding the effects of NHC ligands in possible electro/photocatalysis or even additional avenues in catalysis.

Experimental:

General Methods

Unless otherwise noted, all manipulations were carried out in either a nitrogen filled glovebox or under nitrogen using standard Schlenk techniques. Deuterated benzene, chloroform, and toluene were purchased from Aldrich Chemical Company. Acetone, 2-bromopyridine, 1,8-diaminonaphthalene, formic acid, $LiAlH_4$, MeI, $KN(SiMe_3)_2$, and triethylorthoformate were purchased from Aldrich Chemical Company and used without further purification. ^{1}H and spectra were run on either a Bruker 300 MHz, a Bruker 400 MHz, a Bruker 600MHz spectrometer $^{13}C\{^1H\}$ NMR were run on a Bruker 75 MHz, a Bruker 100 MHz, or a Bruker 150 MHz using the residual protons of the deuterated solvent for reference.

The crystal of **4.5b, 4.7, 4.13,** and **4.15** were mounted on thin glass fibers using paratone oil. Prior to data collection, the crystals were cooled to 201(2) K. The data were collected on a Bruker AXS single-crystal diffractometer equipped with a sealed Mo tube (wavelength 0.71073 Å) and APEX II CCD detector. The raw data collection and reduction were done with the Bruker APEXII software package. 1 Semi-empirical absorption corrections based on equivalent reflections were applied using SADABS. The structures were solved by direct methods and refined with full-matrix least-squares procedures based on F^2, using SHELXL and WinGX. All non-H atoms were refined anisotropically. All hydrogen atoms were placed in idealized positions. Displacement ellipsoid plots were produced using ORTEP.

Syntheses

Synthesis of 2,2-dimethyl-1,3-dihydroperimidine (4.1): To a Teflon screw cap-sealed flask was added **DAN** (5.0g, 31.6 mmol), activated molecular sieves (5.0g) and acetone (18.5g, 319 mmol). The reaction was heated to 80°C overnight. The reaction mixture was filtered and the solids were washed with diethylether. The ether solutions were combined and all volatiles were removed under vacuum to give 5.87g (94%) of a red/purple solid that we have identified as the aminal, 2,2-dimethyl-1,3 dihydroperimidine. ^{1}H NMR ($CDCl_3$, 200 MHz): δ 7.17-7.32 (m, 4H, CH), 6.45 (d, 2H, CH), 4.18 (br, 2H, NH), 1.40 (s, 6H, CH_3). ^{13}C NMR ($CDCl_3$, 200 MHz): δ 140.3, 134.4, 126.9, 116.6, 112.6, 105.6 (C_{arom}), 64.3 ($CHMe_2$), 28.4 ($CH(CH_3)_2$). Analysis Calcd $C_{13}H_{14}N_2$ C, 78.75; H, 7.12; N, 14.13; Found C, 78.79; H, 7.23; N, 13.98

Synthesis of N-(isopropyl)-1,8-diaminonaphthalene, (iPrNH)(NH_2)$C_{10}H_6$ (4.2): A sample of compound **4.1** (5.0g, 25.2 mmol) was dissolved in diethylether and added dropwise to a suspension of LiAlH4 (2.9g, 76 mmol) in 100 ml of diethylether that was maintained at 0°C. After addition, the reaction was allowed to warm to room temperature and stirred for an additional 12 hrs. The reaction was then quenched, at 0°C, with isopropanol followed by water. This mixture was extracted with diethylether and dried under vacuum to give **2a** as a purple oil (4.12g, 82%). ^{1}H NMR ($CDCl_3$, 300 MHz): δ 7.12-7.26 (m, 4H, CH), 6.55-6.59 (m, 2H, CH), 4.89 (br, 3H, NH), 3.60 (sept, 1H,$CHMe_2$), 1.26 (d, 6H, CH3). ^{13}C NMR (CDCl3, 300 MHz): δ 145.3, 144.1, 137.1, 126.2, 125.9, 119.9, 118.7, 117.3, 112.1, 108.5 (Carom), 45.8 ($CHMe_2$), 22.7(CH_3). Analysis Calcd $C_{13}H_{16}N_2$ C, 77.96; H, 8.05; N, 13.99; Found C, 78.21; H, 8.35; N, 14.32

Synthesis of N-(isopropyl)-N'-(neopentyl) -1,8-diaminonaphthalene, (iPrNH)(NpNH)$C_{10}H_6$ (4.4): Reaction of pivaloylchloride with **4.2** in the presence of excess base generated the trimethylacetamide intermediate, (iPrNH)(tBuCONH)$C_{10}H_6$ (**4.3**) which was used without further purification. In a Schlenk flask, lithium aluminum hydride (1.46 g, 38.4 mmol) was dissolved in 50 mL of dry ether, cooled in an ice bath and stirred for 1 h. Compound **4.3** (4.37 g, 15.3 mmol) was added slowly as a solid to this solution under nitrogen and allowed to stir for 2 h. The reaction was stirred for 18 h at room temperature and quenched with wet ether. The organic layer was extracted with water, dried with sodium sulfate, by vacuum, and purified by flash chromatography to yield a purple solid (3.85 g, 93%). ^{1}H NMR (200MHz, 298 K, $CDCl_3$): δ 7.19(m, 4H), 6.60 (m, 2H), 5.23 (br, 2H), 3.65 (sept, 1H, J_{HH}=6.4 Hz), 2.91 (s, 2H), 1.29 (d, 6H, J_{HH}=6.4 Hz), 1.12 (s, 9H). ^{13}C NMR (500MHz, 298 K, $CDCl_3$): δ 147.2, 144.8, 136.8, 126.1, 125.6, 117.8, 117.3, 109.3, 105.4 (Carom), 57.2 (CH_2CMe_3), 45.2 ($CHMe_2$), 31.2 (CMe_3), 27.9 (CH_3), 22.7 (CH_3). Analysis Calcd $C_{18}H_{26}N_2$ C, 79.95; H, 9.69; N, 10.36; Found C, 79.63; H, 10.01; N, 10.39.

Synthesis of 1-isopropyl-3-neopentylperimidinium bromide, {$C_{10}H_6$(iPrN)(NpN)CH}{Br} (4.5b): In a round bottom flask, **4.4** (3.87 g, 14.3 mmol), Ammonium bromide (2.72 g, 14.3 mmol), and triethylorthoformate (21.2 g, 0.143 mol) were combined and stirred for 18 h at 45°C. The solvent was dried, and the product recrystallized from methylene chloride was a yellow solid (3.85 g, 66%). ^{1}HNMR (200MHz, 298 K, $CDCl_3$): δ 9.15 (s, 1H, N_2CH), 7.78 (d, 2H, CH), 7.38 (m, 4H, CH), 7.09 (d, 2H,CH), 6.90 (m, 2H, CH), 4.45 (sept, 1H, $CHMe_2$), 4.27 (s, 2H, CH_2), 2.30 (s, 3H, CH_3), 1.72 (d, 6H, CH_3), 1.08 (s, 9H, CH_3). ^{13}C NMR (500MHz, 298 K, CDCl3): δ 152.0 (N2CH), 143.7, 138.7, 135.0, 132.7, 131.4, 138.2, 128.1, 127.6, 125.8, 124.2, 124.0, 121.6, 108.4, 107.6 (Carom), 59.4 (CH_2CCH_3), 53.5 ($CHCH_3$), 27.7 (CH_2CCH_3), 21.1 (CH_2CCH_3), 19.8 ($CHCH_3$).

Synthesis of Enetetramine, ($C_{10}H_6$(^{i}PrN)(NpN)C)$_2$ (4.7). Compound **4.5b** (0.185 g, 1.10 mmol) was added to a solution of $KN(SiMe_3)_2$ (0.500 g, 1.10 mmol) in 20 mL of anhydrous 1:1 chlorobenzene/THF. The reaction was stirred for 2 days, and the volatiles were removed under vacuum. The solid was extracted with 15 mL of toluene followed by filtration. The filtrate was evaporated under vacuum to afford a pale orange, sticky solid (0.20 g, 64%), which crystallized from ether in -25°C to give colorless crystals. ^{1}H NMR (300 MHz, 298 K, C_6D_6): δ 7.20 (m, 8H, Ar), 6.75 (d, 2H, Ar), 6.69 (d, 2H, Ar), 4.17 (sept, 2H, $CHMe_2$), 4.02 (d, 2H, CH_2), 3.35 (d, 2H, CH_2), 1.55 (dd, 12H, ($C$$H_3$)$_2$), 0.99 (s, 18H, ($CH_3$)$_3$).

Synthesis of 1*H*-perimidine, $C_{11}H_8N_2$ (4.11). DAN (2.28 g, 14.4 mmol), formic acid (3.2 mL, 57 mmol), in 40 mL of ethanol were left to stir for 1h at room temperature. The reaction was then refluxed for 12h at 75°C. The mixture was cooled to 0°C and concentrated NH_4OH was added dropwise to neutralize excess formic acid. The product was filtered off using suction filtration and dried to produce a light brown solid (2.07 g. 88%). ^{1}H NMR ($CDCl_3$, 400 MHz): δ 7.33 (s, 1H, NCHN), 7.10 (m, 4H, Ar), 6.47 (dd, 2H, Ar).

Synthesis of *N*-2-pyridinylperimidine, $C_{10}H_6N(C_5H_4N)CH$ (4.12). 1.5 g (4.6 mmol) of **4.12**, 2-bromopyridine (0.4 mL, 4.2 mmol), 1-methyl-imidazole (1 mL, 12.5 mmol), CuI (80.5 mg, 0.4 mmol), K_2CO_3 (860 mg, 6.2 mmol) and DMF (9 mL) were combined and stirred for 20min at room temperature. The reaction was then refluxed at 110°C for 20h. The mixture was filtered over

Celite and washed with EtOAc (2 x 10 mL). 50 mL of EtOAc was added to the flask. The solution was extracted with brine (3 x 15 mL) and then dried with $NaSO_4$, which was removed with filtration. The organic residue was concentrated to around 5 mL before purification by column chromatography on silica gel (4:1 EtOAC:hexanes). The solvent was removed under vacuum to produce a yellow solid (0.6904 g, 60%). ^1H NMR ($CDCl_3$, 400 MHz): δ 8.66 (dd, 1H, Ar), 7.90 (td, 1H, Ar), 7.51 (m, 2H, Ar), 7.36 (ddd, 1H, Ar), 7.24 (m, 3H, Ar), 7.03 (t, 1H, Ar), 6.91 (d, 1H, Ar), 6.35 (d, 1H, Ar).

Preparation of *N*-methyl-*N'*-2-pyridylperimidinium iodide, $[C_{10}H_6(C_5H_4N)(CH_3N)CH]I$ (4.13). Under a normal atmosphere, **4.12** (0.1726 g, 0.7 mmol) and MeI (stabilized with copper) (4 mL, 64 mmol) were left to stir with minimal exposure to light for 96h at room temperature. The excess MeI was removed using rotary evaporation. The resultant solid was extracted with ether (3 x 20 mL). The aqueous fraction was collected and dried under vacuum. The product is a yellow crystalline solid (0.1424 g, 53%). ^1H NMR ($CDCl_3$, 400 MHz): δ 9.63 (s, 1H, NCHN), 8.70 (dd, 1H, Ar), 8.33 (d, 1H, Ar), 8.16 (td, 1H, Ar), 7.62 (ddd, 1H, Ar), 7.55 (dd, 2H, Ar), 7.46 (t, 1H, Ar), 6.87 (d, 1H, Ar), 6.55 (d, 1H, Ar), 3.87 (s, 3H, Me).

Appendix:

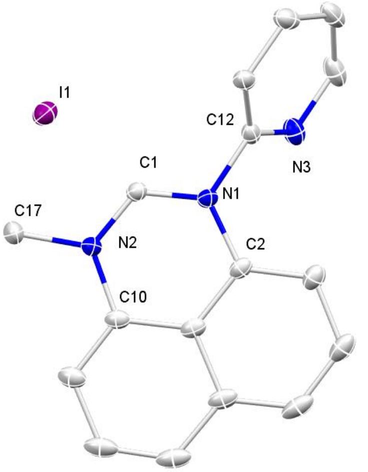

Figure 4.7 X-ray structure of **4.13**. Thermal ellipsoids are drawn at 20% probability. Hydrogen atoms are emitted for clarity.

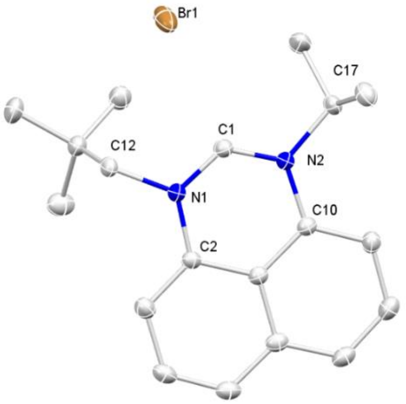

Figure 4.8 X-ray structure of **4.5b**. Thermal ellipsoids are drawn at 30% probability. Hydrogen atoms are emitted for clarity.

Table 4.1 Crystal data and structure refinement for **4.5b** and **4.13**

	4.5b	**4.13**
Empirical formula	$C_{19}H_{25}BrN_2$	$C_{17}H_{14}IN_3$
Formula weight	361.32	387.21
Temperature (K)	200(2)	200(2)
Wavelength (Å)	0.71073	0.71073
Crystal system	Orthorhombic	Monoclinic
Space group	P 21 21 21	C 2/c
a (Å)	7.5531(5)	22.7815(17)
b (Å)	11.1221(8)	21.0674(16)
c (Å)	20.8433(15)	8.2623(6)
α (deg)	90	90
β (deg)	90	108.09020(10)
γ (deg)	90	90
Volume ($Å^3$)	1751.0(2)	3769.4(5)
Z	4	8
Density (calculated) (Mg/m^3)	1.371	1.365
Absorption coefficient (mm^{-1})	2.347	1.696
F(000)	752	1520
Crystal size (mm^3)	0.640 x 0.510 x 0.170	0.248 x 0.083 x 0.069
Theta range for data collection (deg)	1.954 to 28.433	1.881 to 28.377
Index ranges	-9<=h<=10, -14<=k<=14, -27<=l<=27	-29<=h<=30, -28<=k<=28, -11<=l<=10
Reflections collected	29835	30240
Independent reflections	4378 [R(int) = 0.0262]	4695 [R(int) = 0.0349]
Completeness to theta = 25.242	100.0 %	100.0 %
Absorption correction	Semi-empirical from equivalents	Semi-empirical from equivalents
Max. and min. transmission	0.7457 and 0.7058	0.7457 and 0.5956
Refinement method	Full-matrix least-squares on F^2	Full-matrix least-squares on F^2
Data / restraints / parameters	4378 / 0 / 208	4695 / 0 / 198
Goodness-of-fit on F^2	1.063	1.060

Final R indices [I>2sigma(I)]	R1 = 0.0267, wR2 = 0.0643	R1 = 0.0264, wR2 = 0.0582
R indices (all data)	R1 = 0.0325, wR2 = 0.0665	R1 = 0.0471, wR2 = 0.0661
Extinction coefficient	n/a	n/a
Largest diff. peak and hole (e.Å^{-3})	0.772 and -0.794	0.582 and -0.482

Table 4.2 Selected Bond Lengths [Å] and Angles [°] for **4.5b** and **4.13**

4.5b		**4.13**	
Bond lengths (Å)			
N1-C1	1.318(3)	N1-C1	1.321(3)
N2-C1	1.317(3)	N2-C1	1.314(3)
N1-C2	1.4070(15)	N1-C2	1.429(3)
N2-C10	1.2912(16)	N2-C10	1.426(3)
N1-C12	1.4035(16)	N1-C12	1.448(3)
N2-C17	1.505(3)	N2-C17	1.467(3)
Bond Angle (°)			
N1-C1-N2	125.0(2)	N1-C1-N2	124.2(2)
C2-N1-C1	120.7(2)	C1-N1-C2	120.7(2)
C1-N1-C12	116.0(2)	C1-N1-C12	118.12(19)
C10-N2-C1	120.1(2)	C1-N2-C10	120.8(2)
C1-N2-C17	119.1(2)	C1-N2-C17	119.9(2)

Table 4.3 Crystal data and structure refinement for **4.7** and **4.15**

	4.7	**4.15**
Empirical formula	$C_{38}H_{48}N_4$	$C_{17}H_{13}N_3O$
Formula weight	560.80	275.30
Temperature (K)	200(2)	200(2)
Wavelength (Å)	0.71073	0.71073
Crystal system	Orthorhombic	Orthorhombic
Space group	P b c a	P n m a
a (Å)	16.1280(4)	21.847(16)
b (Å)	12.2122(3)	6.905(5)
c (Å)	16.1953(4)	9.030(7)
α (deg)	90	90
β (deg)	90	90
γ (deg)	90	90
Volume (Å^3)	3189.80(14)	1362.2(17)
Z	4	4
Density (calculated) (Mg/m^3)	1.168	1.342
Absorption coefficient (mm^{-1})	0.068	0.087
F(000)	1216	576
Crystal size (mm^3)	0.230 x 0.220 x 0.170	0.180 x 0.130 x 0.110
Theta range for data collection (deg)	2.441 to 24.149	2.441 to 24.125
Index ranges	-18<=h<=18, -14<=k<=11, -18<=l<=18	-25<=h<=25, -7<=k<=7, -10<=l<=10
Reflections collected	16741	10558
Independent reflections	2549 [R(int) = 0.0485]	1183 [R(int) = 0.0869]
Completeness to theta = 25.242	99.9 %	99.9 %
Absorption correction	Semi-empirical from equivalents	Semi-empirical from equivalents
Max. and min. transmission	0.7457 and 0.7058	0.7457 and 0.5956
Refinement method	Full-matrix least-squares on F^2	Full-matrix least-squares on F^2
Data / restraints / parameters	2549 / 112 / 265	1183 / 45 / 145

Goodness-of-fit on F^2	1.025	1.102
Final R indices [I>2sigma(I)]	R1 = 0.0427, wR2 = 0.0958	R1 = 0.0957, wR2 = 0.2810
R indices (all data)	R1 = 0.0828, wR2 = 0.1199	R1 = 0.1261, wR2 = 0.3028
Extinction coefficient	n/a	n/a
Largest diff. peak and hole (e.Å^{-3})	0.115 and -0.154	0.261 and -0.368

Table 4.3 Selected Bond Lengths [Å] and Angles [°] for **4.7** and **4.15**

4.7		**4.15**	
Bond lengths (Å)			
C12-C12’	1.341(4)	C1-O1	1.219(8)
N1-C12	1.430(3)	N1-C1	1.388(9)
N2-C12	1.425(2)	N1-C2	1.396(8)
N1-C10	1.394(2)	N2-C1	1.382(10)
N1-C14	1.467(2)	N2-C10	1.391(9)
N2-C2	1.405(2)	N1-C12	1.420(13)
N2-C19	1.496(5)	N2-N17	1.463(9)
Bond Angle (°)			
N1-C12-N2	112.43(15)	N1-C1-N2	116.7(6)
C12-N1-C10	114.52(16)	C1-N1-C2	124.4(6)
C12-N1-C14	121.84(16)	C1-N1-C12	115.0(6)
C12-N2-C2	111.92(16)	C1-N2-C10	123.3(6)
C12-N2-C19	125.8(4)	C1-N2-C17	116.0(7)

References:

1) R. Hoffmann, *J. Am.Chem. Soc.*, 1968, **90**, 1475.
2) P. B. Grasse, B. E. Brauer, J. J. Zupancic, K. J. Kaufmann, G. B. Schuster, *J. Am. Chem. Soc.* 1983, **23**, 105.
3) A. J. Arduengo III, R. L. Harlow, M. Kline, *J. Am. Chem. Soc.*, 1991, **113**, 361.
4) P. Lei, G. Meng, M. Szostak, *ACS Catal*, 2017, **7**, 1960.
5) C. Färber, M. Leibold, C. Bruhn, M. Maurer, U. Siemeling, *Chem. Commun.*, 2012, **48**, 227.
6) W. A. Herrmann, M. Elison, J. Fischer, C. Köcher, G. R. J. Artus, *Angew. Chem. Int. Ed. Engl.*, 1995, **107**, 2602.
7) J. Schwartz, V. P. W. Böhm, M. G. Gardiner, M. Grosche, W. Herrmann, W. Hieringer, G. Raudaschl-Siebr, *Chem. Eur. J.*, 2000, **6**, 1773.
8) F. Guillen, C. L.Winn, A. Alexakis, *Tetrahedron: Asymmetry* 2001, **12**, 2083.
9) R. W. Alder, M. E. Blake, C. Bortolotti, S. Bufali, C. P. Butts, E. Linehan, J. M. Oliva, A. G. Orpen, M. J. Quayle, *Chem. Commun.* 1999, 241.
10) C. C. Scarborough, M. J. W. Grady, I. A. Guzei, B. A. Gandhi, S. S. Stahl, *Angew. Chem., Int. Ed.* 2005, **44**, 5269.
11) P. Bazinet, T. G. Ong, J. S. O'Brien, N. Lavoie, E. Bell, G. P. A. Yap, L. Korobkov, D. S. Richeson, *Organometallics*, 2007, **26**, 2885.
12) P. Bazinet, G. P. A. Yap, D. S. Richeson *J. Am. Chem. Soc.* 2003, **125**, 13314.
13) H. Tsurugi, S. Fujita, G. Choi, T. Yamagata, S. Ito, H. Miyasaka, K. Mashiama, *Organometallics*, 2010, **29**, 4120.
14) S. Lee, B. Gabidullin, D. Richeson, *ACS Omega*, 2018, **3**, 6587.
15) G. Meng, L. Kakalis, S. P. Nolan, M. Szostak, *Tetrahedron Lett.*, 2019, **60**, 378.

16) R. W. Alder, L. Chaker, F. P. V. Paolini, *Chem. Commun*., 2004, 2172.

17) J. Argawal, T. W. Shaw, C. J. Stanton, G. F. Majetich, A. B. Bocarsly, H. F. Schaefer, *Angew. Chem. Int. Ed.*, 2014, **53** (20), 5152.

18) X. Zhao, Y. She, K. Fang, G. Li, *J. Org. Chem.*, 2017, **82**, 1024.

Chapter V

Conclusion

Overview and Future Work:

Tackling the issues of CO_2, presented in Chapter I, is a focus of many chemists and engineers presently and crowds the literature today, be it CO_2 capture[1,2] or catalytic conversion of CO_2 into more useful chemical sources[3]. Here we presented two projects in Chapters II and III focusing on the catalytic reduction of CO_2, concentrating on the field of homogenous transition metal complexes, known for their advantages of catalyst tuning and facile characterization, utilizing either light (photo) or electricity (electro) as a source of potentially renewable energy.

Chapter III expanded on the popular Re(I) complexes as integrated photosensitizer/catalysts taking advantage of the MLCT observed at wavelengths in the visible light region when coordinating α-diimine ligands. These Re(I) complexes date back over 30 years ago starting with the *fac*-Re(bpy)$(CO)_3$X and growing with the introduction of supporting ligands such as NHCs.[5,6] We synthesized three complexes, **2.1**, **2.2** and **2.3**, exploring a novel coordination environment with two bidentate ligands chelating a Re(I) metal center. When exposed to a photochemical system purged with CO_2, all three complexes exhibited catalytic reduction products. Interestingly, our compounds showed a selectivity for formate as the CO_2 reduction product, making these Re(I) unique among those in the literature, which have been shown to be selective for carbon monoxide. This indicates a possible favoritism for the formation of a metal hydride intermediate, known to be an intermediate in the formate mechanism. In addition to an integrated sensitizer/catalyst system, catalytic enhancements were observed with the addition of an organic dye, Rodamine 6-G, neglecting the need of the more expensive noble metal photosensitizers typically equipped in these systems.

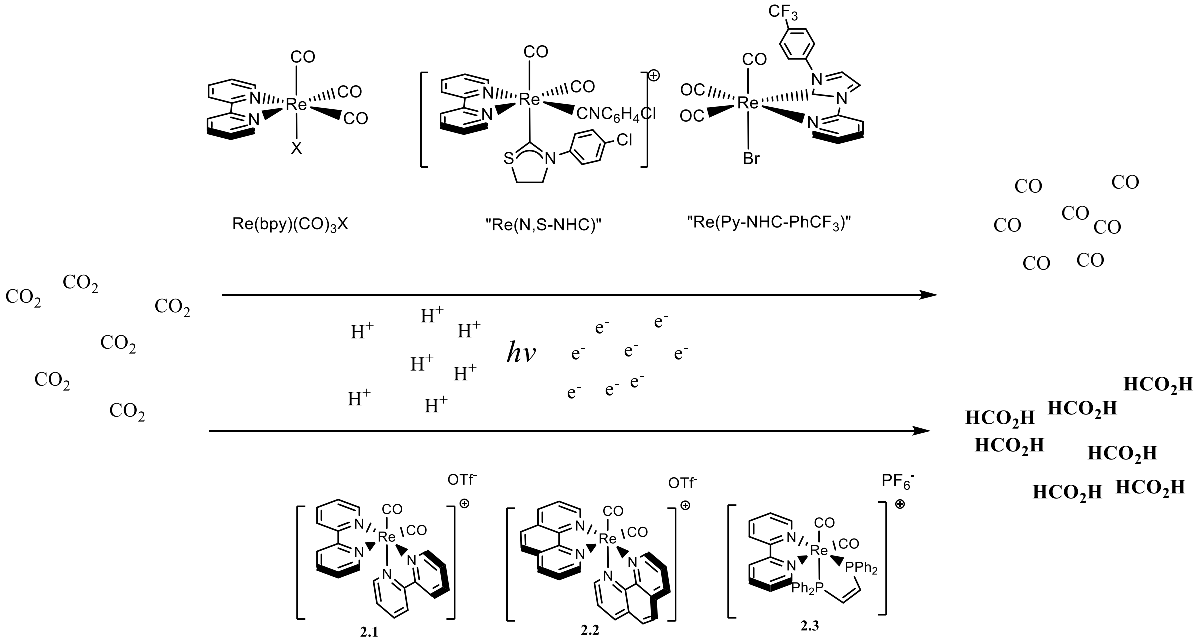

Figure 5.1 Catalytic CO_2 reduction product selectivity for various Re(I) complexes.

Improvements in the photocatalytic system of these Re(I) compounds can be done with the light provided. All reactions used a blue LED light, which did not represent the wavelength of the max absorbance of compounds **2.1**, **2.2** and **2.3** observed form their UV-vis spectrums. This project illustrated a scheme to generate an alternative CO_2 product selectively using Re(I) by structural tuning of the known literature compounds.

Chapter III introduced a different CO_2 reduction system utilizing an electrochemical cell. This expanded on our series of phosphino aminopyridine coordinating first row metal complexes in catalytic CO_2 reduction. We synthesized Zn(II) compounds, **3.1** and **3.2**, and evaluated their propensity for electrocatalytic CO_2 reduction. Here we were able to show unprecedented d^{10} metal complexes' tendency to reduce CO_2 under more commercially and environmentally favorable conditions than those reported in literature such as stoichiometric sacrifice of phosphines or utilization of noble metal electrodes. We reported the first Zn(II) catalyst for CO_2 reduction operating with water as the proton source and a glassy carbon electrode. Notably catalytic production was improved with **3.1**, indicating a possible advantage with the pendant pyridine as an aid in the coordination and configuration of CO_2 with the metal center.

Advancements to be made in this project could include a better understanding of the mechanism through chemical synthesis and isolation of intermediates of these complexes by use of strong reducing agents or generation of the Zn-H believed to be intermediate of the formate mechanism. This may help further grasp an approach for a selective reduction product as well as possibly reducing hydrogen competition.

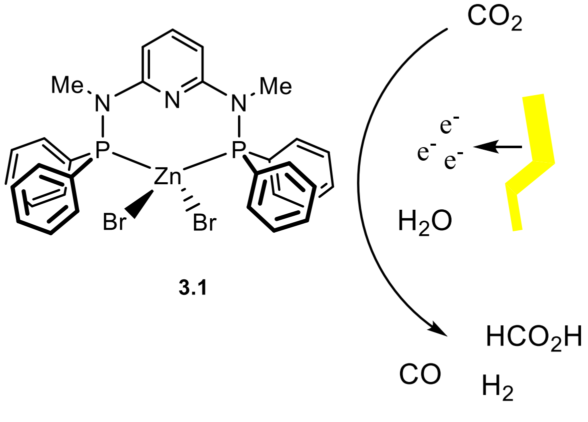

Figure 5.2 Catalytic reduction of CO_2 with **3.1**

With the importance and popularity of NHCs as accessory ligands due to their strong sigma donating abilities specifically in the field of homogenous transition metal catalysis, Chapter IV reintroduced the perimidine based carbene first published by our group over a decade ago. This NHC framework provides a stronger sigma donating ability compared to the prevalent five membered ring counterparts[9,10] as perceived from the C-H j-coupling constant of its salt precursor. The six-membered backbone also provides smaller α angles, which allow for larger steric effects from smaller R-groups flanking the carbene carbon. The larger aromatic backbone also offers electronic stability in comparison to the traditional six membered NHC. This chapter also covered an attempt to synthesize a pyridyl-NHC bidentate ligand (**4.16**), a more convenient ligand for catalysis, as well as a Zn(II) coordinated complex evident through NMR spectroscopy . Although not conclusive, this allows for optimism in its synthesis and use as a comparison to the phosphino aminopyridine complex, **3.2**.

The development of this NHC analogue expands on the use NHC particularly if one is looking to increase the electron density on the metal center and requires a broader scope of stable carbene ligands. Improvements in the synthesis of this ligands and their eventual metal complexes can be further evaluated by a more a diligent emphasis on the purification of intermediates as well as more thorough search on methods that introduce less reagents. Once synthesized, further investigation of the complexes for CO_2 catalysis to assess their proficiency in contrast with the studies of the pyridyl imidazole NHC and the phosiphino aminopyridine counterparts found in the literature.

References:

1) Y. Wang, L. Zhao, A. Otto, M. Robinius, D. Stolten, *Energy Procedia*, 2017, **112**, 650.
2) C. H. Yu, C. H. Huang, C. S. Tan, *Aerosol Air Qual. Res.*, 2012, **12**, 745.
3) M. Y Lee, K. T. Park, W. Lee, H. Lim, Y. Kwon, S. Kang, *Crit. Rev. Environ. Sci. Technol.*, 2020, **50**, 769.
4) I. I. Alkhatib, C. Garlisi, M. Pagliaro, K. Al-Ali, G. Palmisano, *Catal. Today,* 2020, **340**, 209.
5) H. Rao, J. Bonin, M. Robert, *Chem. Commun.*, 2017, **53**, 2830.
6) A. J. Huckaba , E. A. Sharpe, J. H. Delcamp , *Inorg. Chem.*, 2016, **55**, 682.
7) W. Sattler, G. Parkin, *J. Am. Chem. Soc.*, 2012, **134**, 17462.
8) R. Dobrovetsky, D. W. Stephan, *Angew. Chemie - Int. Ed.*, 2013, **52**, 2516.
9) A. J. Arduengo III, R. L. Harlow, M. Kline, *J. Am. Chem. Soc.*, 1991, **113**, 361.
10) P. Lei, G. Meng, M. Szostak, *ACS Catal*, 2017, **7**, 1960.